
Precise Transit Photometric Studies of Exoplanets and Exomoons

A thesis submitted for the degree of

Doctor of Philosophy

in

The Department of Physics,
Pondicherry University,
Puducherry - 605 014, India



by

Suman Saha

Indian Institute of Astrophysics
Bangalore - 560 034, India



September, 2022

Precise Transit Photometric Studies of Exoplanets and Exomoons

Suman Saha

Indian Institute of Astrophysics



Indian Institute of Astrophysics
Bangalore - 560 034, India

Title of the thesis : **Precise Transit Photometric Studies
of Exoplanets and Exomoons**

Name of the author : **Suman Saha**

Address : Indian Institute of Astrophysics
II Block, Koramangala
Bengaluru - 560034, India

Email : suman.saha@iiap.res.in

Name of the supervisor : **Prof. Sujan Sengupta**

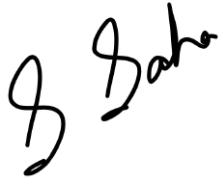
Address : Indian Institute of Astrophysics
II Block, Koramangala
Bengaluru - 560034, India

Email : sujan@iiap.res.in

Declaration of Authorship

I hereby declare that the matter contained in this thesis is the result of the investigations carried out by me at the Indian Institute of Astrophysics, Bangalore, under the supervision of Prof. Sujan Sengupta. This work has not been submitted for the award of any other degree, diploma, associateship, fellowship etc. of any other university or institute.

Signed:

A handwritten signature in black ink, appearing to read 'S Saha', is written above a horizontal line.

Date:

26-06-2023

Certificate

This is to certify that the thesis entitled '**Precise Transit Photometric Studies of Exoplanets and Exomoons**' submitted to the Pondicherry University by Mr. Suman Saha for the award of the degree of Doctor of Philosophy, is based on the results of the investigation carried out by him under my supervision and guidance, at the Indian Institute of Astrophysics. This thesis has not been submitted for the award of any other degree, diploma, associateship, fellowship, etc. of any other university or institute.

Signed:



Date:

26-06-2023

To my parents, who taught me to love what I do...

Acknowledgement

I would like to thank the Indian Institute of Astrophysics (IIA), Bengaluru, for providing me with this wonderful opportunity to pursue my PhD. I would like to thank my PhD supervisor Prof. Sujan Sengupta, who has guided me through the ups and downs of my PhD and taught me how to become a successful researcher. I'm truly thankful to the unmeasurable amount of time and efforts that he has bestowed, and the innumerable discussions, which have helped me to tackle many difficult problems. I would like to thank my colleague and collaborator Dr. Aritra Chakrabarty for his help and contributions in my published works.

I would like to thank the supporting staffs at the Indian Astronomical Observatory (IAO), Hanle, the Center For Research and Education in Science and Technology (CREST), Hosakote, and the Vainu Bappu Observatory (VBO), Kavalur. Some of the computational results reported in this work were performed on the high performance computing facility (NOVA) of IIA, Bangalore. I'm thankful to the computer division of Indian Institute of Astrophysics for the help and co-operation. I have used PyRAF for most of the tasks of data reduction and photometry. PyRAF is a product of the Space Telescope Science Institute, which is operated by AURA for NASA. This work includes data collected by the TESS mission, which are publicly available from the Mikulski Archive for Space Telescopes (MAST). I acknowledge the use of public TOI Release data from pipelines at the TESS Science Office and at the TESS Science Processing Operations Center. Funding for the TESS mission is provided by NASA's Science Mission directorate. Support for MAST is provided by the NASA Office of Space Science via grant NNX13AC07G and by other grants and contracts. This research made use of Lightkurve, a Python package for Kepler and TESS data analysis.

I would like to thank the American Astronomical Society (AAS) and the journals published by them, The Astronomical Journal (AJ) and The Astrophysical Journal (ApJ), to provide the adequate platforms to publish my works. I would like to thank the anonymous reviewers, who reviewed my works before publications, for a critical reading of the manuscripts and for providing many useful comments and suggestions. I would like to thank the Astronomical Society of India (ASI) for providing me the

opportunities to present my work during the 38th and 40th annual meetings held at IISER Tirupati in 2020 and IIT Roorkee in 2022 respectively. I would like to thank the public outreach committee (SCOPE) of IIA, the Department of Science and Technology (DST) of GOI, the Press Information Bureau (PIB) of GOI and many national news media agencies including The Times of India, India Today and Times Now for covering news articles on my research outputs.

I would like to thank the the faculties and colleagues at IIA, with whom I had fruitful discussions and interactions during my PhD. I would like to thank my Doctoral Committee members, Prof. Gajendra Pandey, Indian Institute of Astrophysics and Dr. Alok Saran, Pondicherry University, for providing many valuable inputs towards my PhD work. I would also like to thank Prof. Gajendra Pandey for guiding me during the course work project work of my PhD and the faculties at IIA and IISc who taught us during the PhD course work.

I would like to thank my alma maters and all the teachers who taught me at the different stages of my student life. I would like to thank the education system of my country for providing all the necessary opportunities to fulfill my dreams.

Finally, I would like to thank my family for being there with me in my endeavor.

Abstract

The most challenging limitation in the transit photometry method arises from the noises in the photometric signal. In particular, the ground-based telescopes are heavily affected by the noise due to the perturbation in Earth's atmosphere. Use of telescopes with larger apertures can improve the photometric signal-to-noise ratio (S/N) to a great extent. However, detecting a transit signal out of a noisy light curve of the host star and precisely estimating the transit parameters call for various noise reduction techniques. In our first project, we have presented multi-band transit photometric follow-up studies of five hot-Jupiters e.g., HAT-P-30 b, HAT-P-54 b, WASP-43 b, TrES-3 b and XO-2 N b, using the 2m Himalayan Chandra Telescope (HCT) at the Indian Astronomical Observatory, Hanle and the 1.3m J. C. Bhattacharya Telescope (JCBT) at the Vainu Bappu Observatory, Kavalur. In order to reduce the noise components present in the observational data, we have used a critical noise treatment approach using sophisticated techniques, such as the wavelet denoising and Gaussian process regression, which effectively reduce both time-correlated and time-uncorrelated noise components from the transit light curves. In addition to these techniques, use of our state-of-the-art model algorithm have allowed us to estimate the physical properties of the target exoplanets with a better accuracy and precision compared to the previous studies.

Unlike the ground-based telescopes, the observations from the space-based telescopes are free from any noise component due to the interference of Earth's atmosphere. This is the reason why most of the sophisticated telescopes used in exoplanetary science are space-based. However, the observations from these space-based telescopes still contain noise components due to various instrumental effects and the stellar activity and pulsations. In our second project, we have presented the critical analysis of space-based transit photometric observations from the Transiting Exoplanet Survey Satellite (TESS). We have developed an optimized noise treatment and modeling algorithm based on the algorithm used in our previous project, which also implements the techniques like the wavelet denoising and Gaussian process regression. We have demonstrated the effectiveness of our algorithm by implementing it to the TESS transit photometric observations for four hot Jupiters: KELT-7 b,

HAT-P-14 b, WASP-29 b, WASP-95 b, and a hot Neptune: WASP-156 b. The better quality of photometric data from TESS, combined with our state-of-the-art noise reduction and analysis technique, has resulted into much more accurate and precise values of the physical properties for the target exoplanets than that reported in earlier works.

The effectiveness of the transit photometry method to detect and characterize exoplanets has already been demonstrated by the discovery of thousands of exoplanets using several ground-based as well as space-based survey missions. With the advent of the upcoming next generation large telescopes, the detection of exomoons in a few of these exoplanetary systems is very plausible. In our third project, we present a comprehensive analytical formalism in order to model the transit light curves for such moon hosting exoplanets. In order to achieve analytical formalism, we have considered circular orbit of the exomoon around the host planet, which is indeed the case for tidally locked moons. The formalism uses the radius and orbital properties of both the host planet and its moon as model parameters. The coalignment or non-coalignment of the orbits of the planet and the moon is parameterized using two angular parameters and thus can be used to model all the possible orbital alignments for a star-planet-moon system. This formalism also provides unique and direct solutions to every possible star-planet-moon three circular body alignments. Using the formula derived, a few representative light curves are also presented.

Rocky exomoons around the giant exoplanets in habitable zones hold special significance as they can harbor life. Although the detection of exomoons has yet remained elusive, mainly due to their smaller expected size, the next generation large telescopes can provide unique opportunities for their detection and characterization. In our fourth project, we have studied the capability of the large space based James Webb Space Telescope (JWST) to detect the smaller sub-Earth sized exomoons in the habitable zones of G- and K-type stars. We have consider three different sizes of the moon, i.e. similar in size to the mars, the titan and the luna, and estimated the minimum photometric precision required to detect them. By comparing them to the expected obtainable photometric precision using the NIRCAM instrument of JWST and using different near-infrared filters, we have concluded that exomoons as small as the titan would be detectable around a G2 type star and that as small as the luna would be detectable around a K2 type star.

Publications

- Suman Saha, Aritra Chakrabarty and Sujana Sengupta, “Multiband Transit Follow-up Observations of Five Hot Jupiters with Critical Noise Treatments: Improved Physical Properties”, *The Astronomical Journal*, 162(1):18, 2021. doi:10.3847/1538-3881/ac01dd.
- Suman Saha and Sujana Sengupta, “Critical Analysis of TESS Transit Photometric Data: Improved Physical Properties for Five Exoplanets”, *The Astronomical Journal*, 162(5):221, 2021. doi:10.3847/1538-3881/ac294d.
- Suman Saha and Sujana Sengupta, “Transit Light Curves for Exomoons: Analytical Formalism”, *The Astrophysical Journal*, 936(1):2, 2022. doi:10.3847/1538-4357/ac85a9.
- Suman Saha and Sujana Sengupta, “Detection of Habitable Exomoons in the JWST Era”, *submitted*.

Contents

1	Introduction	
1.1	Exoplanets and their detection	1
1.2	Detection of exoplanet transits	4
1.3	Analysis of the exoplanet transit lightcurves	5
1.4	Exomoons and their detection	6
1.5	Modeling the lightcurves of transiting exomoons	7
1.6	Habitable exomoons	8
2	Multiband follow-up studies of transiting exoplanets using ground based facilities	
2.1	Introduction	9
2.2	Target selection and observations	12
2.3	Data reduction and analysis	14
2.4	Results and Discussion	30
2.5	Conclusion	31
3	Critical analysis of space-based transit photometric observations from TESS	
3.1	Introduction	39
3.2	Target selection and observational data	41
3.3	Data analysis and modeling	42
3.4	Discussion	50
3.5	Conclusion	54
4	Transit light curves for exomoons: Analytical formalism	
4.1	Introduction	63
4.2	Analytical formalism	65
4.3	Results and discussion	78
4.4	Conclusion	83
5	Detection of habitable exomoons in the JWST era	
5.1	Introduction	87
5.2	Transiting exomoons	88
5.3	Detection of transiting exomoons through JWST	91

5.4 Conclusion	99
6 Summary	

List of Figures

2.1	Observational and modelled light curves for HAT-P-30 b. For each observed transit event (see Table 2.2), the observation date, the instrument, and the photometric filter used are mentioned. Top: the unprocessed light curve (cyan), light curve after Wavelet Denoising (magenta), the best-fit transit model (orange). Middle: the residual after modelling without GP regression (magenta), the mean (orange) and $1-\sigma$ interval (cyan) of the best-fit GP regression model. Bottom: mean residual flux (orange).	15
2.2	Same as Figure 2.1, but for HAT-P-54 b	16
2.3	Same as Figure 2.1, but for WASP-43 b	17
2.4	Same as Figure 2.1, but for TrES-3 b	18
2.5	Same as Figure 2.1, but for XO-2 N b	19
2.6	Corner diagram depicting the posterior distributions of the transit parameters and the GP regression coefficients from MCMC sampling for HAT-P-30 b.	33
2.7	Same as Figure 2.6, but for HAT-P-54 b	34
2.8	Same as Figure 2.6, but for WASP-43 b	35
2.9	Same as Figure 2.6, but for TrES-3 b	36
2.10	Same as Figure 2.6, but for XO-2 N b	37
3.1	Observed and best-fit model light-curves of one transit event for each of our target exoplanets. For each observed transit, Top: the unprocessed light-curve (cyan), light-curve after wavelet denoising (magenta), the best-fit transit model (blue). Middle: the residual after modeling without GP regression (magenta), the mean (blue) and $1-\sigma$ interval (cyan) of the best-fit GP regression model. Bottom: mean residual flux (blue). All lightcurves used in this study are shown in Figures 3.2-3.6	43
3.2	All observed and best-fit model light-curves for KELT-7 b, with descriptions same as Figure 3.1	56

3.3	Same as Figure 3.2, but for HAT-P-14 b	57
3.4	Same as Figure 3.2, but for WASP-29 b	58
3.5	Same as Figure 3.2, but for WASP-95 b	59
3.5	Same as Figure 3.2, but for WASP-95 b (<i>cont.</i>)	60
3.6	Same as Figure 3.2, but for WASP-156 b	61
4.1	Orbital orientation of the star-planet-moon system from the observer's point of view, showing z_{sp} , z_{pm} and z_{sm} , the separations between the centers of the star and the planet, the planet and the moon, and the star and the moon respectively; z_{sb} , z_{pb} and z_{mb} , the separation of the planet-moon barycenter from the centers of the star, the planet and the moon respectively; α_{mb} , the angle between the major axes of the projected orbits of the planet-moon barycenter around the star and the moon around the planet-moon barycenter; a_b and a_m , the orbital semi-major axes of the planet-moon barycenter around the star and the moon around the planet-moon barycenter respectively.	66
4.2	(I) Alignment with star-planet and planet-moon intersections showing l_{1s} and l_{2s} , the separation of the star from the points of intersection of the planet and the moon; (II) Alignment with star-planet and star-moon intersections showing l_{1p} and l_{2p} , the separation of the planet from the points of intersection of the star and the moon; (III) Alignment with star-planet and star-moon intersections showing l_{1m} and l_{2m} , the separation of the moon from the points of intersection of the star and the planet.	68
4.3	An instance of all possible cases of alignments for the star (blue), the planet (red) and the moon (green).	69
4.4	Alignment with intersection of all the three bodies (i.e., the star, the planet and the moon) showing A_{Δ} , the area of the triangle and A_{sa} , A_{pa} and A_{ma1} , the areas of the arcs within the common area of intersection of the three bodies.	74
4.5	Transit light-curves of a moon hosting exoplanetary system: (a) with $r_p = 0.1$, $r_m = 0.01$, $t_{0b} = 5$ days, $t_{0m} = 10$ days, $P_b = 300$ days, $P_m = 20$ days, $r_{pm} = 200$, $M_p/M_m = 1411$, $i_b = 90^\circ$, $i_m = 90^\circ$, $\alpha_{mb} = 0^\circ$, $u_1 = 0.4$ and $u_2 = 0.25$; and (b) replacing $t_{0m} = 8$ days. . .	80

4.6	Transit light-curves of a moon hosting exoplanetary system: (a) with $r_p = 0.1$, $r_m = 0.01$, $t_{0b} = 5$ days, $t_{0m} = 10$ days, $P_b = 300$ days, $P_m = 20$ days, $r_{pm} = 200$, $M_p/M_m = 1411$, $i_b = 90^\circ$, $i_m = 90^\circ$, $\alpha_{mb} = 20^\circ$, $u_1 = 0.4$ and $u_2 = 0.25$; and (b) replacing $t_{0m} = 8$ days and $\alpha_{mb} = 30^\circ$	81
4.7	Transit light-curves of a moon hosting exoplanetary system: (a) with $r_p = 0.075$, $r_m = 0.02$, $t_{0b} = 5$ days, $t_{0m} = 10$ days, $P_b = 60$ days, $P_m = 15$ days, $r_{pm} = 25$, $M_p/M_m = 81$, $i_b = 90^\circ$, $i_m = 90^\circ$, $\alpha_{mb} = 0^\circ$, $u_1 = 0.4$ and $u_2 = 0.25$; and (b) same but with $t_{0m} = 5$ days. The dashed red lines show the transit lightcurves of the planet in the absence of a moon. The transit-time-variation (TTV) due to the presence of a moon can be observed in (a).	82
4.8	Alignment of the three bodies with star-planet and planet-moon intersections.	84
5.1	Transit lightcurves corresponding to the parameter values given in Table 5.2 with the host-stars being (a) G2 and (b) K2 type.	90
5.2	The expected photometric precision (dashed lines) for given integration times compared with the transit lightcurves for different sizes of the moons with the host-stars being (a) G2 type with $V_{mag} = 8.$, (b) K2 type with $V_{mag} = 9.,...$ [cont.]	92
5.2	[cont.] ... (c) G2 type with $V_{mag} = 11.5$ and (d) K2 type with $V_{mag} = 12.5.$	93
5.3	The expected photometric precision (dashed lines) for given integration times compared with the transit depths for different sizes of the moons and different values of the impact factor with the host-stars being (a) G2 type with $V_{mag} = 8.$, (b) K2 type with $V_{mag} = 9.,...$ [cont.]	94
5.3	[cont.] ... (c) G2 type with $V_{mag} = 11.5$ and (d) K2 type with $V_{mag} = 12.5.$	95

List of Tables

1.1	Physical properties estimated from transit photometry	6
2.1	Adopted physical properties of the exoplanets and their host-stars . .	12
2.2	Details of the photometric observations	13
2.3	Estimated values of physical parameters for HAT-P-30 b	24
2.4	Estimated values of physical parameters for HAT-P-54 b	25
2.5	Estimated values of physical parameters for WASP-43 b	26
2.6	Estimated values of physical parameters for TrES-3 b	27
2.7	Estimated values of physical parameters for XO-2 N b	28
2.8	Mid-transit times and GP regression parameters for each observed transit event	29
3.1	Physical properties of the host stars	41
3.2	Estimated physical parameters for KELT-7 b	45
3.3	Estimated physical parameters for HAT-P-14 b	46
3.4	Estimated physical parameters for WASP-29 b	47
3.5	Estimated physical parameters for WASP-95 b	48
3.6	Estimated physical parameters for WASP-156 b	49
3.7	Best-fit GP regression model parameters	50
3.8	Estimated mid-transit times	51
3.8	Estimated mid-transit times (<i>cont.</i>)	52
3.9	Estimated CDPP for lightcurves	53
4.1	Different cases of star-planet-moon alignments	75
4.1	Different cases of star-planet-moon alignments (<i>cont.</i>)	76
4.1	Different cases of star-planet-moon alignments (<i>cont.</i>)	77
5.1	Physical properties of stellar and planetary bodies	88
5.2	Transit parameters for different scenarios	89
5.3	Photometric precision [in ppm] required for the detection of exomoons of different sizes around G2 and K2 type stars	96

5.4	Photometric precision [in ppm] obtainable from different filters for G2 type host stars of different V_{mag} for an integration time of 3 hrs. . . .	97
5.5	Photometric precision [in ppm] obtainable from different filters for G2 type host stars of different V_{mag} for an integration time of 3 hrs. . . .	98

Chapter 1

Introduction

1.1 Exoplanets and their detection

The exoplanets (also known as extra-solar planets) are the planets beyond our solar system. As the planets are much smaller in size compared to the stars they orbit around, and unlike their stellar counterparts, they have no source of radiation due to nuclear fusion, they are extremely faint and hard to detect. Over the years, several detection techniques have evolved to detect and characterize the exoplanets, such as radial velocity (Cumming, 2004; Hatzes, 2016; Lovis & Fischer, 2010; Perryman, 2000; Wright, 2018), transit photometry (Deeg & Alonso, 2018; Haswell, 2010; Winn, 2010; Wright & Gaudi, 2013), gravitational microlensing (Bennett, 2008; Gaudi, 2010), astrometry (Malbet & Sozzetti, 2018; Quirrenbach, 2010), direct imaging (Hinkley et al., 2021; Pueyo, 2018; Traub & Oppenheimer, 2010) and transit timing variations (Agol & Fabrycky, 2018) etc.

The radial velocity method (also known as ‘doppler spectroscopy’) was used for the detection of the first ever exoplanet around a main-sequence star in the year 1995, named 51Peg b (Mayor & Queloz, 1995). This method relies on the periodic doppler shift in the spectrum of the planet hosting star due to the gravitational impact of the orbiting planet. As mass is a major factor in gravitational interactions, and increasing mass of the planet will increase its impact of the star, most of the exoplanets discovered through the radial velocity method are massive. On the other hand, the gravitational interactions between two bodies are also affected by the distance between them. As the gravitational force imparted by the planet decreases with the increase in its distance from the host star, most of the exoplanets discovered through the radial velocity method are also orbiting their host stars in close-in orbits. Radial velocity method provides lower constrain on the mass of the detected exoplanets along with the orbital period. However, radial velocity method is not well suited for the detection of smaller exoplanets and the exoplanets in wider orbits around their host stars. Also, it is both time and resource consuming to survey individual stars through spectroscopic techniques, decreasing the effectiveness of the

radial velocity method for large scale surveys to discover exoplanets.

The transit photometry method (or simply ‘transit method’) was used for the first time in 1999 to confirm the first ever transiting exoplanet, named HD209458 b (Henry et al., 2000). The transit method relies on the detection of the small decrease in the magnitude of the host star due to a transiting planet. The transit probability decreases with the increase in the distance of the planet from the star. This is the reason why most of the exoplanets detected using the transit method orbit in closed-in orbits around their host stars. Also, the photometric precision required to detect the exoplanets using transit method increases with the decrease in the size of the planet with respect to its host star. However, such higher precision can be accomplished using larger telescopes or space based facilities. Another advantage of using a photometric method over a spectroscopic one is that the stars over a large field of view can be surveyed simultaneously using the photometric method. Because of this advantage, several large scale dedicated space based missions have been planned and conducted for the discovery and study of new exoplanets using the transit method, which includes the likes of CoRoT (Convection, Rotation and planetary Transits), Kepler, K2 and TESS (Transiting Exoplanet Survey Satellite) among others. Till date, more than four thousand exoplanets have been discovered using the transit method, many of which are smaller exoplanets known as mini-Neptunes and super-Earths, making it the most effective method for the detection of new exoplanets. The transit method provides accurate information about the size and orbital properties of the detected exoplanets. Also, combining radial velocity measurements for such exoplanets, their mass can be estimated accurately.

The gravitational microlensing method relies on the magnification of a distant background star by the gravitational field of a foreground planet hosting system, when they are aligned exactly with respect to the observer. The gravitational field of the planet works as a second lens apart from the host-star, which perturbs the light from the distance source. This method is extremely sensitive and can be used to detect smaller exoplanets like the earth around a sun like star. Also, this method can be used to detect exoplanets in wider orbits around their host stars easily. Since gravitational interaction is the key behind the phenomenon of microlensing, this method gives extremely precise estimation of the mass of the detected exoplanets. However, the major disadvantage of this method lies in the fact that microlensing events are one time events and the observations are non-repeatable. This, combined with the fact that the detected exoplanetary systems using this method are very far away and can not be effectively studied using other methods like transit or radial

velocity, follow-up studied of these systems are not possible. Another drawback of the gravitational microlensing method is that the microlensing events are extremely rare and opportunistic, which limits the number of systems that can be surveyed using this method.

The astrometry method relies on measuring the position of an exoplanet hosting star precisely and detecting the tiny shift in its position due to its rotation around the planet-star center of mass. Astrometry is the oldest method that has been in use for the search of exoplanets. However, the detection of any exoplanet using this method has remained unsuccessful using the ground based telescopes. This is because, the shift in the position of a star due to the presence a companion exoplanet is so small that it is even smaller than the distortions in the photometric observations due to the earth's atmosphere. The first astrometric detection of an previously discovered exoplanet was successful using the space based Hubble Space Telescope (HST) in 2002 (Benedict et al., 2002). Recently, several exoplanets have been discovered using the astrometry method using the photometric data from the space based Gaia mission. One advantage of the astrometry method is that it can be used to estimate the mass of the exoplanets accurately, unlike the radial velocity method. Also, the astrometry can be used to detect exoplanets in very wide orbits around their host stars. However, such detections would also require a very long observation time.

The direct imaging method is used to detect large young exoplanets in a far away orbit from their host stars. The exoplanets detectable using this technique need to be large and hot in order to emit enough thermal emissions. Moreover, the radiation from the host star are blocked using a coronagraph in order to make the planet visible. This method gives an indirect estimation of the mass and size of the detected exoplanets. However, the major advantage of the direct imaging technique is that the chemical composition of the detected exoplanets can be studied.

The transit timing variations method consists of detecting the variation in the transit timing of a known transiting exoplanet due to the presence of an undiscovered planetary companion in the system. This method can be used to estimate of the maximum mass of the detected exoplanets, where the limit is due to the unknown orbital inclination. The major advantage of the transit timing variation method is that it can be used to detect exoplanets with smaller masses, those are not detectable through the radial velocity method, but orbiting close enough to a known transiting planet in the system which has a smaller mass compared to the host star, and thus is affected more by the gravity of the undiscovered planet.

Till date, most of the exoplanets have been discovered using the transit photometry

method, which is followed by the radial velocity method. The works in this thesis involve both observational and theoretical aspects of the transit method, as will be discussed in subsequent sections.

1.2 Detection of exoplanet transits

The exoplanet transit occurs when the planet crosses through the front of its host star while orbiting it, from the point of view of the observer. This is also known as the primary eclipse, in contrast to the secondary eclipse, which occurs when the exoplanet is occulted by the host star.

Several ground based as well as space based telescopes have been used over the years to detect exoplanet transits. The depth in the photometric lightcurves during an transit event, which is also known as the transit depth, depends upon the relative size of the exoplanet to its host star. Thus, for the detection of a smaller exoplanet compared to its host star, one would require a higher signal-to-noise ratio (SNR), which in turn would require a larger telescope. On the other hand, detection of transiting exoplanets around fainter stars would also require a larger telescope, which is because of the falling flux with the increase in the apparent magnitude.

Most of the survey telescopes, which are used for the discovery of new exoplanets, have large field of view, but very small aperture. Such set-ups are really effective for detecting new exoplanets. However, due to low SNR, the estimated physical properties of the detected exoplanets have high uncertainties. Thus, follow-up observations using telescopes of larger apertures are required to study the properties of these exoplanets more precisely. With this motive, we have used the 2m Himalayan Chandra Telescope (HCT) at the Indian Astronomical Observatory, Hanle and the 1.3m J. C. Bhattacharya Telescope (JCBT) at the Vainu Bappu Observatory, Kavalur, for the follow up studies of several known exoplanets. The larger apertures of these telescopes have resulted in photometric transit observations with higher SNR, which in turn have helped us to characterize these exoplanets more precisely. More about this has been discussed in Chapter 2.

On the other hand, the space based telescopes also provide several advantages over their ground based counter-parts in detecting exoplanet transits. This is the reason why several space based missions have been conducted, including the CoRoT, Kepler, K2 and TESS, and many other are being planned, to survey photometrically for new exoplanets. Some of these survey telescopes, such as the TESS, cover a large portion of the sky during its survey period. This provides opportunity not only for

the detection of a large number of new exoplanets, but also for the follow-up studies of many already known exoplanets. With this motive we have used the TESS data to conduct follow-up studies of several existing exoplanets and have characterized them with a better precision thanks to the better quality of photometric data from the space based observations. More about this has been discussed in Chapter 3.

1.3 Analysis of the exoplanet transit lightcurves

The observed lightcurves of exoplanet transits give valuable information about the physical properties of the system. In particular, the transit lightcurve directly depends upon the size of the exoplanet compared to the host star, the distance of the planet from the star and the orbital inclination angle of the planet compared to the field of view of the observer, which are known as transit parameters. The limb-darkening effect of the host star also affects the transit lightcurve, and thus can also be estimated from it. Some of the transit properties, such as radius of the planet, are wavelength dependent, and can be studied more precisely using multiband follow-up studies. We have conducted such multiband follow-up studies using our ground based telescopes, HCT and JCBT, and have estimated the wavelength dependent physical properties more precisely. More about this has been discussed in Chapter 2.

In order to model the transit lightcurves to estimate the physical properties of the exoplanets, one would require a comprehensive analytical formulation comprising of all the dependent physical factors. Mandel and Agol (2002) has provided such an analytic formulation, which also incorporates the limb darkening effect of the host star following the quadratic limb-darkening law. This formulation is widely used by the exoplanet communities, and also has been used in our studies. The transit parameters, which are estimated directly from the transit lightcurves, can also be used for the estimation of several other derivable physical properties of the exoplanets. A list of different physical properties of the exoplanets, which can be estimated using transit photometry, are given in Table 1.1.

One major limitation in the accuracy and precision of the estimated physical properties of the exoplanets from transit photometry comes from the embedded noise in the signals. Especially the noise components arising from the turbulence in the Earth's atmosphere, several instrumental effects and systematics, and the variability and pulsations of the host stars contribute dominantly in distorting the lightcurves. Sophisticated modern techniques can be used to treat these lightcurves in order to reduce these noise components, which can provide much better accuracy and

Table 1.1: Physical properties estimated from transit photometry

Parameter	Explanation
T_0 [BJD_{TDB}]	Initial transit time in BJD-TDB
P [$days$]	Orbital period in days
R_\star/a	Scaled stellar radius
R_p/R_\star	Ratio of planet to stellar radius
C_1	Limb darkening coefficient (linear term)
C_2	Limb darkening coefficient (quadratic term)
T_{14} [hr]	Transit duration in hours
a/R_\star	Scale parameter
i [deg]	Orbital inclination angle in degree
M_p [M_J]	Mass of the planet in Jupiter-mass
M_p [M_\oplus]	Mass of the planet in Earth-mass
T_{eq} [K]	Equilibrium temperature of the planet in Kelvin
a [AU]	Semi-major axis in AU
R_p [R_J]	Radius of planet in Jupiter-radius
R_p [R_\oplus]	Radius of planet in Earth-radius
T_C [BJD_{TDB}]	Mid-transit time in BJD-TDB

precision in the estimated physical properties of the exoplanets. We have discussed various aspects of modeling transit lightcurves with critical noise treatment analysis for both ground-based and space-based telescopes in Chapters 2 and 3.

1.4 Exomoons and their detection

Exomoons are the natural satellites around exoplanets beyond our solar system. Although natural satellites are abundant on the solar system, detection of exomoons has still remained elusive. As the transit method has remained the most effective method for the detection and characterization of the exoplanets, it could also provide the best opportunity for the detection of exomoons. Derivatives of the transit method involving the effect of the exomoon on the companion exoplanet, such as the Transit-Timing Variation (TTV, Sartoretti & Schneider, 1999; Szabó et al., 2006), and the Transit-Duration Variation (TDV, D. M. Kipping, 2009) have been proposed for the detection of exomoons. However, the amplitude of these effects is extremely

small for sub-Earth mass exomoons and so far no confirmed exomoon candidate has been detected using these techniques (Fox & Wiegert, 2021; D. Kipping, 2020, 2021). Several other techniques have also been proposed for the detection of exomoons, such as photometric orbital sampling effect (Heller, 2014; Teachey et al., 2018), imaging of mutual transits (Cabrera & Schneider, 2007), microlensing (Han & Han, 2002), spectroscopy (R. E. Johnson & Huggins, 2006; Oza et al., 2019; Williams & Knacke, 2004), polarimetry of self-luminous exoplanets (Sengupta & Marley, 2016), doppler monitoring of directly imaged exoplanets (Agol et al., 2015), pulsar timing (Lewis et al., 2008) and radio emissions of giant exoplanets (Noyola et al., 2014, 2016). However, no confirmed exomoon candidate has yet been detected by using any of these techniques.

The major reason behind the non-detection of exomoons till date, even if our solar system is teeming with natural satellites, is that the moons tend to be much smaller in size compared to the planets, which would require a much better photometric precision to detect them. The next generation large telescopes, such as the James Webb Space Telescope (JWST), would be able to achieve such high photometric precision, which could provide a unique opportunity to detect the first confirmed exomoons. Another reason for the non-detection of exomoons till date is that most of the exoplanets discovered till date have been found in close-in orbits. Several studies (Dobos et al., 2021; Namouni, 2010; Spalding et al., 2016) have suggested that such exoplanets would lose any natural satellite present around them during their migration to such close-in orbits. However, the present and upcoming long term transit photometric survey missions would be able to discover more number of exoplanets in wider orbits, increasing the probability for the detection of transiting exomoons in future.

1.5 Modeling the lightcurves of transiting exomoons

As discussed in the previous section, the transit method could prove to be the most effective mean for the detection of first confirmed exomoons in future, and as such the next generation large telescopes, such as JWST, would play a crucial role. Under such possibilities, a comprehensive analytical formalism for modeling the lightcurves of a transiting exoplanetary system hosting exomoons is the need of the time.

Deriving an analytical formalism for modeling the exomoon transit lightcurves would require to solve a three body problem, including the star, the moon and the planet. Depending upon the scenario of formation and evolution, the plane of the

orbit of the moon around the planet may or may not be coaligned with the orbit of the planet around the star. Also, depending upon the alignment of the three bodies, i.e. the star, the planet and the moon, the stellar flux occulted by the planet and the moon would have to be calculated. This would require defining the conditions where different cases of the three body alignments will hold, along with the area of overlap between these bodies. We have formulated such an analytical formalism to model the lightcurves of an exomoon hosting system, which is discussed in the Chapter 4.

1.6 Habitable exomoons

The detection probability of giant exoplanets is more compared to their smaller counterparts using the transit method. Some of these giant exoplanets have also been discovered in the habitable zones of their host stars. While these giant planets may not provide the most ideal condition for the study of planetary habitability, the possible smaller rocky exomoons around such exoplanets may provide unique opportunities for finding life outside our solar system. We have studied the detectability of such smaller exomoons, in the habitable zones of G-type and K-type host stars, using the next generation large space based telescopes, JWST, which we have discussed in Chapter 5.

Chapter 2

Multiband follow-up studies of transiting exoplanets using ground based facilities *

2.1 Introduction

The transit photometry serves as one of the most important methods in the context of exoplanet detection and characterisation. This method helps us to determine several physical parameters of a transiting exoplanet, e.g., the radius, the inclination angle of the planetary orbit with respect to our line of sight, and the semi-major axis. However, a prior knowledge of the stellar radius is necessary for the estimation of these parameters. Modelling the transit light curves also allows us to determine the limb-darkening properties of the parent stars. Moreover, the orbital inclination angle estimated by using the transit method can be combined with the radial-velocity measurements, if available, and a prior knowledge of stellar mass to precisely estimate the mass of those exoplanets (Chakrabarty & Sengupta, 2019; Southworth et al., 2007).

The photometric observations obtained from the ground-based telescopes are heavily affected by the turbulence in the Earth's atmosphere. This significantly adds to the overall noise in the observed signal. Moreover, if the ground-based survey telescopes used for the detection of new transiting exoplanets is small, it gives rise to a poor signal-to-noise ratio (S/N) in the observed transit signals. Therefore, repeated follow-up observations are very important in order to estimate the physical properties of the confirmed exoplanets with a good accuracy and precision. Repeated follow-up observations with telescopes of larger aperture can result in high S/N in the transit light curves causing small error-bars in the light-curves. Further, in order to achieve an improved accuracy and precision in the values of the estimated transit parameters,

*Part of this work is published in Suman Saha et al 2021 AJ 162 18,
doi:10.3847/1538-3881/ac01dd.

application of critical noise reduction techniques is essential to reduce the fluctuations prevailing in the transit light curves. The results from transit follow-ups spanning over a large period of time can be used for the studies of planetary dynamics and may reveal the presence of any undiscovered planetary mass objects in those systems (Gillon et al., 2017; M. C. Johnson et al., 2015; Maciejewski et al., 2018; Nesvorný et al., 2012; Patra et al., 2017).

Our ongoing project involves the photometric follow-up of transiting exoplanets using multiple photometric bands and analysis using noise reduction techniques for an improved estimation of the physical properties. For photometric follow-up, we use the 2m Himalayan Chandra Telescope (HCT) at the Indian Astronomical Observatory, Hanle and the 1.3m J. C. Bhattacharya Telescope (JCBT) at the Vainu Bappu Observatory, Kavalur. We have followed up five hot Jupiters in multi-wavelength bands, namely HAT-P-30 b (e.g., J. A. Johnson et al., 2011), HAT-P-54 b (e.g., Bakos et al., 2015), WASP-43 b (e.g., Esposito et al., 2017; Hellier et al., 2011), TrES-3 b (e.g., Christiansen et al., 2011; Sozzetti et al., 2009) and XO-2 N b (e.g., Damasso et al., 2015). The multi-band observations of transits have enable us to estimate the wavelength dependent physical parameters, such as planetary radius, with a better accuracy corresponding to each photometric band.

One of the most prominent noise component in the photometric light-curves is the time-uncorrelated noise (white noise), which consists of both photon noise and the fluctuations in the light curve due to the small spatial scale variability in the transparency of Earth's atmosphere, such as atmospheric scintillation (Föhring et al., 2019; Osborn et al., 2015). Most of the pre-processing techniques (such as binning and Gaussian smoothing) that can reduce the effect of these time-uncorrelated noise components also tend to distort the shape of the transit signal. The Wavelet Denoising technique (Cubillos et al., 2017; del Ser et al., 2018; Donoho & Johnstone, 1994; Luo & Zhang, 2012; Quan Pan et al., 1999; Waldmann, 2014) can be used to reduce the time-uncorrelated fluctuations in the light-curves without distorting the transit signal and improves the precision of the estimated physical parameters. Wavelet denoising technique also reduces the outliers in the light-curves due to cosmic ray events. In the present work, we have used this technique to pre-process the transit light curves with suitable optimizations in order to handle the multi-band data sets and a greater number of free parameters.

Another important noise component in the photometric signals is the time-correlated noise (red noise). We have reduced the large temporal scale red noise due to various instrumental and astrophysical effects by using the baseline correction

method. On the other hand, the time-correlated fluctuations in the light curves of short temporal scale are due to the small spatial scale variations that affect each object on a frame differently. The major sources of this kind of red noise is the small-scale activity and pulsation of the host stars. We address this red noise component by using Gaussian Process (GP) regression method (Barros et al., 2020; M. C. Johnson et al., 2015; Pereira et al., 2019; Rasmussen & Williams, 2006) to model it simultaneously while modelling for the transit signal.

In order to model the transit light curves, we have used the analytical formalism provided by Mandel and Agol (2002), which also incorporates the limb-darkening effect of the host-star using the quadratic limb darkening law. We have used the Markov Chain Monte Carlo (MCMC) method with the Metropolis-Hastings algorithm (Hastings, 1970) while modelling the transit light curves simultaneously along with the GP regression of the red noise. Although, the MCMC sampling technique is computationally expensive, it is extremely effective for modelling any noisy signal with a large number of free parameters.

As we have observed the transits in multiple wavebands, we have set the radius of a planet as a free parameter for each wavelength band corresponding to each filter used. This allows us to get a coarse estimation of the band-dependent radius of the planets. This can be helpful in characterising the planets by studying the broad atmospheric features, if any, in those ultra low-resolution transit spectra detected with the help of the model transmission spectra in optical and in near infrared regions (Chakrabarty & Sengupta, 2020; Sengupta et al., 2020).

For the simultaneous handling of multiple observed photometric data from different nights of observation and a smooth and streamlined implementation of all the state-of-the-art techniques for reduction, photometry, processing, and modelling of the light curves, we have used the software package developed by us. This Python-based package uses a semi-automated approach and the steps in this package aim at a precise estimation of the planetary properties from the transit light curves, which are at the same time robust, accurate, and reliable.

In section 2.2, we have described our observational details. In section 2.3, we have detailed our analysis and modelling techniques. In section 2.4, we have discussed the significance of our results and in section 2.5, we have concluded our study.

Table 2.1: Adopted physical properties of the exoplanets and their host-stars

	HAT-P-30 b	HAT-P-54 b	WASP-43 b	TrES-3 b	XO-2 N b
P [days]	2.810595	3.7998474	0.813475	1.30618608	2.61585922
	± 0.000005	± 0.000014	± 0.000001	± 0.00000038	± 0.00000028
K_{RV} [$m s^{-1}$]	88.1 ± 3.3	132.6 ± 4.9	551.0 ± 3.2	378.4 ± 9.9	90.17 ± 0.82
R_{\star} [R_{\odot}]	1.215 ± 0.051	0.617 ± 0.013	0.6506 ± 0.0054	0.829 ± 0.022	0.998 ± 0.033
M_{\star} [M_{\odot}]	1.242 ± 0.041	0.645 ± 0.020	0.688 ± 0.037	0.928 ± 0.048	0.96 ± 0.05
$T_{eff\star}$ [K]	6304 ± 88	4390 ± 50	4500 ± 100	5650 ± 75	5332 ± 57

Sources: HAT-P-30 b (J. A. Johnson et al., 2011), HAT-P-54 b (Bakos et al., 2015), WASP-43 b (Esposito et al., 2017; Hellier et al., 2011), TrES-3 b (Christiansen et al., 2011; Sozzetti et al., 2009), XO-2 N b (Damasso et al., 2015)

2.2 Target selection and observations

In this study we report the follow-up of five hot-Jupiters, e.g., HAT-P-30 b, HAT-P-54 b, WASP-43 b, TrES-3 b and XO-2 N b. The adopted physical properties of these exoplanets and their host-stars are listed in Table 2.1.

Our photometric observations are conducted using the 2m Himalayan Chandra Telescope (HCT) at Indian Astronomical Observatory, Hanle and the 1.3m J. C. Bhattacharya Telescope (JCBT) at Vainu Bappu Observatory, Kavalur. At HCT, the Hanle Faint Object Spectrograph Camera (HFOSC) has been used for photometric observations in V, R and I bands (Bessel), whereas the TIFR Near Infrared Spectrometer and Imager (TIRSPEC) has been used for the observations in J band. At JCBT, the UKATC optical CCD and the ProEM imagers have been used for the photometric observations at V, R and I bands. We have also made simultaneous observations of a few similar magnitude stars present within the photometric field of view of the target host-stars. These are used as reference stars for the differential photometry as described in the next section. The details of our observations have been listed in Table 2.2. Our observations have been optimised for mid-high cadence and high S/N. As can be seen from the table, the observations from JCBT have mean $S/N > 250$. On the other hand, the observations from HCT/HFOSC have very-high cadence and mean $S/N > 1000$.

Table 2.2: Details of the photometric observations

Target Name	Date	Telescope	Instrument	Filter	Frames	S/N (Mean)
HAT-P-30 b	2020-02-05	JCBT	UKATC	V	42	747.92
	2020-02-05	HCT	HFOSC	I	315	2002.55
	2020-02-22	HCT	HFOSC	R	233	1508.76
	2020-03-10	JCBT	UKATC	I	50	482.48
	2020-03-24	JCBT	UKATC	V	22	747.37
HAT-P-54 b	2020-01-15	JCBT	UKATC	I	24	570.82
	2020-02-03	JCBT	UKATC	I	56	410.26
	2020-02-03	HCT	HFOSC	V	160	1001.14
	2020-02-22	HCT	HFOSC	R	93	1544.17
WASP-43 b	2019-03-06	JCBT	UKATC	V	85	379.06
	2019-04-02	JCBT	UKATC	V	93	390.22
	2019-04-11	JCBT	UKATC	R	54	606.31
	2019-12-31	HCT	HFOSC	I	261	1264.00
	2020-02-05	HCT	TIRSPEC	J	232	226.06
	2020-02-14	JCBT	UKATC	R	31	662.59
TrES-3 b	2019-02-18	JCBT	UKATC	I	96	283.19
	2019-05-03	JCBT	UKATC	R	50	337.95
	2020-03-31	JCBT	UKATC	I	26	537.23
	2020-09-21	HCT	HFOSC	V	203	1447.40
XO-2 N b	2020-01-28	JCBT	UKATC	I	54	710.21
	2020-02-05	HCT	HFOSC	V	292	1789.22
	2020-02-18	JCBT	ProEM	I	40	782.06
	2020-02-18	HCT	HFOSC	R	622	1261.56
	2020-03-23	JCBT	UKATC	I	27	699.05

2.3 Data reduction and analysis

We have reduced the raw photometric data to obtain the transit light curves, which are then processed through several techniques to reduce the noises from various sources. We have then modelled the processed light curves in order to obtain the transit parameters. These parameters are then used to derive a few other physical properties of the exoplanets. For the whole process of data reduction and analysis, we have used our software package, which is written in Python programming language and uses several open-source software libraries. A detailed explanation of our methodology is given in the following subsections.

2.3 Data reduction and differential photometry

Our observational data obtained at each night, consists of a large number of photometric frames which are reduced through our automatic pipeline that uses the standard PyRAF (IRAF) libraries in the back-end. The raw photometric data are first calibrated using the bias and flat frames obtained during the respective nights of observations. Since, all the instruments used in our observations are cooled up to -70°C , the dark noise is found to be negligible. The calibrated frames are used to obtain the flux from our target host-stars and the reference field stars using aperture photometry. We have calculated the photometric noise precisely using the formula:

$$N = \sqrt{f/g + a \times s^2 + a^2 \times s^2/k} \quad (2.1)$$

where, f is sky-subtracted flux of the target object, s is the standard deviation of the counts on the region of the sky surrounding the object, g is gain of the instrument, a is the area of aperture of the object chosen in square pixels, and k is number of sky pixels. We have converted the time scale to BJD-TDB using the `utc2bjd` online applet (Eastman et al., 2010).

The observations from the ground-based telescopes are heavily affected by the varying atmospheric transparency and air-mass effect which can be reduced using the differential photometry method. We have used the flux of the reference field stars with the best S/N and minimum differential fluctuations for the differential photometry of our target host-stars and obtained the photometric transit light-curves.

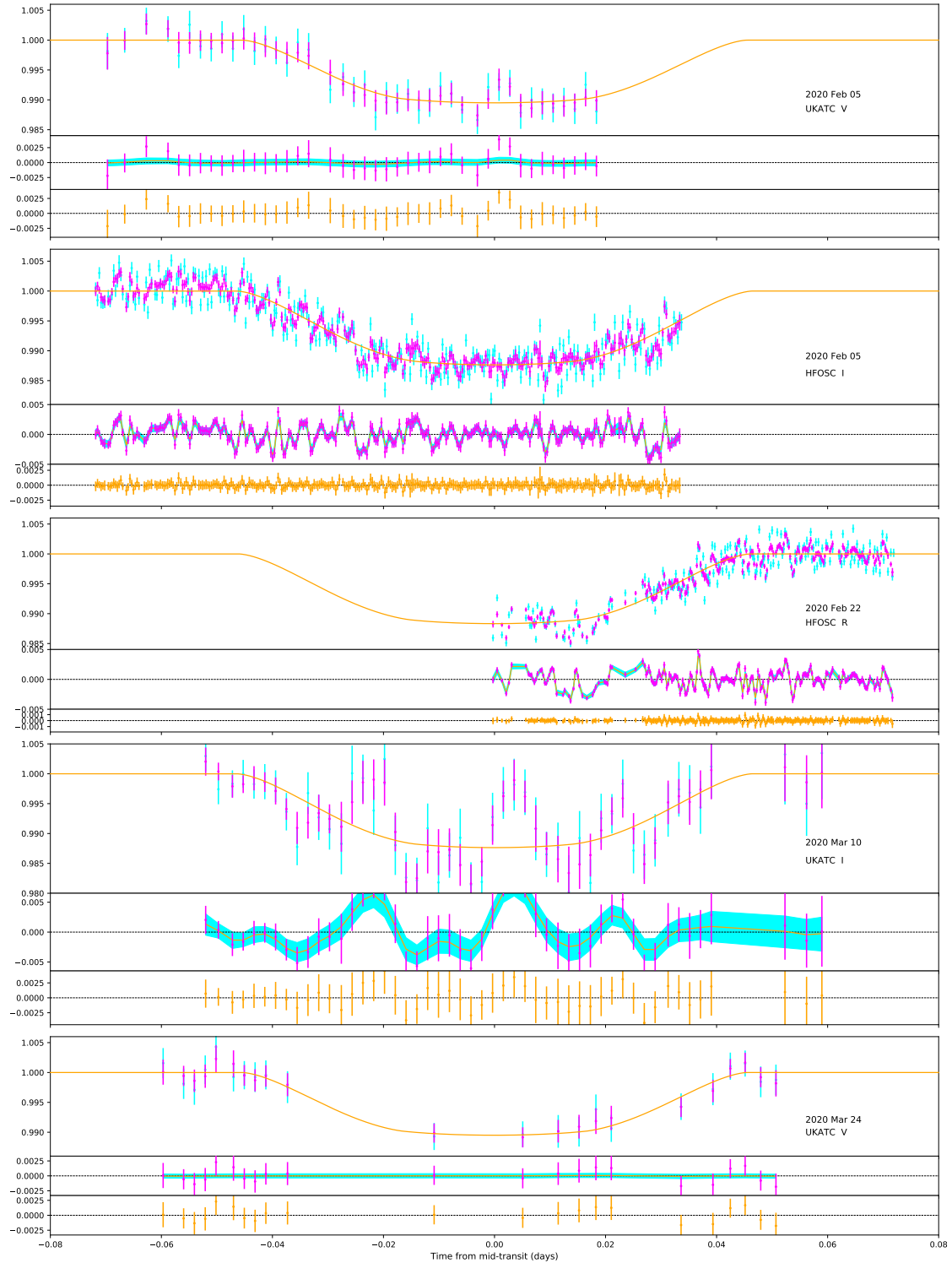


Figure 2.1: Observational and modelled light curves for HAT-P-30 b. For each observed transit event (see Table 2.2), the observation date, the instrument, and the photometric filter used are mentioned. Top: the unprocessed light curve (cyan), light curve after Wavelet Denoising (magenta), the best-fit transit model (orange). Middle: the residual after modelling without GP regression (magenta), the mean (orange) and $1\text{-}\sigma$ interval (cyan) of the best-fit GP regression model. Bottom: mean residual flux (orange).

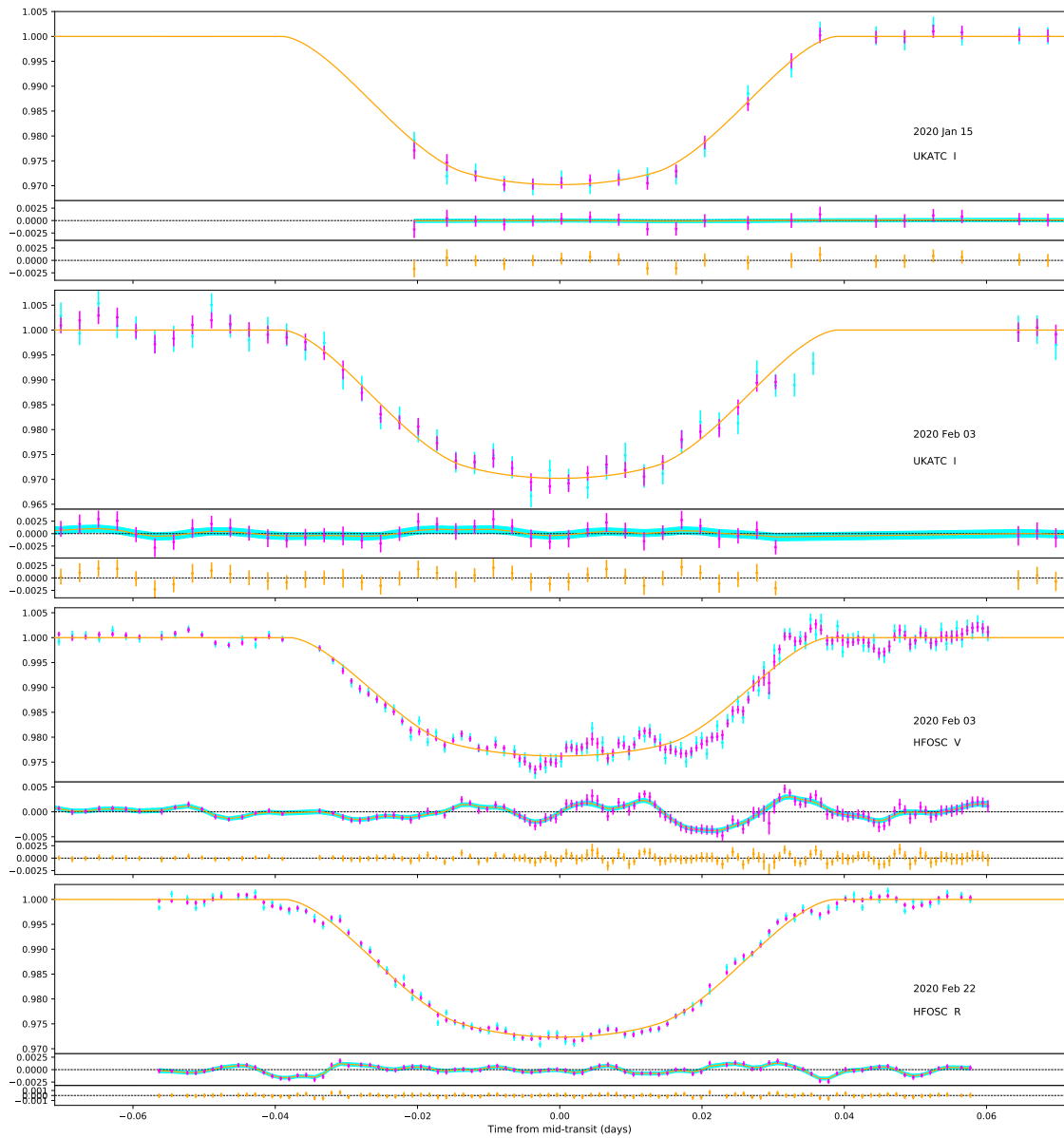


Figure 2.2: Same as Figure 2.1, but for HAT-P-54 b

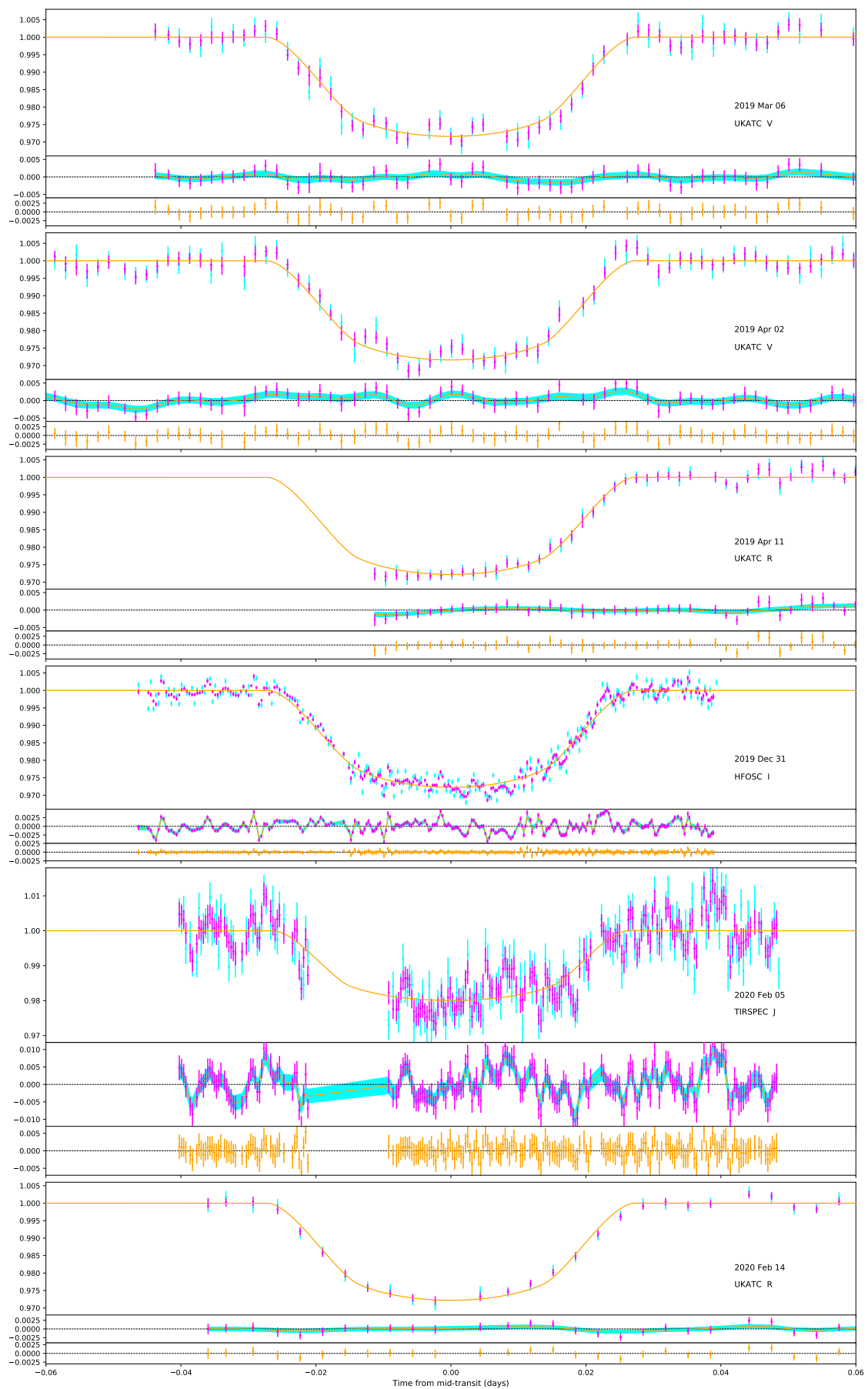


Figure 2.3: Same as Figure 2.1, but for WASP-43 b

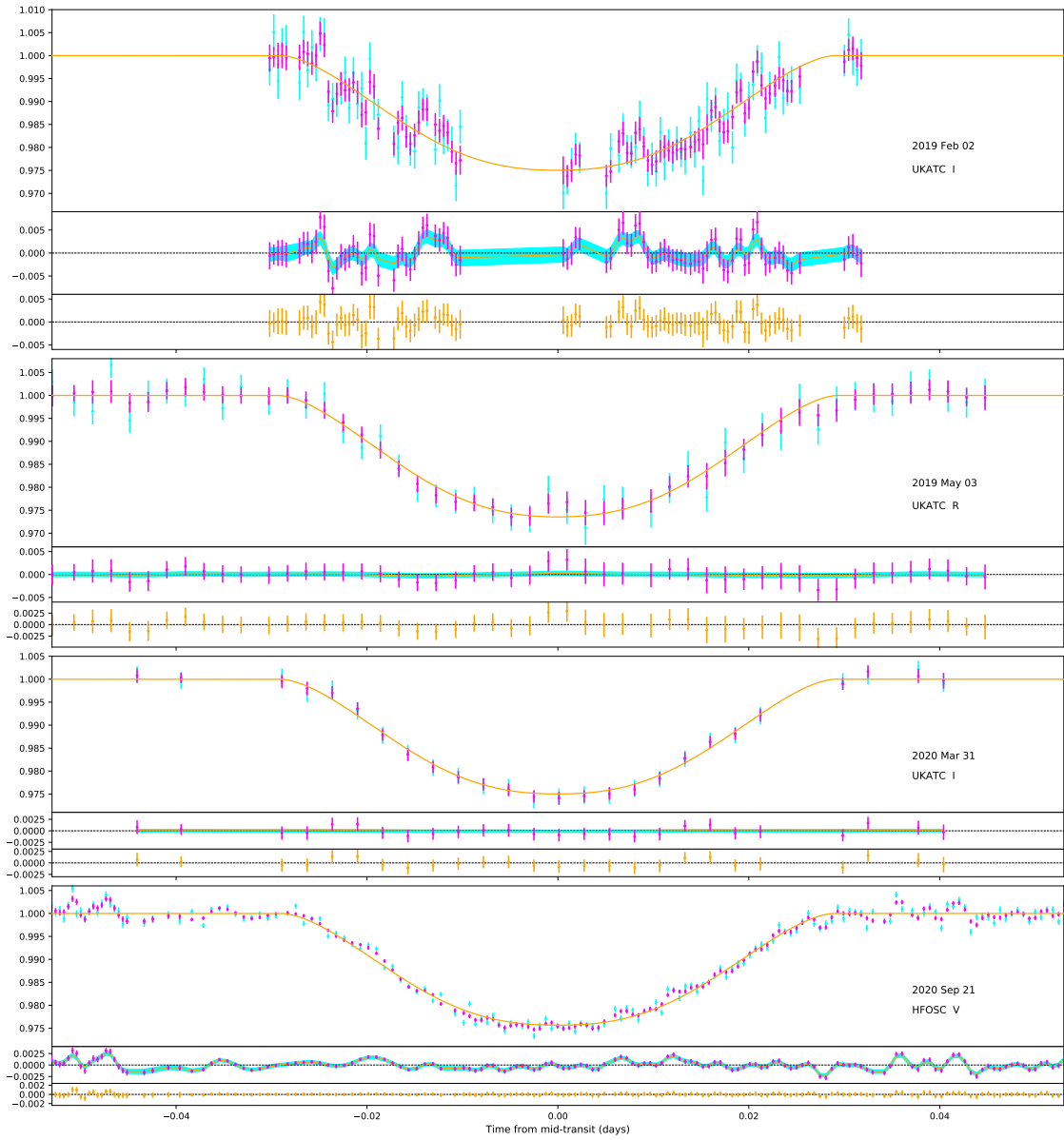


Figure 2.4: Same as Figure 2.1, but for TrES-3 b

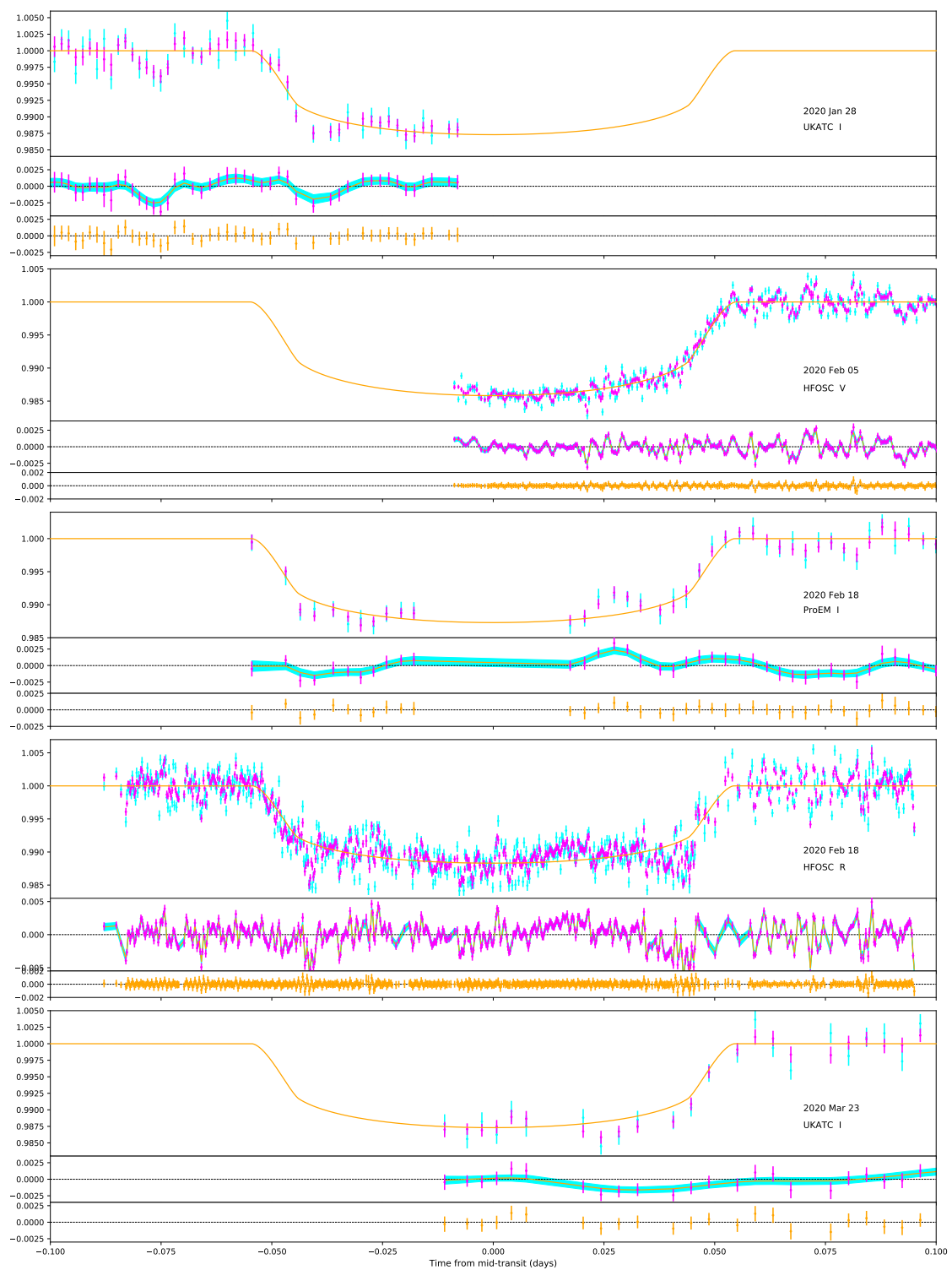


Figure 2.5: Same as Figure 2.1, but for XO-2 N b

2.3 Baseline correction

The red noise of large temporal scale (i.e., more than the characteristic scale of transit durations), which are mainly due to various instrumental effects and long-term stellar variability, results in a non-flat baseline for the photometric signals. One way to address this noise component is to model it using simple polynomial fits alongside the transits and subtract from the light-curves. However, it risks a potential bias in the estimated parameters due to the large scale nature of these noise components, and an increment in the parameter load in the already heavily populated model parameter space for MCMC sampling (see Section 2.3.5).

We have, therefore, performed the baseline correction before modelling for the transit signals. We have used linear and quadratic polynomials of time to model the out-of-transit part of the light-curves and chosen the one with the least BIC (Bayesian Information Criterion) (Schwarz, 1978) for the baseline correction. Use of only the out-of-transit portion of the light curves for baseline modelling removes the risk of the low-mid temporal scale variations in transit signal influencing the determination of baseline coefficients. Hence, it removes the risk of potential manipulation in the estimated transit parameters. The normalised baseline corrected transit light-curves from our observations are shown in Figure 2.1-2.5.

2.3 Wavelet Denoising

The time-uncorrelated noise (white noise) in the photometric signal also consists of the fluctuations in the light curve due to the small spatial scale variability in the transparency of the Earth's atmosphere. The presence of such fluctuations are more evident in the high-cadence photometric observations due to a better temporal resolution. They can severely affect both accuracy and precision of the estimated transit properties from those light curves. The white noise component cannot be totally removed from a signal and should be only reduced cautiously without distorting the informative part of the signal. Hence, instead of smoothing the light curves with some low-pass filter, we used a more robust technique, namely the Wavelet Denoising (Donoho & Johnstone, 1994; Luo & Zhang, 2012; Quan Pan et al., 1999). Although wavelet based denoising techniques have been widely used in image processing and remote sensing in various fields of science and engineering, it is a recent addition in the context of transit photometry and other light curve analysis (e.g., Cubillos et al., 2017; del Ser et al., 2018; Waldmann, 2014).

Wavelet Denoising consists of mainly three steps: deconstruction of the original signal into wavelet coefficients using discrete wavelet transform, thresholding, and reconstruction of the signal from the thresholded coefficients. We have used the PyWavelets (Lee et al., 2019) python package to perform the single level discrete wavelet transform of our photometric light-curves. In this process, we have used the Symlet family of wavelets, which are the least asymmetric modified version of Daubechies wavelets. A single level transform removes the risk of excess denoising. We have calculated the threshold value using the universal thresholding law (Donoho & Johnstone, 1994) given as;

$$Th = \sigma \sqrt{2 \log_e(N)} \quad (2.2)$$

where $\sigma = |median(D_x)|/0.6745$, and performed the hard thresholding, where the wavelet coefficients with absolute values less than the threshold value are replaced with it. The advantage behind universal threshold is that the risk of thresholding is small enough to satisfy the requirement of most applications. The threshold coefficients are then used to construct the denoised signal. The transit light curves after Wavelet Denoising are shown in Figure 2.1-2.5.

2.3 Gaussian Process Regression

The small-mid temporal scale red noise, which are correlated in time, form the major source of the remaining reducible noise components in our transit light curves after the Wavelet Denoising. This noise is primarily due to the small-scale activity of the host stars. To reduce this noise component, we have used the Gaussian Process (GP) regression (Barros et al., 2020; M. C. Johnson et al., 2015; Pereira et al., 2019; Rasmussen & Williams, 2006) technique.

We have modelled the time-correlated noise in the transit light-curves using GP regression alongside modelling for the transit signals, using the Markov Chain Monte Carlo (MCMC) technique (see Section 2.3.5). In order to treat the photometric noise in our observed light-curves while modelling for time-correlated noise, we have followed the regression formalism as given by Rasmussen and Williams (2006) for noisy observations. In this process, we have used the Matérn class covariance function with parameter of covariance, $\nu = 3/2$, and two free parameters, e.g., the signal standard deviation α and the characteristic length scale τ , which are used as model parameters in the MCMC sampling.

2.3 Markov Chain Monte Carlo sampling

In the final phase of our analysis of the transit light-curves, we have modelled them to the analytical transit formulation following Mandel and Agol (2002), which also incorporates the limb darkening effect of the host-star using the quadratic limb-darkening law given by,

$$I(\mu) = 1 - C_1(1 - \mu) - C_2(1 - \mu)^2 \quad (2.3)$$

We have used the MCMC sampling technique for this modelling, and simultaneously modelled for the time-correlated noise in the signal using the GP regression method as explained in section 2.3.4. The model parameters in MCMC includes the transit parameters: (i) mid-transit time T , (ii) the impact-parameter b , (iii) the scaled stellar radius R_\star/a , (iv) the ratio of planet to stellar radius R_p/R_\star , (v) the out-of-transit flux f_o , (vi) the limb darkening coefficients C_1 and C_2 ; and (vii) the GP regression coefficients α and τ . The orbital periods have been kept constant and are adopted from previous studies as given in Table 2.1. We have followed Sing (2010) for the prior values of the quadratic limb-darkening coefficients.

We have modelled all the transit light-curves corresponding to each of our target exoplanets simultaneously keeping the transit independent parameters the same for all transit events of the same target and keeping the wavelength dependent parameters same across those transit events observed using the same photometric filters. We have used the Metropolis-Hastings algorithm (Hastings, 1970) in MCMC sampling and used the modified marginal likelihood function due to the inclusion of the GP regression technique (Rasmussen & Williams, 2006). In MCMC sampling for each of our targets, we have used 30 walkers and 100,000 iterations for each independent walker. Such a large volume of sampling is done in order to handle the large number of model parameters and high volume of photometric data under simultaneous modelling of multiple transit events. The aim has been to assess the robustness of the convergence of the sampling parameters such that a high accuracy in the derived parameters is achieved. Such a large computation is practically impossible without the incursion of parallel computing. For this purpose, our software package for modelling and data analysis has been facilitated with parallel computing using the Python-based *multiprocessing* library. We have used the high performance computing facility (NOVA) at Indian Institute of Astrophysics (IIA) for our numerical computation. We have discarded the first 10,000 iterations for each walkers as burn-in and accepted the rest 90,000 iterations for obtaining the

posterior distributions. We have shown the corner diagrams depicting the posterior distributions of the transit parameters and the GP regression coefficients from our MCMC sampling in Figures 2.6-2.10.

We present the best-fit transit models, best-fit GP regression model, and the mean residual fluxes in Figures 2.1-2.5. The estimated values of the physical properties for our target exoplanets with 1σ error have been given in Table 2.3-2.7 and the estimated values of mid-transit times along with the GP regression coefficients for each transit light-curves have been given in Table 2.8.

2.3 Derived parameters

The posterior distribution of the transit parameters from the MCMC sampling along with the adopted physical properties of the target exoplanets and the host stars as given in Table 2.1 are used to estimate the values of some other physical parameters.

We have estimated the transit duration T_{14} for each of our targets at each photometric band using the relation,

$$T_{14} = \frac{P}{\pi} \sin^{-1} \left(\frac{\sqrt{(1+R_p/R_\star)^2 - b^2}}{\sqrt{(a/R_\star)^2 - b^2}} \right) \quad (2.4)$$

The inclination angle of the planetary orbit i is estimated using the relation,

$$i = \cos^{-1} \left(\frac{bR_\star}{a} \right) \quad (2.5)$$

We have estimated the mass M_p and the equilibrium temperature T_{eq} of the target exoplanets using the relations,

$$M_p = M_\star^{2/3} \left(\frac{P}{2\pi G} \right)^{1/3} \frac{K_{RV}}{\sin i} \quad (2.6)$$

and

$$T_{eq} = T_{eff} \sqrt{\frac{R_\star}{2a}} \quad (2.7)$$

For all the cases, we have assumed circular orbits, zero Bond albedo, and full re-circulation of the incident stellar flux over the planetary surface. The estimated values of all the derived physical properties for each of our targeted exoplanets are given in the Table 2.3-2.7.

Table 2.3: Estimated values of physical parameters for HAT-P-30 b

Parameter	Filter	This work	J. A. Johnson et al. (2011)
Transit parameters			
b		$0.8546^{+0.0041}_{-0.0055}$	$0.854^{+0.008}_{-0.010}$
R_{\star}/a		$0.1430^{+0.0013}_{-0.0012}$	0.1348 ± 0.0047
R_p/R_{\star}	V	$0.10753^{+0.00180}_{-0.00165}$	$0.1134 \pm 0.002^{\dagger}$
	R	$0.11346^{+0.00193}_{-0.00165}$	
	I	$0.11683^{+0.00110}_{-0.00104}$	
Limb-darkening coefficients			
C_1	V	$0.329^{+0.020}_{-0.020}$	0.1975^{\dagger}
	R	$0.329^{+0.020}_{-0.020}$	
	I	$0.329^{+0.020}_{-0.020}$	
C_2	V	$0.280^{+0.020}_{-0.020}$	0.3689^{\dagger}
	R	$0.280^{+0.020}_{-0.020}$	
	I	$0.279^{+0.021}_{-0.019}$	
Derived parameters			
T_{14} [hr]	V	$2.186^{+0.025}_{-0.022}$	$2.129 \pm 0.036^{\dagger}$
	R	$2.213^{+0.025}_{-0.021}$	
	I	$2.223^{+0.024}_{-0.021}$	
a/R_{\star}		$6.994^{+0.060}_{-0.062}$	7.42 ± 0.26
i [deg]		$82.982^{+0.082}_{-0.087}$	83.6 ± 0.4
M_p [M_J]		$0.712^{+0.031}_{-0.031}$	0.711 ± 0.028
M_p [M_{\oplus}]		$226.2^{+9.8}_{-9.7}$	226.0 ± 8.9
T_{eq} [K]		$1686.1^{+24.8}_{-24.7}$	1630 ± 42
a [AU]		$0.03948^{+0.00170}_{-0.00169}$	0.0419 ± 0.0005
R_p [R_J]	V	$1.2995^{+0.0482}_{-0.0481}$	$1.340 \pm 0.065^{\dagger}$
	R	$1.3720^{+0.0505}_{-0.0495}$	
	I	$1.4122^{+0.0482}_{-0.0480}$	
R_p [R_{\oplus}]	V	$14.566^{+0.540}_{-0.539}$	$15.02 \pm 0.73^{\dagger}$
	R	$15.379^{+0.566}_{-0.555}$	
	I	$15.829^{+0.541}_{-0.538}$	

 \dagger value doesn't corresponds to the mentioned wavelength filter.

Table 2.4: Estimated values of physical parameters for HAT-P-54 b

Parameter	Filter	This work	Bakos et al. (2015)
Transit parameters			
b		$0.7599^{+0.0060}_{-0.0054}$	$0.741^{+0.010}_{-0.011}$
R_{\star}/a		$0.07175^{+0.00098}_{-0.00072}$	0.0697 ± 0.001
R_p/R_{\star}	V	$0.15616^{+0.00204}_{-0.00214}$	0.1572 ± 0.002 †
	R	$0.16898^{+0.00115}_{-0.00082}$	
	I	$0.17516^{+0.00176}_{-0.00165}$	
Limb-darkening coefficients			
C_1	V	$0.627^{+0.043}_{-0.026}$	0.4324 †
	R	$0.685^{+0.017}_{-0.035}$	
	I	$0.630^{+0.041}_{-0.028}$	
C_2	V	$0.080^{+0.007}_{-0.007}$	0.2457 †
	R	$0.080^{+0.006}_{-0.007}$	
	I	$0.079^{+0.007}_{-0.006}$	
Derived parameters			
T_{14} [hr]	V	$1.819^{+0.021}_{-0.017}$	1.797 ± 0.017 †
	R	$1.855^{+0.020}_{-0.017}$	
	I	$1.872^{+0.021}_{-0.018}$	
a/R_{\star}		$13.94^{+0.14}_{-0.19}$	14.34 ± 0.22
i [deg]		$86.873^{+0.046}_{-0.057}$	87.040 ± 0.084
M_p [M_J]		$0.761^{+0.032}_{-0.032}$	0.760 ± 0.032
M_p [M_{\oplus}]		$241.8^{+10.3}_{-10.1}$	242 ± 10
T_{eq} [K]		$832.0^{+10.9}_{-10.8}$	818 ± 12
a [AU]		$0.03994^{+0.00098}_{-0.00098}$	0.04117 ± 0.00043
R_p [R_J]	V	$0.9796^{+0.0329}_{-0.0330}$	0.944 ± 0.028 †
	R	$1.0611^{+0.0333}_{-0.0332}$	
	I	$1.0997^{+0.0362}_{-0.0357}$	
R_p [R_{\oplus}]	V	$10.980^{+0.369}_{-0.370}$	10.6 ± 0.3 †
	R	$11.894^{+0.374}_{-0.372}$	
	I	$12.327^{+0.406}_{-0.401}$	

† value doesn't corresponds to the mentioned wavelength filter.

Table 2.5: Estimated values of physical parameters for WASP-43 b

Parameter	Filter	This work	Esposito et al. (2017)
Transit parameters			
b		$0.6810^{+0.0054}_{-0.0058}$	0.689 ± 0.013
R_{\star}/a		$0.2182^{+0.0018}_{-0.0017}$	0.2012 ± 0.0057
R_p/R_{\star}	V	$0.16442^{+0.00152}_{-0.00156}$	$0.1588 \pm 0.004^{\dagger}$
	R	$0.16268^{+0.00178}_{-0.00142}$	
	I	$0.16214^{+0.00123}_{-0.00121}$	
	J	$0.1375^{+0.0035}_{-0.0032}$	
Limb-darkening coefficients			
C_1	V	$0.627^{+0.041}_{-0.026}$	0.66^{\dagger}
	R	$0.632^{+0.041}_{-0.029}$	
	I	$0.680^{+0.021}_{-0.036}$	
	J	$0.643^{+0.042}_{-0.037}$	
C_2	V	$0.079^{+0.007}_{-0.007}$	
	R	$0.079^{+0.007}_{-0.006}$	
	I	$0.081^{+0.006}_{-0.007}$	
	J	$0.080^{+0.007}_{-0.006}$	
Derived parameters			
T_{14} [hr]	V	$1.3046^{+0.0091}_{-0.0086}$	$1.164 \pm 0.24^{\dagger}$
	R	$1.3016^{+0.0099}_{-0.0089}$	
	I	$1.3010^{+0.0091}_{-0.0094}$	
	J	$1.2583^{+0.0102}_{-0.0118}$	
a/R_{\star}		$4.584^{+0.036}_{-0.037}$	4.97 ± 0.14
i [deg]		$81.46^{+0.12}_{-0.13}$	82.109 ± 0.088
M_p [M_J]		$1.994^{+0.072}_{-0.073}$	1.998 ± 0.079
M_p [M_{\oplus}]		$633.9^{+22.7}_{-23.1}$	635.0 ± 25.1
T_{eq} [K]		$1486.3^{+33.5}_{-33.5}$	1426.7 ± 8.5
a [AU]		$0.01387^{+0.00016}_{-0.00016}$	0.01504 ± 0.00029
R_p [R_J]	V	$1.1006^{+0.0599}_{-0.0598}$	$1.006 \pm 0.017^{\dagger}$
	R	$1.0900^{+0.0595}_{-0.0593}$	
	I	$1.0857^{+0.0587}_{-0.0586}$	
	J	$0.9199^{+0.0546}_{-0.0539}$	
R_p [R_{\oplus}]	V	$12.336^{+0.671}_{-0.670}$	$11.61 \pm 0.21^{\dagger}$
	R	$12.218^{+0.667}_{-0.664}$	
	I	$12.169^{+0.658}_{-0.657}$	
	J	$10.311^{+0.612}_{-0.604}$	

 \dagger value doesn't corresponds to the mentioned wavelength filter.

Table 2.6: Estimated values of physical parameters for TrES-3 b

Parameter	Filter	This work	Sozzetti et al. (2009)
Transit parameters			
b		$0.8317^{+0.0040}_{-0.0047}$	0.84 ± 0.01
R_{\star}/a		$0.1681^{+0.0021}_{-0.0020}$	0.1687 ± 0.0016
R_p/R_{\star}	V	$0.16483^{+0.00076}_{-0.00081}$	$0.1655 \pm 0.002^{\dagger}$
	R	$0.17226^{+0.00192}_{-0.00215}$	
	I	$0.16704^{+0.00261}_{-0.00177}$	
Limb-darkening coefficients			
C_1	V	$0.454^{+0.024}_{-0.027}$	0.4378
	R	$0.447^{+0.028}_{-0.025}$	
	I	$0.448^{+0.027}_{-0.026}$	
C_2	V	$0.251^{+0.013}_{-0.013}$	0.2933
	R	$0.249^{+0.014}_{-0.013}$	
	I	$0.250^{+0.013}_{-0.013}$	
Derived parameters			
T_{14} [hr]	V	$1.387^{+0.015}_{-0.015}$	
	R	$1.405^{+0.016}_{-0.016}$	
	I	$1.393^{+0.014}_{-0.015}$	
a/R_{\star}		$5.948^{+0.072}_{-0.073}$	5.926 ± 0.056
i [deg]		$81.96^{+0.13}_{-0.13}$	81.85 ± 0.16
M_p [M_J]		$1.954^{+0.085}_{-0.084}$	$1.91^{+0.075}_{-0.080}$
M_p [M_{\oplus}]		$621.1^{+26.9}_{-26.6}$	$607.030^{+23.836}_{-25.425}$
T_{eq} [K]		$1638.3^{+24.1}_{-24.0}$	
a [AU]		$0.02293^{+0.00068}_{-0.00067}$	$0.02282^{+0.00023}_{-0.00040}$
R_p [R_J]	V	$1.4881^{+0.0770}_{-0.0768}$	$1.336^{+0.031}_{-0.037}{}^{\dagger}$
	R	$1.5555^{+0.0830}_{-0.0823}$	
	I	$1.5108^{+0.0802}_{-0.0796}$	
R_p [R_{\oplus}]	V	$16.680^{+0.863}_{-0.860}$	$14.975^{+0.347}_{-0.415}{}^{\dagger}$
	R	$17.434^{+0.930}_{-0.922}$	
	I	$16.935^{+0.899}_{-0.892}$	

 \dagger value doesn't corresponds to the mentioned wavelength filter.

Table 2.7: Estimated values of physical parameters for XO-2 N b

Parameter	Filter	This work	Damasso et al. (2015)
Transit parameters			
b		$0.1993^{+0.0239}_{-0.0295}$	$0.287^{+0.043}_{-0.055}$
R_{\star}/a		$0.1204^{+0.0010}_{-0.0008}$	0.1261 ± 0.0017
R_p/R_{\star}	V	$0.10702^{+0.00064}_{-0.00062}$	$0.1049^{+0.00059 \dagger}_{-0.00063}$
	R	$0.09797^{+0.00052}_{-0.00039}$	
	I	$0.10164^{+0.00153}_{-0.00148}$	
Limb-darkening coefficients			
C_1	V	$0.503^{+0.030}_{-0.032}$	$0.474^{+0.030 \dagger}_{-0.028}$
	R	$0.466^{+0.023}_{-0.011}$	
	I	$0.487^{+0.036}_{-0.026}$	
C_2	V	$0.201^{+0.013}_{-0.014}$	$0.171^{+0.067 \dagger}_{-0.070}$
	R	$0.194^{+0.015}_{-0.010}$	
	I	$0.199^{+0.014}_{-0.013}$	
Derived parameters			
T_{14} [hr]	V	$2.628^{+0.018}_{-0.016}$	$2.7024 \pm 0.006 \dagger$
	R	$2.606^{+0.018}_{-0.016}$	
	I	$2.615^{+0.018}_{-0.017}$	
a/R_{\star}		$8.308^{+0.059}_{-0.072}$	$7.928^{+0.099}_{-0.093}$
i [deg]		$88.63^{+0.21}_{-0.17}$	$87.96^{+0.42}_{-0.34}$
M_p [M_J]		$0.595^{+0.021}_{-0.021}$	0.597 ± 0.021
M_p [M_{\oplus}]		$189.1^{+6.7}_{-6.8}$	189.737 ± 6.674
T_{eq} [K]		$1308.4^{+14.9}_{-14.8}$	
a [AU]		$0.0385^{+0.0013}_{-0.0013}$	0.03673 ± 0.00064
R_p [R_J]	V	$0.9996^{+0.0522}_{-0.0521}$	$1.019 \pm 0.031 \dagger$
	R	$0.9155^{+0.0477}_{-0.0476}$	
	I	$0.9492^{+0.0513}_{-0.0509}$	
R_p [R_{\oplus}]	V	$11.264^{+0.585}_{-0.584}$	$11.422 \pm 0.347 \dagger$
	R	$10.262^{+0.534}_{-0.534}$	
	I	$10.640^{+0.575}_{-0.571}$	

† value doesn't corresponds to the mentioned wavelength filter.

Table 2.8: Mid-transit times and GP regression parameters for each observed transit event

Target Name	Date	Instrument/Filter	Mid-transit time [BJD-TDB]	α	τ
HAT-P-30 b	2020-02-05	UKATC/V	2458885.401561 ^{+0.001551} _{-0.001481}	0.00054 ^{+0.00019} _{-0.00020}	0.0582 ^{+0.0219} _{-0.0264}
	2020-02-05	HFOSC/I	2458885.401169 ^{+0.000696} _{-0.000772}	0.00158 ^{+0.00009} _{-0.00009}	0.0263 ^{+0.0010} _{-0.0008}
	2020-02-22	HFOSC/R	2458902.265187 ^{+0.000822} _{-0.000976}	0.00159 ^{+0.00015} _{-0.00011}	0.0240 ^{+0.0009} _{-0.0011}
HAT-P-54 b	2020-03-10	UKATC/I	2458919.128141 ^{+0.002098} _{-0.001620}	0.00358 ^{+0.00045} _{-0.00042}	0.0650 ^{+0.0055} _{-0.0042}
	2020-03-24	UKATC/V	2458933.175811 ^{+0.001766} _{-0.001794}	0.00036 ^{+0.00024} _{-0.00021}	0.0825 ^{+0.0447} _{-0.0592}
	2020-01-15	UKATC/I	2458864.201261 ^{+0.000374} _{-0.000410}	0.00035 ^{+0.00026} _{-0.00021}	0.1007 ^{+0.0492} _{-0.0437}
	2020-02-03	UKATC/I	2458883.204510 ^{+0.000427} _{-0.000402}	0.00095 ^{+0.00039} _{-0.00039}	0.0642 ^{+0.0212} _{-0.0149}
WASP-43 b	2020-02-03	HFOSC/V	2458883.204556 ^{+0.000331} _{-0.000437}	0.00151 ^{+0.00017} _{-0.00016}	0.0711 ^{+0.0069} _{-0.0050}
	2020-02-22	HFOSC/R	2458902.203596 ^{+0.000231} _{-0.000308}	0.00091 ^{+0.00011} _{-0.00009}	0.0564 ^{+0.0044} _{-0.0048}
	2019-03-06	UKATC/V	2458549.296039 ^{+0.000334} _{-0.000409}	0.00112 ^{+0.00032} _{-0.00023}	0.0581 ^{+0.0178} _{-0.0129}
	2019-04-02	UKATC/V	2458576.140878 ^{+0.000294} _{-0.000322}	0.00150 ^{+0.00022} _{-0.00029}	0.0613 ^{+0.0125} _{-0.0088}
	2019-04-11	UKATC/R	2458585.087944 ^{+0.000496} _{-0.000520}	0.00096 ^{+0.00043} _{-0.00029}	0.0548 ^{+0.0251} _{-0.0242}
	2019-12-31	HFOSC/I	2458849.468659 ^{+0.000188} _{-0.000166}	0.00171 ^{+0.00010} _{-0.00010}	0.0235 ^{+0.0009} _{-0.0010}
TrES-3 b	2020-02-05	TIRSPEC/J	2458885.259449 ^{+0.000789} _{-0.000911}	0.00407 ^{+0.00029} _{-0.00027}	0.0276 ^{+0.0018} _{-0.0017}
	2020-02-14	UKATC/R	2458894.207388 ^{+0.000255} _{-0.000365}	0.00675 ^{+0.00032} _{-0.00028}	0.0744 ^{+0.0029} _{-0.0022}
	2019-02-18	UKATC/I	2458533.473769 ^{+0.000382} _{-0.000400}	0.00223 ^{+0.00025} _{-0.00021}	0.0281 ^{+0.0035} _{-0.0032}
	2019-05-03	UKATC/R	2458607.351900 ^{+0.000405} _{-0.000402}	0.00051 ^{+0.00022} _{-0.00025}	0.0582 ^{+0.0248} _{-0.0242}
XO-2 N b	2020-03-31	UKATC/I	2458940.426286 ^{+0.000337} _{-0.000281}	0.00030 ^{+0.00021} _{-0.00018}	0.0854 ^{+0.0421} _{-0.0330}
	2020-09-21	HFOSC/V	2459114.150846 ^{+0.000216} _{-0.000244}	0.00105 ^{+0.00010} _{-0.00009}	0.0327 ^{+0.0010} _{-0.0011}
	2020-01-28	UKATC/I	2458877.220952 ^{+0.000550} _{-0.000626}	0.00151 ^{+0.00031} _{-0.00021}	0.0653 ^{+0.0088} _{-0.0084}
	2020-02-05	HFOSC/V	2458885.071089 ^{+0.000290} _{-0.000316}	0.00101 ^{+0.00006} _{-0.00006}	0.0288 ^{+0.0008} _{-0.0008}
	2020-02-18	ProEM/I	2458898.149337 ^{+0.000431} _{-0.000425}	0.00126 ^{+0.00029} _{-0.00030}	0.0896 ^{+0.0129} _{-0.0120}
2020-02-18	HFOSC/R	2458898.149390 ^{+0.000249} _{-0.000237}	0.00180 ^{+0.00005} _{-0.00004}	0.0238 ^{+0.0005} _{-0.0005}	
2020-03-23	UKATC/I	2458932.154930 ^{+0.000927} _{-0.000723}	0.00116 ^{+0.00031} _{-0.00030}	0.1501 ^{+0.0557} _{-0.0413}	

2.4 Results and Discussion

Our study involves the photometric follow up observations of five hot-Jupiters using a 1.3m (JCBT) and a 2m (HCT) class telescopes. Table 2.1 shows that the observations from HCT have a better S/N and time-cadence. This can be attributed to the large aperture of HCT, short readout time of the new CCD installed at the back-end (HFOSC2), and good observational condition at the site of IAO. However, the observations from JCBT also show good S/N and have been extremely useful in complementing the observations from the HCT. Since the number of nights allocated at each telescope is limited, we use both the telescopes for our observations.

Figure 2.1-2.5 demonstrate that the Wavelet Denoising technique is a useful tool for the reduction of the time-uncorrelated noise components and outliers from the transit light curves. Also, we have avoided excessive smoothing of the light-curves by cautiously choosing the decomposition levels and threshold levels while using this denoising technique.

The GP regression method has very effectively modelled the correlated noise components in the transit signal as shown in Figure 2.1 - 2.5. The origin of this correlated noise component is not only attributed to the low-scale variability of the exoplanet host-stars, but also to that of the reference stars used for differential photometry. Since, the reference stars are different in most of the cases, due to various observational reasons, the amplitude of the correlated noises are different for the same target host star. Similarly, the correlated noise components are negligible for some of the low-cadence observations from JCBT. Our analysis shows the efficiency of GP regression technique in reducing the correlated noise components irrespective of their origin and amplitude.

Our MCMC sampling includes a large number of sampling points, which is helpful to remove any bias from the choice of prior values in the MCMC, thereby resulting in an more accurate estimation of the free parameters. This is evident from the near-normal distribution of most of the model-parameter posterior distributions as shown in Figures 2.6-2.10. As can be seen from the estimated values of the mid-transit times of our observed transit events, the independently estimated mid-transit times for the same transit event observed from the two different telescopes (HCT and JCBT) in three different instances [2020-02-05 for HAT-P-30 b, 2020-02-03 for HAT-P-54 b and 2020-02-18 for XO-2 N b] are in perfect agreement with each other, with the error-bar in the estimated value from the HCT observation being small due to a better S/N. This proves the robustness of our analysis method in the estimation

of these properties.

Due to the multi-band observations of the transit events, we have been able to estimate the wavelength dependent radii of our target exoplanets with good accuracy at each band. Even though the site conditions at IAO allows observation in the infrared wavelengths, the S/N of the data observed using the TIRSPEC instrument at the back-end of HCT is significantly low, especially in the context of transit photometry. However, we managed to observe one frame in the J-band for WASP-43 b. Apart from this, all of the targets have been observed in V-, R- and I-bands. We will further analyse these results to check if any information can be excavated about the atmospheres of these planets with the help of the models we have developed for transmission spectra (Chakrabarty & Sengupta, 2020; Sengupta et al., 2020).

We have compared the estimated values of the physical parameters for the target exoplanets in our study with those from the previous studies (given in Tables 2.3-2.7) to understand the effectiveness of the critical noise reduction and modelling algorithm used in our study, and the improvement in the accuracy and precision in the parameter estimation. While for most of the parameters, the estimated values are in good accordance with those from previous studies, small differences in a few parameter values can be attributed to the improvement in the quality of the transit signals due to the use the noise reduction algorithms, thereby improving the accuracy in parameter estimation. Also, the precision in the estimated values of the transit parameters and the parameters which are directly derived from them have been improved up to 4 times compared to the previous studies, which is significant in the context of transit photometric studies of exoplanets. This improvement in the uncertainties in estimated parameters is due to a better S/N in our follow-up observations and further reduction of various noise components. On the other hand, the estimated values of other derived parameters, which are dependent upon the stellar properties of the host-stars for their estimation (adopted from the previous studies and given in Table 2.1), have seen no significant improvements in their precision. This is due to the large uncertainties embedded with those adopted values of stellar parameters.

2.5 Conclusion

In this study, we have performed new multi-band transit photometric follow-up of five hot-Jupiters, HAT-P-30 b, HAT-P-54 b, WASP-43 b, TrES-3 b and XO-2 N b, using the 2m Himalayan Chandra Telescope (HCT) at IAO, Hanle and the 1.3m J.

C. Bhattacharya Telescope (JCBT) at VBO, Kavalur. Taking the advantage of the larger apertures of these telescopes compared to those used for previous studies of these exoplanets, we have obtained transit light-curves with better S/N.

Our critical noise treatment analysis employs the Wavelet Denoising technique for the reduction of time-uncorrelated noise components from the photometric light curves without potential loss of signal due to transit origins and the Gaussian Process regression technique to effectively model and compensate for the time-correlated noise in the photometric signal simultaneously along with the transit modelling. We have used the Markov Chain Monte Carlo (MCMC) sampling technique by adopting the Metropolis-Hastings algorithm.

Due to the high S/N photometric follow-up observations as well as the adopted highly optimised noise reduction and analysis techniques, the estimated physical parameters from our study have a better accuracy and overall precision. Also, the follow-up using multiple photometric bands have enabled us to estimate accurately, the wavelength dependent physical properties which can be used as an outset for the high-resolution atmospheric characterisation of these exoplanets in future.

Our ongoing project of follow-up studies of the exoplanets can be extended for the study of other existing exoplanets in future. Also, the critical noise analysis algorithm can be used for the analysis of transit light curves from the existing and upcoming global exoplanet survey missions, such as the TESS (Transiting Exoplanet Survey Satellite), for the estimation of physical properties of the detected exoplanets with better accuracy, which have been discussed in the next chapter.

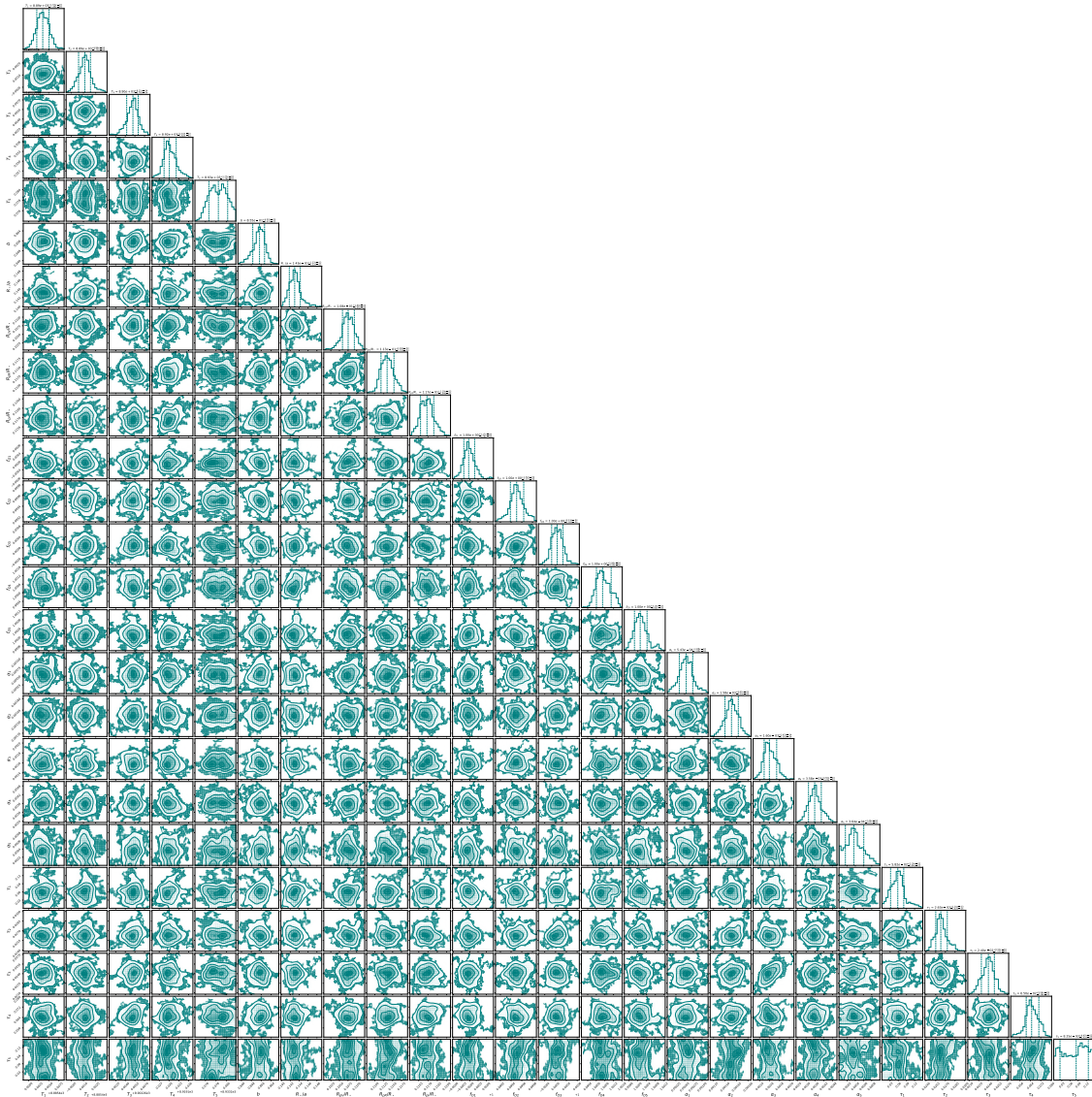


Figure 2.6: Corner diagram depicting the posterior distributions of the transit parameters and the GP regression coefficients from MCMC sampling for HAT-P-30 b.

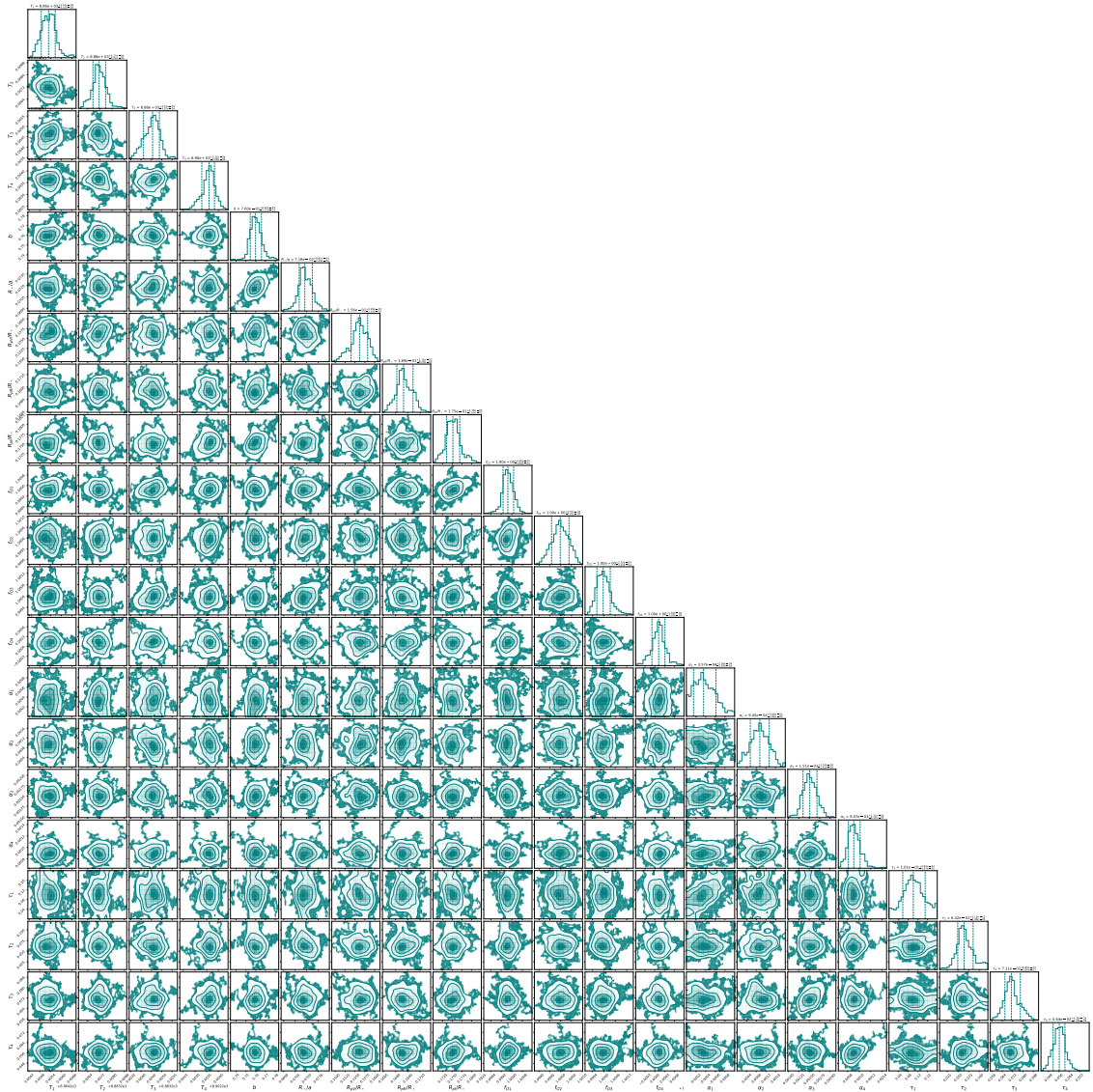


Figure 2.7: Same as Figure 2.6, but for HAT-P-54 b

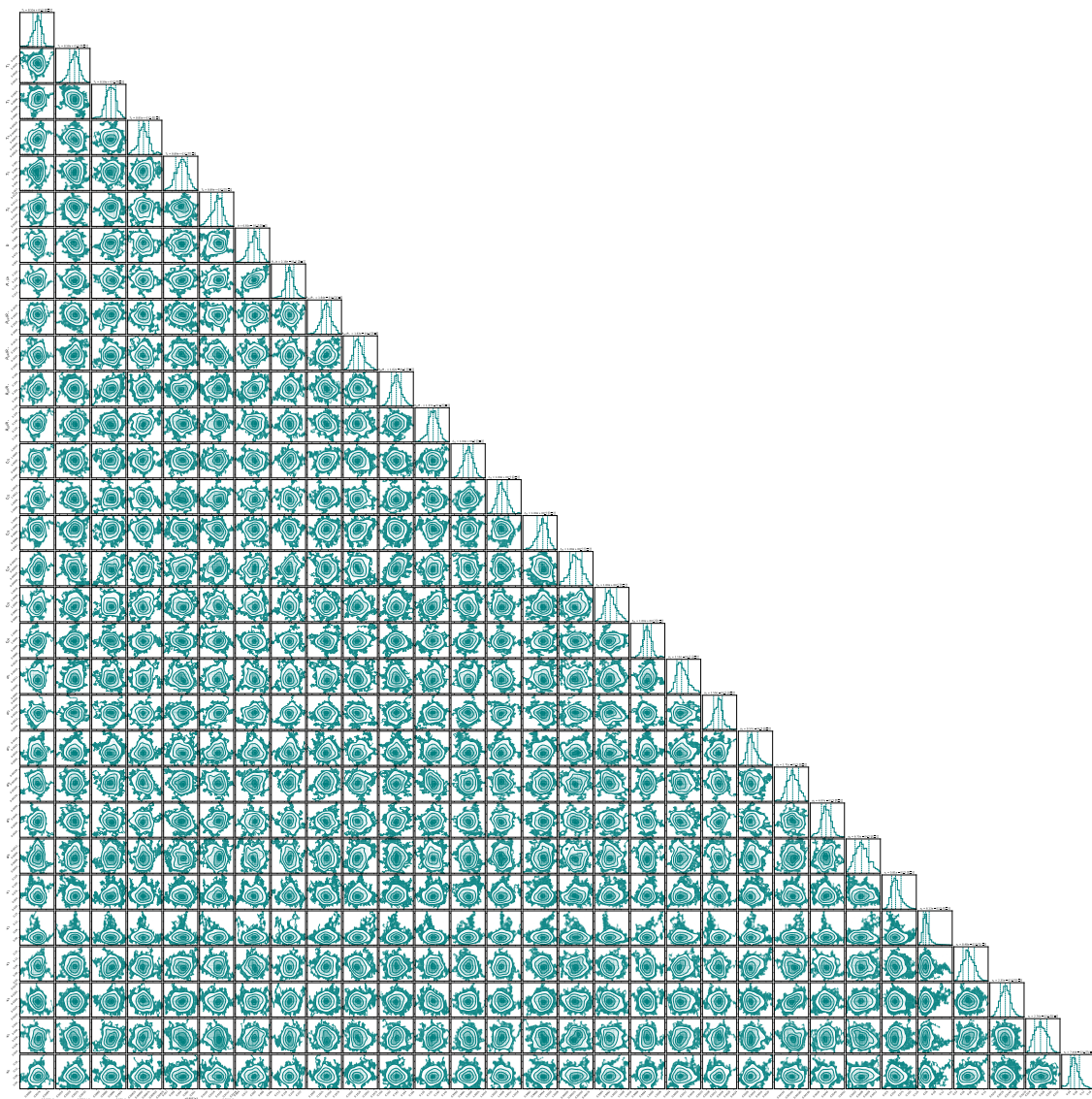


Figure 2.8: Same as Figure 2.6, but for WASP-43 b

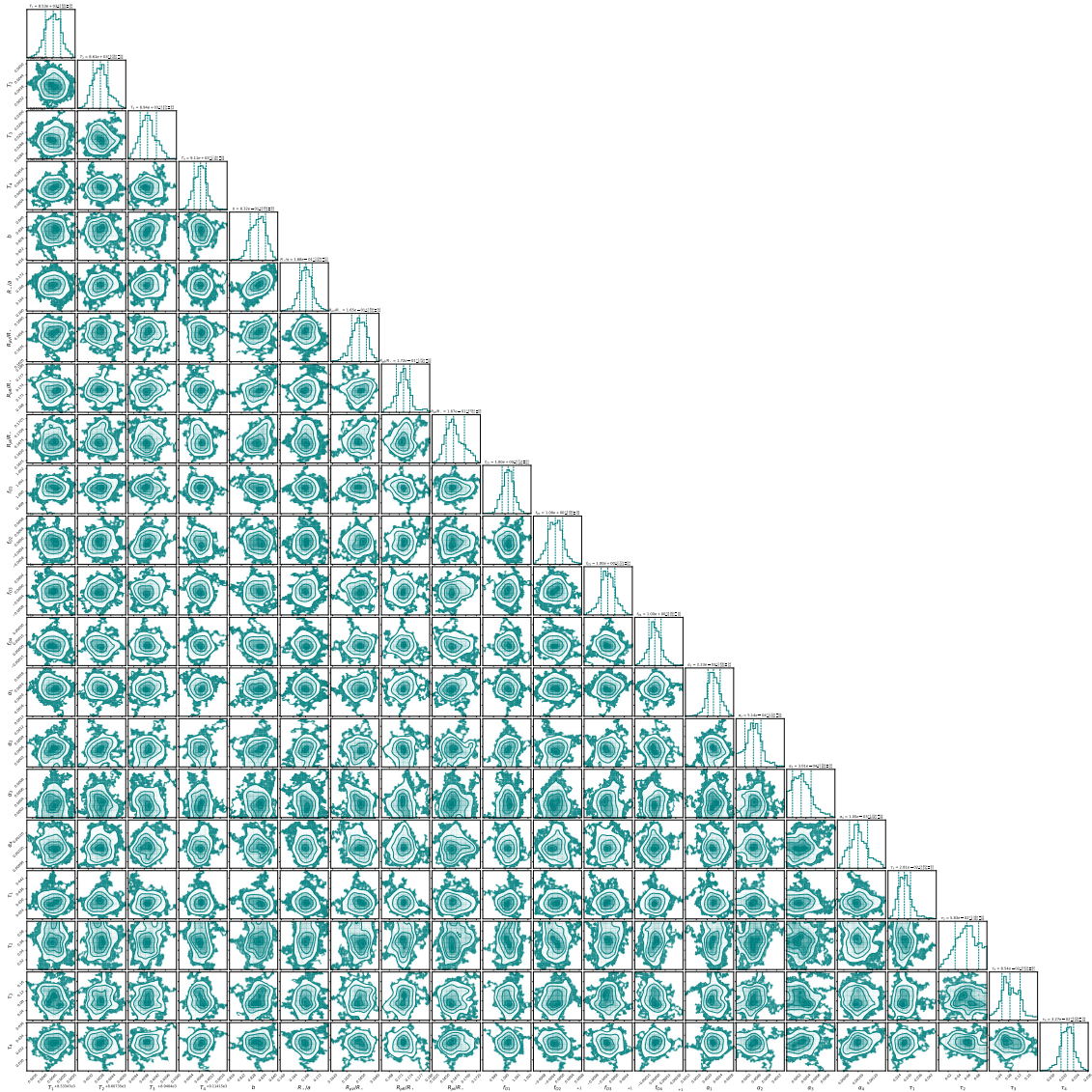


Figure 2.9: Same as Figure 2.6, but for TrES-3 b

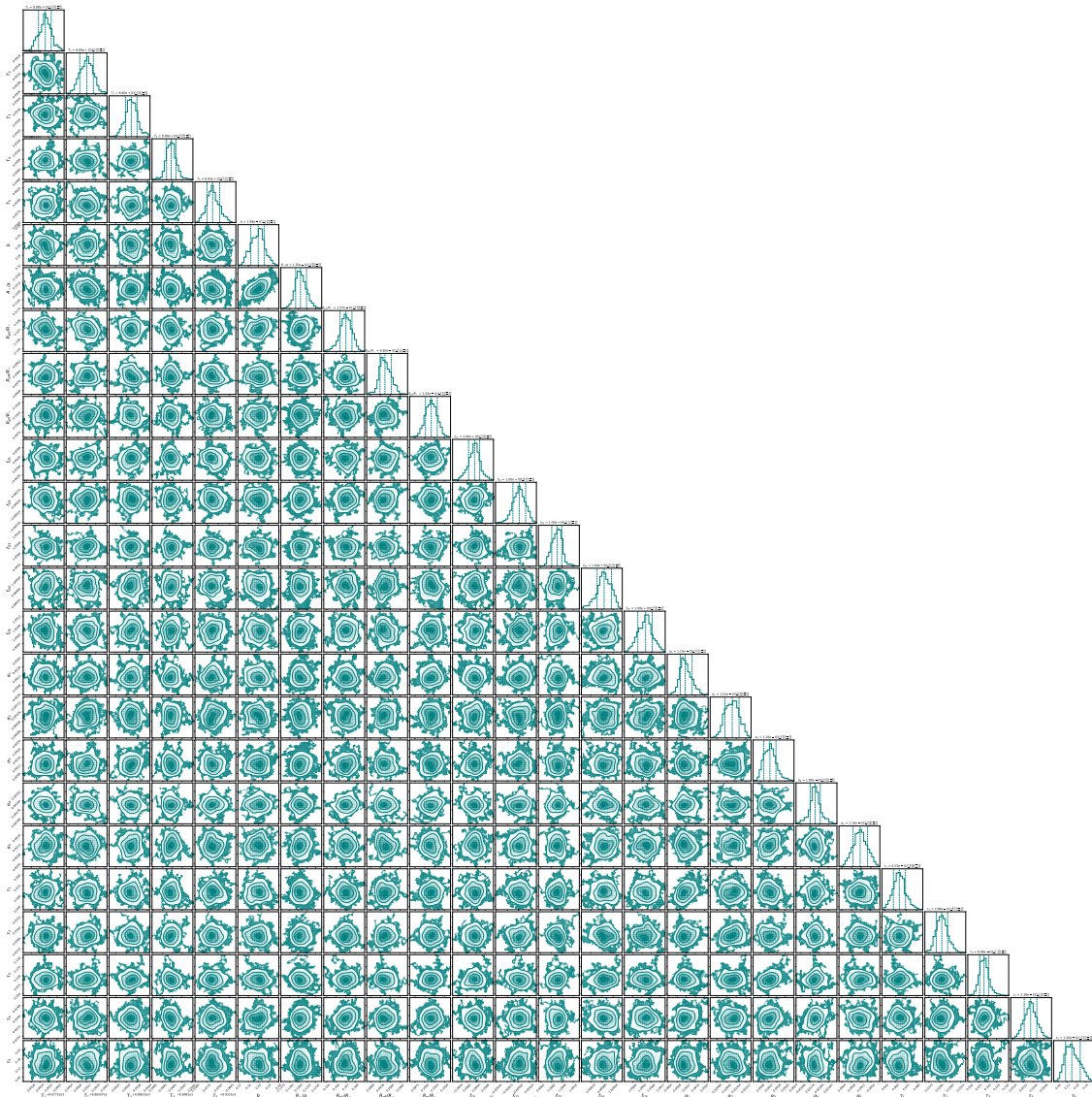


Figure 2.10: Same as Figure 2.6, but for XO-2 N b

Chapter 3

Critical analysis of space-based transit photometric observations from TESS ‡

3.1 Introduction

The transit photometric follow-up studies of known exoplanets are aimed at improving their physical properties through repeated observations using better facilities and by using improved noise reduction and analysis techniques (Chakrabarty & Sengupta, 2019; Christiansen et al., 2011; Esposito et al., 2017; Livingston et al., 2019; Saha et al., 2021). The results from the follow-up studies over a prolonged period of time can also be used to study the planetary dynamics and the presence of other undiscovered planetary mass objects in those systems (Gillon et al., 2017; M. C. Johnson et al., 2015; Maciejewski et al., 2018; Nesvorný et al., 2012; Patra et al., 2017). The improved values of various planetary parameters obtained through follow-up observations and precise noise reduction and data analysis would help interpreting the observed transmission spectra of the exoplanets more accurately through precise modeling (Chakrabarty & Sengupta, 2020; Sengupta et al., 2020).

The transit follow-up observation from the space-based telescopes has an edge as they are unaffected by the variability of Earth's atmosphere. Another advantage of space-based telescopes is their longer available observational time as compared to their ground based counter-parts that remain dormant owing to daylight and unfavorable weather conditions. This longer available observation time is an useful aspect in continuous monitoring and follow-up of successive transit events. The Transiting Exoplanet Survey Satellite (TESS) (Ricker et al., 2015) is a space-based survey mission for the discovery of new exoplanets around bright nearby stars. It is also a powerful tool for transit follow-up studies of already discovered exoplanets,

‡Part of this work is published in Suman Saha and Sujana Sengupta 2021 AJ 162 221, doi:10.3847/1538-3881/ac294d.

because it covers a large portion ($\sim 75\%$) of the sky over the span of the entire survey. Space based instruments as TESS are affected by the scattered light from the Earth and the Moon, which causes increased background sky levels during certain parts of certain sectors. Also, though the observations from TESS is deprived of all noise components that arise by the interference of Earth’s atmosphere, the noise components due to various instrumental effects and the stellar activity and pulsations need to be effectively reduced in order to estimate the physical properties of the target exoplanets with better accuracy and precision.

We have recently reported (Saha et al., 2021) multiband transit follow-up studies of a few exoplanets with the implementation of critical noise reduction techniques that provided improved physical properties. The present study is a continuation of that project. Here we have used the photometric time-series data from TESS to conduct transit follow-up studies of four hot Jupiters: KELT-7 b (e.g., Bieryla et al., 2015), HAT-P-14 b (e.g., Torres et al., 2010), WASP-29 b (e.g., Hellier et al., 2010), WASP-95 b (e.g., Hellier et al., 2014), and a hot Neptune: WASP-156 b (e.g., Demangeon et al., 2018). The instrumental effects of TESS contribute to the small scale fluctuations in the light-curves, which are uncorrelated in time. These fluctuations are similar in effect to the fluctuations in the light-curves from the ground-based telescopes due to the effect of Earth’s atmosphere (Chakrabarty & Sengupta, 2019; Saha et al., 2021), but differ in magnitude scale, which is towards the lower end for TESS. We have used the wavelet denoising technique (Chakrabarty & Sengupta, 2019; Donoho & Johnstone, 1994; Luo & Zhang, 2012; Quan Pan et al., 1999; Saha et al., 2021) to effectively reduce this noise component without compromising the high-frequency components of the transit signals. The stellar activity and pulsations result in small temporal scale correlated noise in the light-curves. These noise components are treated by modeling them simultaneously along with the transit signal using the Gaussian Process (GP) regression method (Barros et al., 2020; Chakrabarty & Sengupta, 2019; M. C. Johnson et al., 2015; Pereira et al., 2019; Rasmussen & Williams, 2006; Saha et al., 2021). The improvements of the estimated physical properties due to the use of these critical noise reduction techniques is also demonstrated (see section 3.4).

Following Chakrabarty and Sengupta (2019) and Saha et al. (2021), we have modeled the transit light-curves by using the analytical transit formalism given by Mandel and Agol (2002). This incorporates the quadratic limb-darkening effect and uses the Markov chain Monte Carlo (MCMC) sampling technique by invoking the Metropolis-Hastings algorithm (Hastings, 1970). From this modeling, we have

Table 3.1: Physical properties of the host stars

	KELT-7	HAT-P-14	WASP-29	WASP-95	WASP-156
$K_{RV} [m s^{-1}]$	138 ± 19	219 ± 3.3	35.6 ± 2.7	175.7 ± 1.7	19 ± 1
$R_{\star} [R_{\odot}]$	1.715 ± 0.049	1.468 ± 0.054	0.808 ± 0.044	1.13 ± 0.08	0.76 ± 0.03
$M_{\star} [M_{\odot}]$	1.483 ± 0.069	1.386 ± 0.045	0.825 ± 0.033	1.11 ± 0.09	0.842 ± 0.052
$T_{eff} [K]$	6789 ± 49	6600 ± 90	4800 ± 150	5830 ± 140	4910 ± 61

Sources: KELT-7 b (Bieryla et al., 2015), HAT-P-14 b (Torres et al., 2010), WASP-29 b (Hellier et al., 2010), WASP-95 b (Hellier et al., 2014), WASP-156 b (Demangeon et al., 2018)

estimated the transit parameters for our target exoplanets and used them to estimate the ephemeris parameters and other derivable parameter. For a streamlined flow of data analysis and modeling, we have used our semi-automated software package, previously used in Saha et al. (2021). We have compared the estimated parameter values obtained from this study with those from the previous studies (see section 3.4) to determine the improvement brought upon by this work.

In section 3.2, we have detailed target selection and observations. In section 3.3, we have described data analysis and modeling procedures. In section 3.4, we have discussed the significance of our results and in section 3.5, we have derived conclusions.

3.2 Target selection and observational data

The TESS survey is aimed at detection of exoplanets around bright stars (9-15 mag), with the upper end limited only to exoplanets with significantly high transit depth. This is because the effective S/N decreases with the increase in magnitude. However, the studies involving precise estimation of physical properties require photometric observations with high S/N ($\gtrsim 100$) and thereby limits the optimal magnitude for such studies ($\lesssim 12$ mag).

For our current study, we have selected five exoplanets, e.g., KELT-7 b, HAT-P-14 b, WASP-29 b, WASP-95 b and WASP-156 b, all of which are orbiting around bright stars with magnitude < 12 , and are within TESS survey field. We have found large uncertainties in their known parameter values with no significant follow-up studies. The properties of the target host stars used in our analysis are listed in Table 3.1. In this table K_{RV} is the radial velocity of the host star, R_{\star} and M_{\star} are its radius and mass respectively in term of solar radius R_{\odot} and solar mass M_{\odot} , and T_{eff} is its

effective temperature. KELT-7 was observed in TESS sector 19, HAT-P-14 in 25 and 26, WASP-29 in 2 and 29, WASP-95 in 1 and 28, and WASP-156 in 4 and 31. We have obtained the TESS PDCSAP light-curves (Jenkins, 2017; Smith et al., 2012; Stumpe et al., 2012, 2014) of these target stars from the public Mikulski Archive for Space Telescopes (MAST)*. From these light-curves, we have identified 9, 11, 11, 20 and 12 full transit observations for KELT-7 b, HAT-P-14 b, WASP-29 b, WASP-95 b and WASP-156 b respectively.

3.3 Data analysis and modeling

In this section, we describe the two most important aspects of this study, i.e. the noise treatment and the modeling of the transit light-curves. For this part of the study, we have used our semi-automated software package, written in Python and used in our previous investigations (Chakrabarty & Sengupta, 2019; Saha et al., 2021).

At first, we have sliced the long continuous TESS light-curves into smaller segments concentrated around the observed full-transit events to obtain the transit light-curves. We have used only full-transit observations in this study to account for the best possible accuracy. To eliminate any long-term variability effects in these light-curves, we have treated them with the baseline correction method following the same procedure as in Saha et al. (2021).

To reduce the small-scale time-uncorrelated fluctuations in the light-curves due to various instrumental effects, we have used the wavelet denoising technique (Chakrabarty & Sengupta, 2019; Donoho & Johnstone, 1994; Luo & Zhang, 2012; Quan Pan et al., 1999; Saha et al., 2021). For this purpose, we have used the PyWavelets (Lee et al., 2019) python package for the wavelet based operations and followed the procedure described in Saha et al. (2021). We have shown the transit light-curves before and after wavelet denoising in Figures 3.1-3.6.

We have reduced the correlated noise components in the light-curves due to stellar activities and pulsations by modeling them simultaneously along with the transit signals using the GP regression method (Barros et al., 2020; Chakrabarty & Sengupta, 2019; M. C. Johnson et al., 2015; Pereira et al., 2019; Rasmussen & Williams, 2006; Saha et al., 2021). Following Saha et al. (2021), we have used the formalism described in Rasmussen and Williams (2006) for noisy observations. We have shown the best-fit GP regression models over-plotted on the correlated noise components and the

*<https://mast.stsci.edu/portal/Mashup/Clients/Mast/Portal.html>

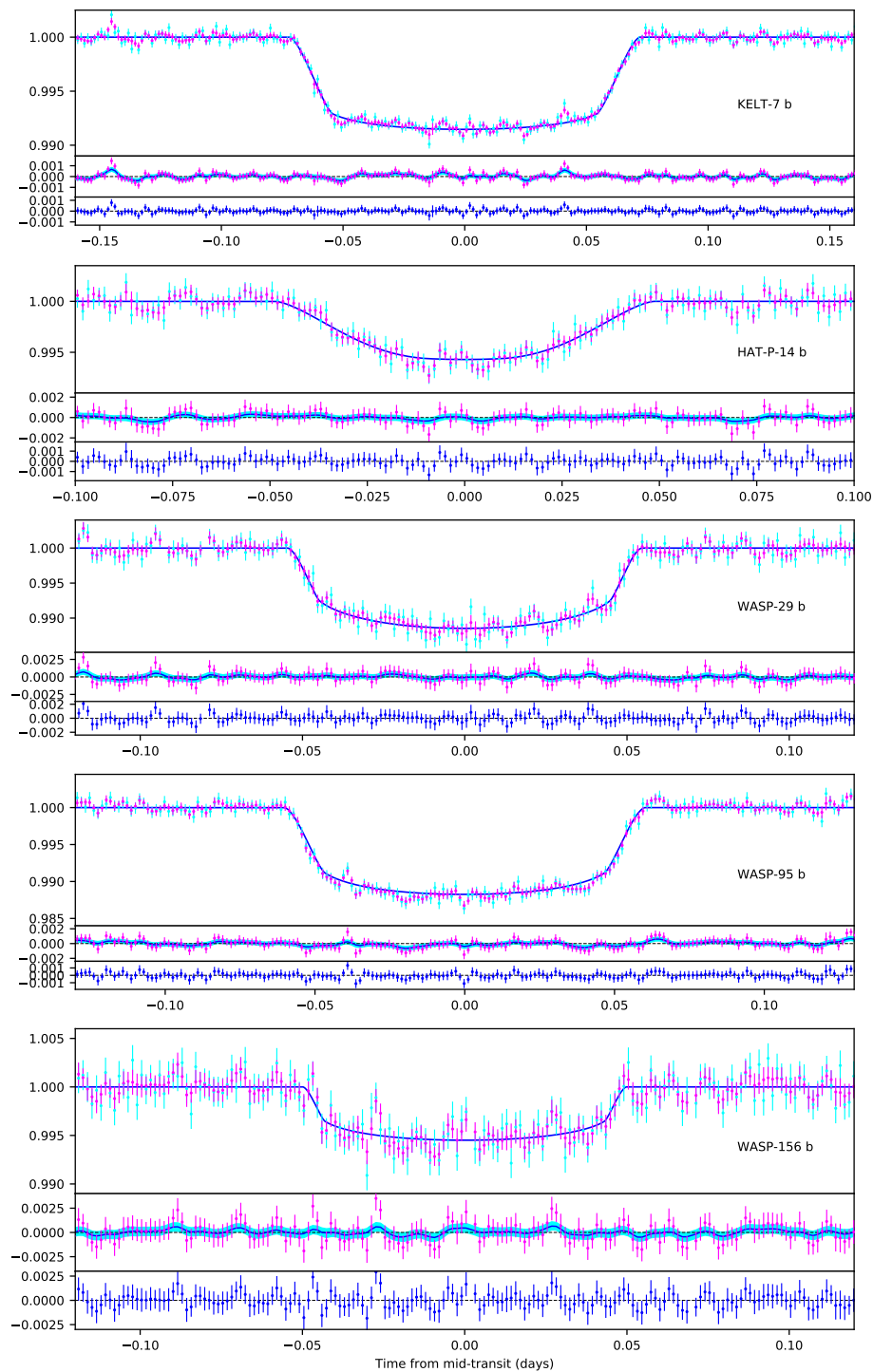


Figure 3.1: Observed and best-fit model light-curves of one transit event for each of our target exoplanets. For each observed transit, Top: the unprocessed light-curve (cyan), light-curve after wavelet denoising (magenta), the best-fit transit model (blue). Middle: the residual after modeling without GP regression (magenta), the mean (blue) and 1- σ interval (cyan) of the best-fit GP regression model. Bottom: mean residual flux (blue). All lightcurves used in this study are shown in Figures 3.2-3.6

reduced mean residuals following the GP regression in Figures 3.1-3.6.

To model the transit signals, we have followed the analytical transit model formulation given by Mandel and Agol (2002). This formulation incorporates the limb-darkening effects of the host stars by using a quadratic limb-darkening formula. In order to estimate the transit parameters for our target exoplanets, we have used the MCMC sampling technique by incorporating the Metropolis-Hastings algorithm (Hastings, 1970) for the simultaneous modeling of the transit light-curves. A detailed description of this technique can be found in Saha et al. (2021). We have shown the best-fit transit models over-plotted on the observed and wavelet denoised light-curves in the Figures 3.1-3.6. To understand the improvements in the values of various physical parameters estimated by using our critical noise reduction techniques, i.e. wavelet denoising and GP regression, we have also modeled the transit light-curves of our target exoplanets directly without using these techniques.

One of the estimated parameters from the modeling of our transit light-curves is the mid-transit times T_C . These values of T_C are used to model the linear ephemeris of these exoplanets with two free parameters, T_0 and P , using the MCMC sampling technique. Following the relations given in Saha et al. (2021), we have derived the values of the remaining physical parameters from the estimated parameter values and the adopted host star properties as listed in Table 3.1. We have tabulated all the derived physical parameters of our target exoplanets in Tables 3.2-3.6. We have also listed the best-fit GP regression model parameters in Table 3.7, while the estimated mid-transit times with O-C deviations from the best-fit linear ephemeris are provided in Table 3.8.

Table 3.2: Estimated physical parameters for KELT-7 b

Parameter	This work	Exp values †	Bieryla et al. (2015)
Transit parameters			
T_0 [BJD_{TDB}]	$2458816.518385 \pm 0.000051$	$2458816.518344 \pm 0.000083$	$2456352.495016 \pm 0.000191$
P [$days$]	2.734784 ± 0.000009	2.734788 ± 0.000015	2.7347795 ± 0.00000037
b	$0.59178^{+0.00036}_{-0.00039}$	$0.59185^{+0.00072}_{-0.00082}$	$0.599^{+0.023}_{-0.026}$
R_*/a	$0.178949^{+0.000022}_{-0.000020}$	$0.178968^{+0.000078}_{-0.000093}$	0.1828 ± 0.0040
R_p/R_*	$0.089597^{+0.000021}_{-0.000019}$	$0.089623^{+0.000071}_{-0.000057}$	$0.09074^{+0.00067}_{-0.00066}$
Limb-darkening coefficients			
C_1	$0.2106^{+0.0035}_{-0.0049}$	$0.2078^{+0.0068}_{-0.0075}$	—
C_2	$0.2192^{+0.0059}_{-0.0055}$	$0.218^{+0.010}_{-0.011}$	—
Derived parameters			
T_{14} [hr]	$3.4555^{+0.0012}_{-0.0010}$	$3.4557^{+0.0025}_{-0.0023}$	$3.511^{+0.023}_{-0.022}$
a/R_*	$5.58818^{+0.00061}_{-0.00069}$	$5.5876^{+0.0029}_{-0.0024}$	5.47 ± 0.12
i [deg]	$83.9211^{+0.0039}_{-0.0038}$	$83.9203^{+0.0084}_{-0.0096}$	$83.72^{+0.40}_{-0.39}$
M_p [M_J]	$1.24^{+0.18}_{-0.17}$	$1.24^{+0.18}_{-0.17}$	1.28 ± 0.18
M_p [M_\oplus]	$394.2^{+55.7}_{-55.1}$	$394.2^{+55.7}_{-55.1}$	407 ± 57
T_{eq} [K]	2030.8 ± 14.6	2030.8 ± 14.6	2051^{+28}_{-27}
a [AU]	0.0446 ± 0.0013	0.0446 ± 0.0013	$0.04364^{+0.00067}_{-0.00068}$
R_p [R_J]	1.293 ± 0.060	1.293 ± 0.060	$1.514^{+0.051}_{-0.050}$
R_p [R_\oplus]	14.49 ± 0.67	14.49 ± 0.67	$16.97^{+0.57}_{-0.56}$

† values estimated without using wavelet denoising and GP regression techniques (for comparison purpose).

Table 3.3: Estimated physical parameters for HAT-P-14 b

Parameter	This work	Exp values †	Torres et al. (2010)
Transit parameters			
T_0 [BJD_{TDB}]	$2458984.653413 \pm 0.000047$	$2458984.653370 \pm 0.000093$	$2454875.28938 \pm 0.00047$
P [$days$]	4.627686 ± 0.0000077	4.627694 ± 0.000015	4.627669 ± 0.000005
b	$0.91039^{+0.00017}_{-0.00019}$	$0.91044^{+0.00034}_{-0.00033}$	$0.891^{+0.007}_{-0.008}$
R_*/a	$0.112595^{+0.000039}_{-0.000046}$	$0.112590^{+0.000066}_{-0.000061}$	0.1127 ± 0.0037
R_p/R_*	$0.081607^{+0.000020}_{-0.000024}$	$0.081609^{+0.000067}_{-0.000063}$	0.0805 ± 0.0015
Limb-darkening coefficients			
C_1	$0.2486^{+0.0080}_{-0.0072}$	$0.150^{+0.012}_{-0.011}$	0.1089
C_2	$0.2805^{+0.0084}_{-0.0079}$	$0.281^{+0.013}_{-0.015}$	0.2439
Derived parameters			
T_{14} [hr]	$2.3386^{+0.0014}_{-0.0013}$	2.3384 ± 0.0021	2.1888 ± 0.0408
a/R_*	$8.8881^{+0.0036}_{-0.0031}$	$8.8818^{+0.0048}_{-0.0052}$	8.87 ± 0.29
i [deg]	$84.1167^{+0.0026}_{-0.0025}$	$84.1164^{+0.0050}_{-0.0046}$	83.5 ± 0.3
M_p [M_J]	2.244 ± 0.059	2.244 ± 0.059	2.232 ± 0.059
M_p [M_\oplus]	$713.1^{+18.8}_{-18.7}$	$713.1^{+18.9}_{-18.6}$	709.4 ± 18.7
T_{eq} [K]	1566.0 ± 21.2	1566.0 ± 21.2	1570 ± 34
a [AU]	0.0606 ± 0.0022	0.0606 ± 0.0022	0.0606 ± 0.0007
R_p [R_J]	1.101 ± 0.036	1.101 ± 0.036	1.150 ± 0.052
R_p [R_\oplus]	12.34 ± 0.40	12.34 ± 0.40	12.89 ± 0.58

† values estimated without using wavelet denoising and GP regression techniques (for comparison purpose).

Table 3.4: Estimated physical parameters for WASP-29 b

Parameter	This work	Exp values †	Hellier et al. (2010)
Transit parameters			
T_0 [BJD_{TDB}]	$2458356.414870 \pm 0.000032$	$2458356.414808 \pm 0.000066$	2455320.2341 ± 0.004
P [$days$]	$3.92271218 \pm 0.00000025$	$3.92271254 \pm 0.00000053$	3.922727 ± 0.000004
b	$0.1160^{+0.0036}_{-0.0039}$	$0.1169^{+0.0078}_{-0.0077}$	0.29 ± 0.15
R_*/a	$0.080005^{+0.00044}_{-0.000040}$	$0.080008^{+0.000074}_{-0.000061}$	—
R_p/R_*	$0.096602^{+0.000039}_{-0.000049}$	$0.096595^{+0.000056}_{-0.000069}$	0.1010 ± 0.0020
Limb-darkening coefficients			
C_1	$0.5001^{+0.0046}_{-0.0032}$	$0.4995^{+0.0069}_{-0.0077}$	—
C_2	$0.1396^{+0.0038}_{-0.0037}$	$0.1406^{+0.0087}_{-0.0076}$	—
Derived parameters			
T_{14} [hr]	$2.6178^{+0.0016}_{-0.0014}$	$3.0881^{+0.0039}_{-0.0034}$	2.6592 ± 0.036
a/R_*	$12.4992^{+0.0063}_{-0.0069}$	$12.499^{+0.010}_{-0.012}$	—
i [deg]	$89.468 - 0.017^{+0.018}$	$89.464^{+0.035}_{-0.036}$	88.8 ± 0.7
M_p [M_J]	$0.243^{+0.020}_{-0.019}$	0.257 ± 0.020	0.244 ± 0.020
M_p [M_\oplus]	$77.2^{+6.2}_{-6.1}$	$81.5^{+6.6}_{-6.5}$	77.547 ± 6.356
T_{eq} [K]	$960.0^{+29.9}_{-29.8}$	$960.1^{+29.8}_{-29.9}$	—
a [AU]	0.0470 ± 0.0025	0.0470 ± 0.0025	0.0457 ± 0.0006
R_p [R_J]	0.775 ± 0.031	0.775 ± 0.031	$0.792^{+0.056}_{-0.035}$
R_p [R_\oplus]	8.69 ± 0.35	8.69 ± 0.35	$8.878^{+0.628}_{-0.392}$

† values estimated without using wavelet denoising and GP regression techniques (for comparison purpose).

Table 3.5: Estimated physical parameters for WASP-95 b

Parameter	This work	Exp values †	Hellier et al. (2014)
Transit parameters			
T_0 [BJD_{TDB}]	$2458326.505909 \pm 0.000027$	$2458326.505892 \pm 0.000048$	$2456338.45851 \pm 0.00024$
P [$days$]	2.1846656 ± 0.00000011	$2.18466574 \pm 0.00000019$	2.1846730 ± 0.0000014
b	$0.41984^{+0.00071}_{-0.00097}$	$0.4197^{+0.0012}_{-0.0013}$	$0.19^{+0.21}_{-0.13}$
R_*/a	$0.168589^{+0.000039}_{-0.000045}$	$0.168601^{+0.000083}_{-0.000073}$	—
R_p/R_*	$0.101692^{+0.000048}_{-0.000044}$	$0.101694^{+0.000069}_{-0.000074}$	0.1025 ± 0.0015
Limb-darkening coefficients			
C_1	$0.3345^{+0.0032}_{-0.0042}$	0.3332 ± 0.0059	—
C_2	$0.2306^{+0.0037}_{-0.0040}$	$0.2294^{+0.0067}_{-0.0079}$	—
Derived parameters			
T_{14} [hr]	$2.8877^{+0.0017}_{-0.0015}$	$2.8877^{+0.0012}_{-0.0015}$	2.784 ± 0.024
a/R_*	$5.9316^{+0.0016}_{-0.0014}$	$5.9316^{+0.0016}_{-0.0014}$	—
i [deg]	$85.9411^{+0.0065}_{-0.0066}$	$85.9411^{+0.0095}_{-0.0066}$	$88.4^{+1.2}_{-2.1}$
M_p [M_J]	$1.206^{+0.065}_{-0.067}$	$1.206^{+0.065}_{-0.067}$	$1.13^{+0.1}_{-0.04}$
M_p [M_\oplus]	$383.1^{+20.7}_{-21.2}$	$383.1^{+20.7}_{-21.2}$	$359.13^{+31.78}_{-12.71}$
T_{eq} [K]	1692.6 ± 40.4	1692.6 ± 40.4	1570 ± 50
a [AU]	0.0312 ± 0.0022	0.0312 ± 0.0022	0.03416 ± 0.00083
R_p [R_J]	1.098 ± 0.088	1.098 ± 0.088	1.21 ± 0.06
R_p [R_\oplus]	12.31 ± 0.99	12.31 ± 0.99	13.56 ± 0.67

† values estimated without using wavelet denoising and GP regression techniques (for comparison purpose).

Table 3.6: Estimated physical parameters for WASP-156 b

Parameter	This work	Exp values †	Demangeon et al. (2018)
Transit parameters			
T_0 [BJD_{TDB}]	$2458414.136153 \pm 0.000065$	$2458414.13622 \pm 0.00012$	2454677.707 ± 0.002
P [$days$]	3.8361603 ± 0.00000048	$3.83615987 \pm 0.00000089$	3.836169 ± 0.0000003
b	$0.2442^{+0.0061}_{-0.0073}$	$0.240^{+0.016}_{-0.010}$	—
R_*/a	$0.07844^{+0.00016}_{-0.00015}$	$0.07843^{+0.00024}_{-0.00026}$	$0.0781^{+0.0018}_{-0.0043}$
R_p/R_*	$0.067654^{+0.000082}_{-0.000060}$	$0.06766^{+0.00015}_{-0.00017}$	$0.0685^{+0.0012}_{-0.0008}$
Limb-darkening coefficients			
C_1	$0.4717^{+0.0040}_{-0.0043}$	$0.4728^{+0.0077}_{-0.0061}$	0.461 ± 0.002
C_2	$0.1344^{+0.0070}_{-0.0106}$	$0.135^{+0.015}_{-0.016}$	$0.0995^{+0.0066}_{-0.0074}$
Derived parameters			
T_{14} [hr]	$2.3926^{+0.0049}_{-0.0055}$	$2.3930^{+0.0089}_{-0.0098}$	$2.41^{+0.04}_{-0.03}$
a/R_*	$12.748^{+0.025}_{-0.027}$	$12.750^{+0.043}_{-0.039}$	$12.8^{+0.3}_{-0.7}$
i [deg]	$88.902^{+0.033}_{-0.028}$	$88.921^{+0.049}_{-0.072}$	$89.1^{+0.6}_{-0.9}$
M_p [M_J]	$0.1303^{+0.0088}_{-0.0086}$	$0.1303^{+}_{-0.0085}0.0088$	$0.128^{+0.010}_{-0.009}$
M_p [M_\oplus]	$41.4^{+2.8}_{-2.7}$	$41.4^{+2.8}_{-2.7}$	$40.7^{+3.2}_{-2.9}$
T_{eq} [K]	972.4 ± 17.3	972.4 ± 17.4	970^{+30}_{-20}
a [AU]	0.0451 ± 0.0018	0.0451 ± 0.0018	0.0453 ± 0.0009
R_p [R_J]	0.554 ± 0.034	0.554 ± 0.034	0.51 ± 0.02
R_p [R_\oplus]	6.22 ± 0.38	6.22 ± 0.38	5.7 ± 0.2

† values estimated without using wavelet denoising and GP regression techniques (for comparison purpose).

Table 3.7: Best-fit GP regression model parameters

Target	α	τ
KELT-7 b	$0.0002496^{+0.0000014}_{-0.0000015}$	$0.002805^{+0.000012}_{-0.000016}$
HAT-P-14 b	$0.0003001^{+0.0000016}_{-0.0000014}$	$0.003201^{+0.000020}_{-0.000015}$
WASP-29 b	$0.0004297^{+0.0000015}_{-0.0000017}$	$0.002700^{+0.000016}_{-0.000013}$
WASP-95 b	$0.0003393^{+0.0000021}_{-0.0000020}$	$0.002998^{+0.000056}_{-0.000050}$
WASP-156 b	$0.0005149^{+0.0000127}_{-0.0000166}$	$0.002806^{+0.000077}_{-0.000086}$

3.4 Discussion

In this study, we have conducted transit photometric follow-up analysis of four hot Jupiters, KELT-7 b, HAT-P-14 b, WASP-29 b, WASP-95 b, and a hot Neptune, WASP-156 b, using the photometric observations from the TESS space-based telescope, and using the critical noise reduction techniques, i.e. wavelet denoising and GP regression. The main purpose have been to estimate the various physical properties of these exoplanets more precisely and accurately.

Starting with the photometric observations from TESS, having a constant cadence of 120 seconds of exposure time means a gradual decrease in S/N with the increase in magnitude (Bryson et al., 2010). The visible difference in S/N is well noticeable in the KELT-7, which is the brightest among all our target stars and the WASP-156, the faintest one. However, in the present work, the absence of any fluctuations in the light-curves from the atmospheric effects has given us an advantage over the previous studies of our target exoplanets, all of which were based on observations using ground-based facilities.

The small scale fluctuations in the light-curves caused by various instrumental effects that are uncorrelated in time, are especially noticeable because of the absence atmospheric effects. We have reduced them using the same wavelet denoising technique which has been found to be efficient in our previous studies of transiting exoplanets observed by using ground-based facilities. The time-correlated noise components due to stellar activities and pulsations were also reduced by applying GP regression method. It is worth mentioning here that the amplitude of these correlated noise components in TESS observations is small compared to those from ground-based observations. This is because of the fact that unlike their ground-based counterparts, the space-based observations do not require differential photometric method in order to tackle the effects of air-mass and atmospheric variability. This is

Table 3.8: Estimated mid-transit times

Target	Epoch	T_C [BJD _{TDB}]	O – C [sec]
KELT-7 b	0	2458816.517884 ^{+0.000129} _{-0.000102}	-43.23
	1	2458819.253384 ^{+0.000083} _{-0.000068}	18.61
	2	2458821.987897 ^{+0.000085} _{-0.000073}	-4.78
	3	2458824.723077 ^{+0.000059} _{-0.000083}	29.39
	4	2458827.457495 ^{+0.000087} _{-0.000081}	-2.24
	5	2458830.192210 ^{+0.000059} _{-0.000071}	-8.20
	6	2458832.926792 ^{+0.000081} _{-0.000073}	-25.68
	7	2458835.661988 ^{+0.000091} _{-0.000080}	9.94
	8	2458838.396687 ^{+0.000071} _{-0.000057}	2.57
HAT-P-14 b	0	2458984.653102 ^{+0.000094} _{-0.000093}	-26.92
	1	2458989.281403 ^{+0.000078} _{-0.000071}	26.23
	2	2458993.908200 ^{+0.000072} _{-0.000086}	-50.61
	3	2458998.535608 ^{+0.000078} _{-0.000090}	-74.64
	4	2459003.165288 ^{+0.000085} _{-0.000081}	97.57
	5	2459007.792394 ^{+0.000056} _{-0.000065}	47.44
	6	2459012.419598 ^{+0.000082} _{-0.000067}	5.80
	7	2459017.046880 ^{+0.000075} _{-0.000064}	-29.13
	8	2459021.675296 ^{+0.000080} _{-0.000061}	33.94
	9	2459026.301697 ^{+0.000076} _{-0.000061}	-77.07
	10	2459030.930598 ^{+0.000073} _{-0.000083}	27.82
WASP-29 b	0	2458356.415209 ^{+0.000069} _{-0.000057}	29.26
	1	2458360.337309 ^{+0.000058} _{-0.000057}	-23.58
	2	2458364.260001 ^{+0.000073} _{-0.000081}	-25.37
	4	2458372.105822 ^{+0.000073} _{-0.000107}	8.96
	5	2458376.028072 ^{+0.000092} _{-0.000075}	-31.00
	6	2458379.951496 ^{+0.000056} _{-0.000071}	30.50
	187	2459089.962194 ^{+0.000065} _{-0.000092}	12.68
	188	2459093.884380 ^{+0.000077} _{-0.000074}	-32.74
	189	2459097.807400 ^{+0.000064} _{-0.000071}	6.21
	191	2459105.653298 ^{+0.000079} _{-0.000080}	34.71
	192	2459109.575601 ^{+0.000091} _{-0.000083}	-0.57

Table 3.8: Estimated mid-transit times (*cont.*)

Target	Epoch	T_C [BJD _{TDB}]	O – C [sec]
WASP-95 b	0	2458326.506113 ^{+0.000085} _{-0.000069}	17.64
	1	2458328.690901 ^{+0.000082} _{-0.000086}	28.26
	2	2458330.874826 ^{+0.000075} _{-0.000100}	-35.69
	3	2458333.060402 ^{+0.000080} _{-0.000091}	42.88
	5	2458337.428737 ^{+0.000078} _{-0.000082}	-43.18
	7	2458341.798552 ^{+0.000122} _{-0.000085}	-1.37
	8	2458343.983001 ^{+0.000110} _{-0.000105}	-20.09
	9	2458346.167908 ^{+0.000067} _{-0.000082}	70.29
	11	2458350.537197 ^{+0.000065} _{-0.000059}	-2.91
	12	2458352.721972 ^{+0.000081} _{-0.000069}	6.53
	337	2459062.738413 ^{+0.000064} _{-0.000060}	15.67
	338	2459064.922486 ^{+0.000069} _{-0.000069}	-35.58
	339	2459067.107641 ^{+0.000081} _{-0.000114}	6.70
	340	2459069.292621 ^{+0.000066} _{-0.000063}	33.86
	341	2459071.476797 ^{+0.000070} _{-0.000065}	-8.41
	343	2459075.846513 ^{+0.000081} _{-0.000076}	24.81
	344	2459078.031202 ^{+0.000069} _{-0.000087}	26.88
	345	2459080.215201 ^{+0.000069} _{-0.000062}	-30.73
	346	2459082.400225 ^{+0.000071} _{-0.000094}	25.42
	347	2459084.584804 ^{+0.000076} _{-0.000064}	-7.3
WASP-156 b	0	2458414.135676 ^{+0.000134} _{-0.000127}	-41.22
	1	2458417.971972 ^{+0.000172} _{-0.000197}	-29.49
	2	2458421.809599 ^{+0.000144} _{-0.000179}	97.25
	3	2458425.644830 ^{+0.000139} _{-0.000155}	16.94
	4	2458429.480008 ^{+0.000160} _{-0.000138}	-67.93
	5	2458433.317222 ^{+0.000154} _{-0.000128}	23.10
	191	2459146.842429 ^{+0.000122} _{-0.000127}	-29.18
	192	2459150.678210 ^{+0.000180} _{-0.000193}	-61.88
	193	2459154.514789 ^{+0.000164} _{-0.000169}	-25.70
	195	2459162.188300 ^{+0.000153} _{-0.000172}	77.08
	196	2459166.022691 ^{+0.000176} _{-0.000146}	-75.71
	197	2459169.860999 ^{+0.000152} _{-0.000156}	109.79

Table 3.9: Estimated CDPP for lightcurves

Target	CDPP [in ppm]		
	PDCSAP lightcurves	After wavelet denoising	After GP regression
KELT-7 b	138.0	134.5	40.3
HAT-P-14 b	227.0	222.7	117.2
WASP-29 b	243.4	231.1	131.1
WASP-95 b	245.4	241.7	97.8
WASP-156 b	328.2	319.5	189.7

also the reason why we have used a single set of GP regression parameters for each of our targets.

We have estimated the photometric precision of the lightcurves at each step of our critical noise treatment algorithm, by computing the Combined Differential Photometric Precision (CDPP) noise metric (Gilliland et al., 2011; Van Cleve et al., 2016) using the *estimate_cdpp* module of *Lightkurve* (Lightkurve Collaboration et al., 2018) package, and listed in the Table 3.9. We can see a small improvement in the photometric precision due to the wavelet denoising technique and a significant improvement due to the GP regression technique. The small improvement due to wavelet denoising is desirable, as a large correction at this step will lead to an over-smoothing of the lightcurves, resulting in deformation of the transit signals. On the other hand, the GP regression is performed simultaneously along with modeling for the transit signals, and thus a large correction has no impact in deforming the lightcurves.

To appreciate the improvements brought upon by the critical noise reduction techniques, we have also modeled the raw light-curves of our targets without using any of those techniques. We have then compared the estimated values of various physical parameters with those derived after using the critical noise reduction techniques (see Table 3.2). We can clearly notice the improvements in the uncertainty limits in the estimated and directly derived transit parameters achieved by using the critical noise reduction techniques. This proves that the noise components can severely affect the precision and overall accuracy of the estimated parameters when left untreated, and therefore require critical noise reduction methods to reduce them efficiently. However, there is no difference in the uncertainty limits of the estimated values for the parameters that require the adopted properties of the host stars. This is because of the large uncertainties in those stellar parameters.

To understand the improvements in the values of the physical parameters of the target exoplanets derived by us in the present work, we have also compared them with their estimated values from previous studies. We have found a few order of magnitude improvements in the values of the estimated transit parameters and parameters derived from them directly. This is expected and can be attributed to a combination of very high S/N photometric observations from TESS and the state-of-the-art critical noise treatment algorithm used in our study. Only the uncertainty limits in the estimated values for the orbital periods of KELT-7 b and HAT-P-14 b are comparatively large. This is because of the fact that the follow-up observations of these two planets are over a very limited number of transit epochs (9 and 11 respectively). This can be improved by further follow-up studies and combining the results with the precise values for mid-transit times estimated in this study (see Table 3.8). On the other hand, the estimated values of the parameters derived from the stellar parameters, do not have significant improvements over uncertainty limits because of very high uncertainties in the values of the adopted stellar properties.

Overall, our work has resulted into a more precise and accurate estimation of the physical parameters for our target exoplanets as compared to that reported in previous studies. This improvements are attributed to a better quality of photometric data from TESS and reduction of various noise components using a critical noise treatment algorithm.

3.5 Conclusion

In this work, we have critically analyzed TESS transit photometric data of five already discovered exoplanets, e.g., KELT-7 b, HAT-P-14 b, WASP-29 b, WASP-95 b and WASP-156 b. Being a space based telescope, the TESS observations are unaffected by Earth's atmospheric interferences. Also, since all the target host stars in our study were brighter than 12 magnitude, we have found high S/N in all the transit light-curves.

In order to improve the quality of the transit signal in the light-curves, we have reduced the noise components due to various sources by using a state-of-the-art critical noise treatment algorithm that includes wavelet denoising and GP regression methods. Thus, we have demonstrated the efficiency of these techniques in improving the precision and overall accuracy of the estimated parameters.

The modeling of the transit light-curves has used the MCMC sampling technique, which has provided extremely precise estimation of the physical parameters for our

target exoplanets. This can be attributed to both the quality of the photometric observations from TESS and the critical noise treatment algorithm used in this study. We have compared our estimated parameter values with those from the previous studies to show the improvements in precision and overall accuracy. The work establishes the power of space-based photometric follow-up studies when combined with a critical noise treatment approach.

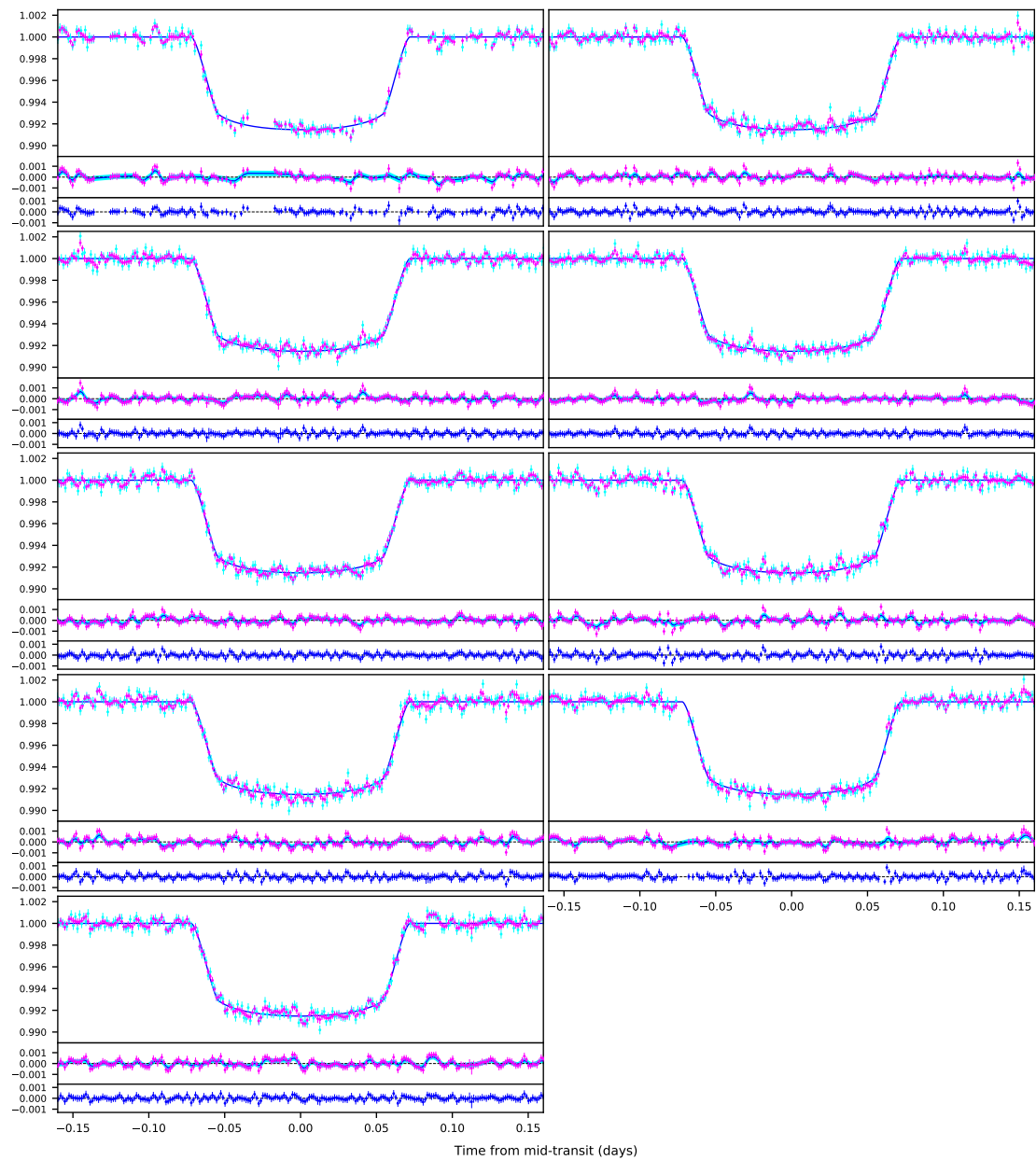


Figure 3.2: All observed and best-fit model light-curves for KELT-7 b, with descriptions same as Figure 3.1

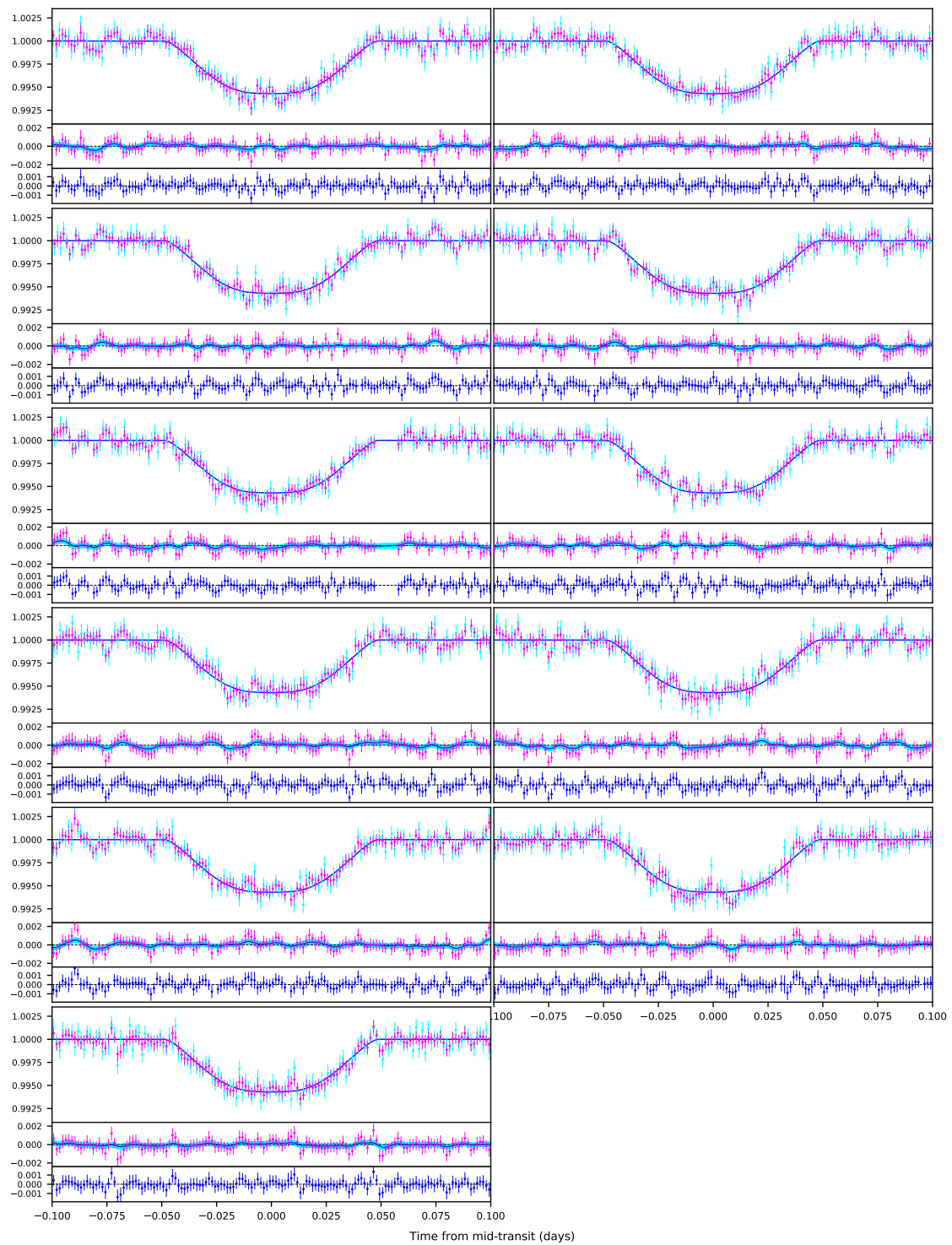


Figure 3.3: Same as Figure 3.2, but for HAT-P-14 b

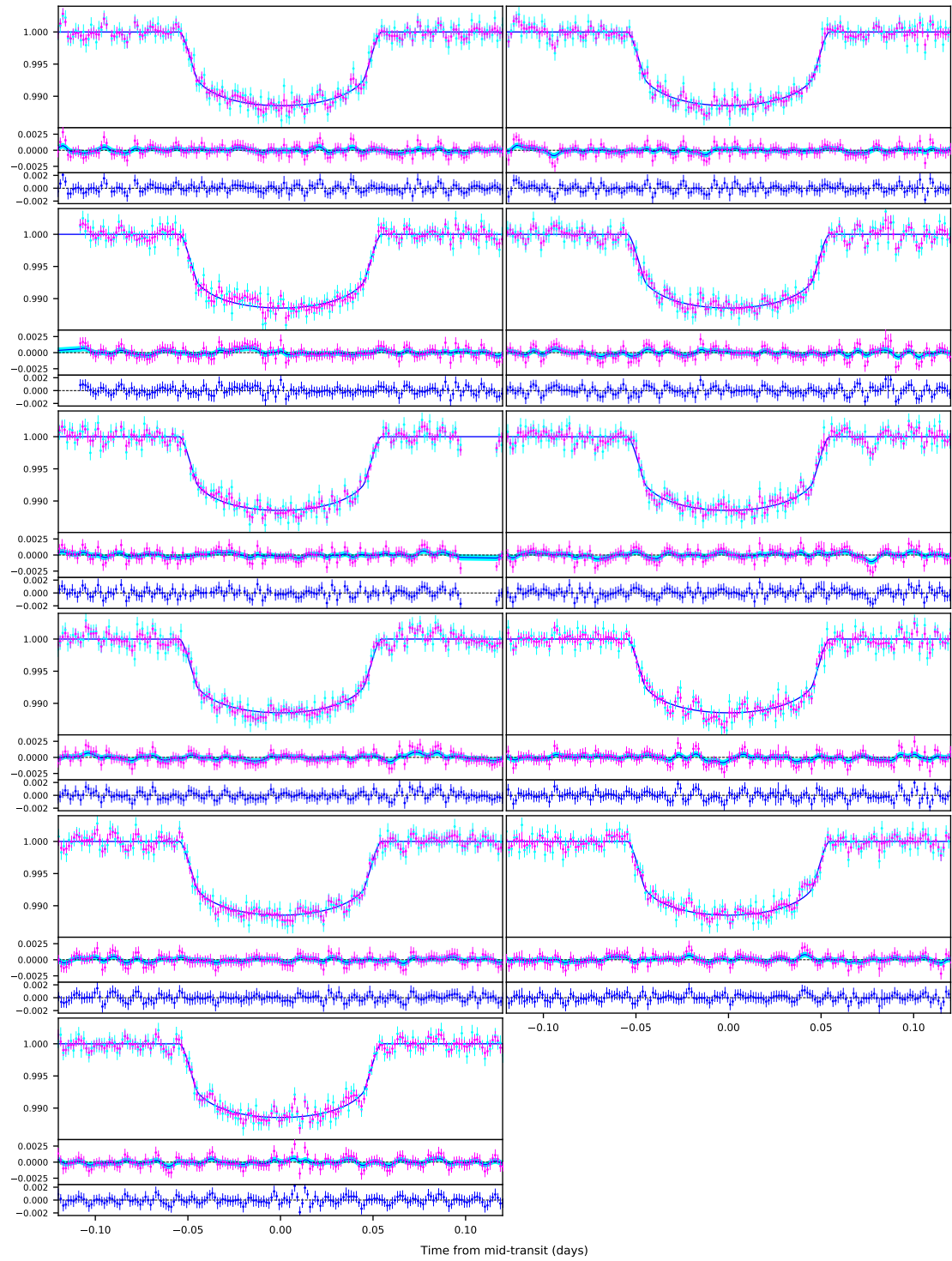


Figure 3.4: Same as Figure 3.2, but for WASP-29 b

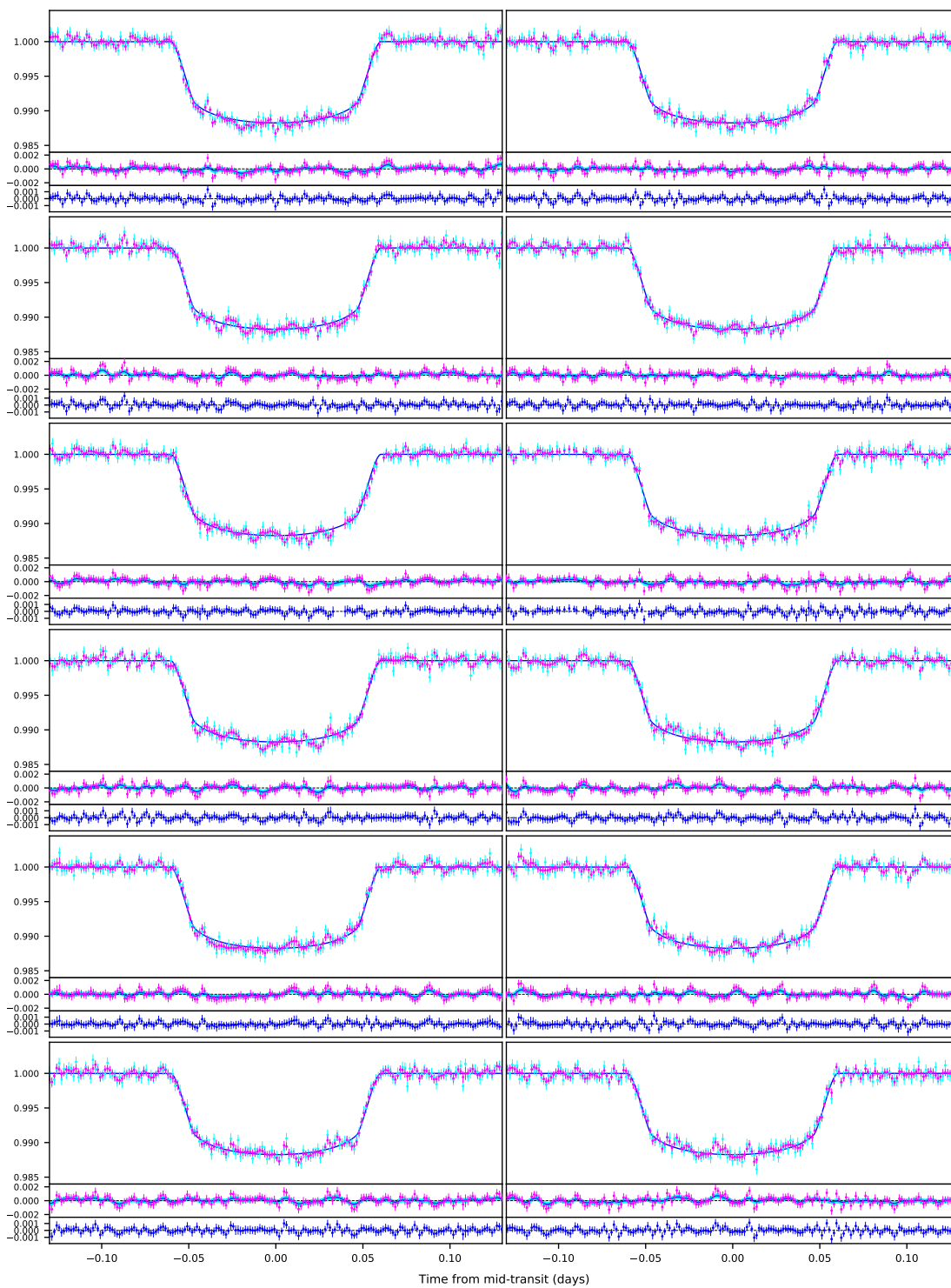


Figure 3.5: Same as Figure 3.2, but for WASP-95 b

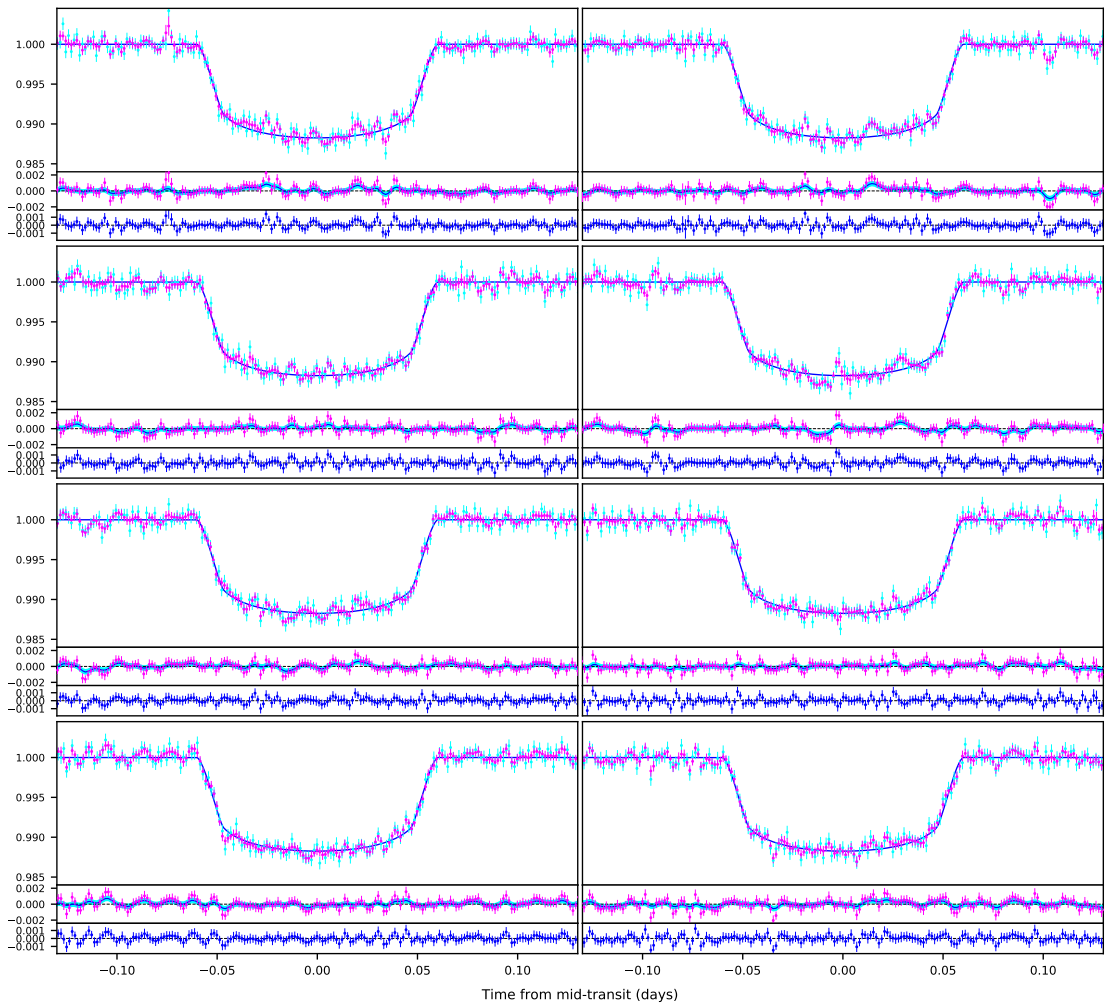


Figure 3.5: Same as Figure 3.2, but for WASP-95 b (*cont.*)

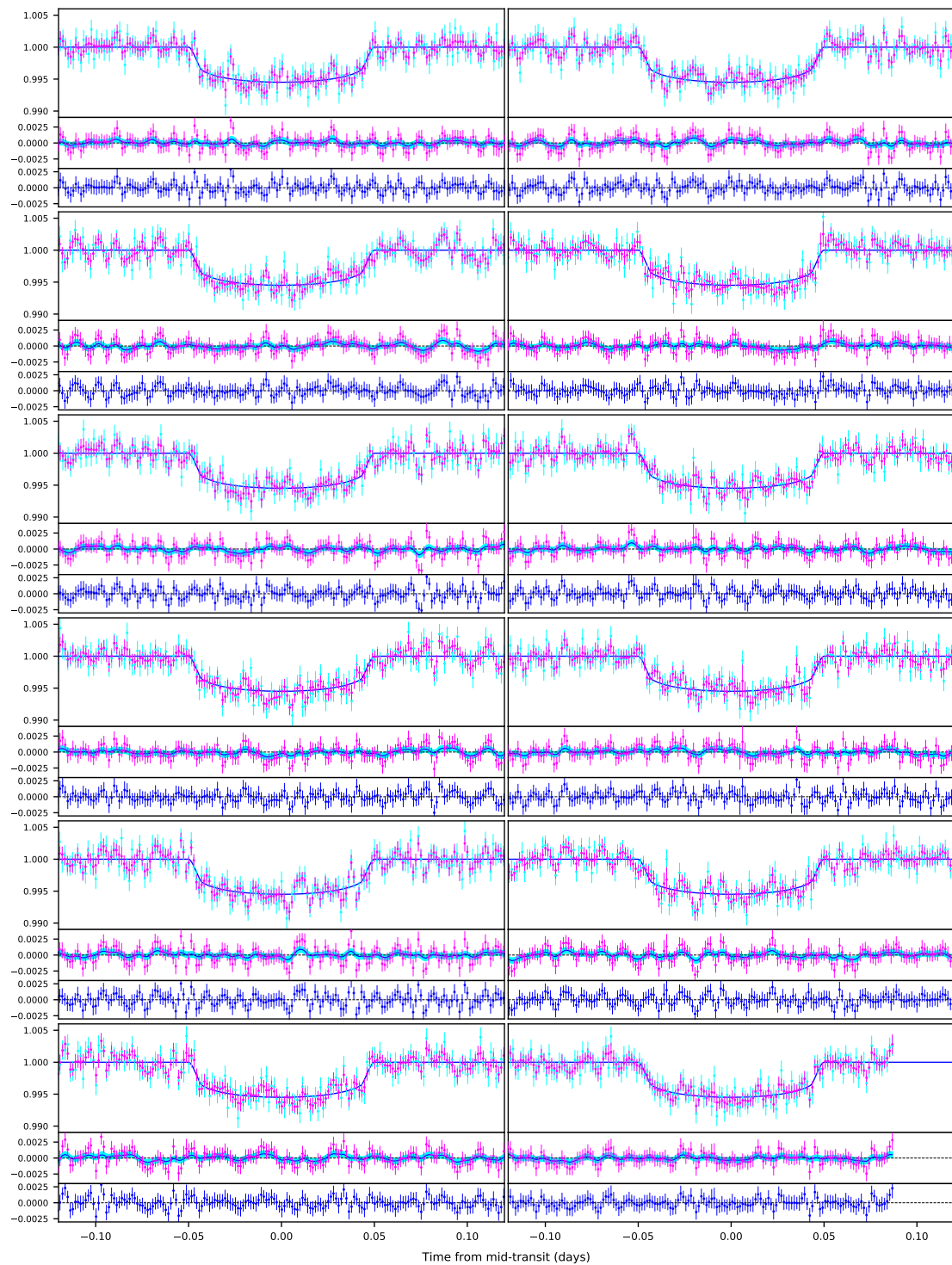


Figure 3.6: Same as Figure 3.2, but for WASP-156 b

Chapter 4

Transit light curves for exomoons: Analytical formalism §

4.1 Introduction

The large number of natural satellites around the planets in our Solar system suggests a high possibility of the existence of such sub-planetary bodies around many of the exoplanets discovered till date. In the past two decades, more than four thousand exoplanets with a wide range of size and mass have been discovered by using various detection techniques. However, the discovery of natural satellites (also known as exomoons) in those systems still remains elusive.

Out of the various detection techniques used for the discovery of exoplanets, the transit method has been proven to be the most effective. Apart from detection, the transit method also provides a way to estimate the size and orbital properties of the exoplanets accurately. However, a shortcoming of the transit method is that the transit probability decreases with the increase in the orbital distance of the exoplanets from their host-stars. Also, with the increase in the orbital distance, the orbital period of the exoplanets increases reducing the probability of detection as it requires continuous monitoring for a longer time-period to confirm the detection. Both these factors have severely constrained the discovery of exoplanets in wider orbits. Previous studies (Dobos et al., 2021; Namouni, 2010; Spalding et al., 2016) has shown that the exoplanets in close-in orbits are likely to lose any natural satellite during the orbital migration. This could be the prime reason behind the lack of discovery of exomoons around the planetary systems discovered till date. With the installation of dedicated survey telescopes, both ground-based and space-based, and a combination of the observations from multiple observing facilities can enable the detection of exoplanets in wider orbits in near future. Such facilities may also enable to detect the natural satellites around the exoplanets.

§Part of this work is published in Suman Saha and Sujana Sengupta 2022 ApJ 936 2, doi:10.3847/1538-4357/ac85a9.

Another major factor that makes it difficult to detect the exomoons through photometric transit method is the requirement of extreme precision. Survey missions like the CoRoT, Kepler and TESS, and the 2m class Hubble Space Telescope have made it possible to detect and study exoplanets as small as the Earth. However, the detection probability of such smaller exoplanets is more around the smaller late-K or M dwarf stars compared to the larger stars of similar apparent magnitude. This is because the precision required to detect exoplanets is proportional to the ratio of disc area of the planet to the star. On the other hand, the largest of the natural satellites in our solar system has a radius even smaller than half of the radius of the Earth. Such smaller natural satellites may be abundant in many exoplanetary systems, but their detection would require a much better photometric precision. All these factors sum up to the inference that the detection of exomoons would require a precision higher than that achievable using the currently available instruments. However, the next generation large telescopes, such as the James Webb Space Telescope (JWST), the European Extremely Large Telescope (E-ELT), the Thirty Meter Telescope (TMT), and the Giant Magellan Telescope (GMT) etc. will make it possible to achieve such extremely high precision. Also, the major improvements in small-scale noise reduction techniques (Chakrabarty & Sengupta, 2019; M. C. Johnson et al., 2015; Livingston et al., 2019; Saha & Sengupta, 2021; Saha et al., 2021) will help in such studies to improve the precision of photometric lightcurves.

As a consequence, it's very much likely that the improved facilities in near future will make it possible to detect the exomoons through photometric transit method. In that case, a self-consistent and mathematically straightforward analytical formalism will be necessary to model the transit lightcurves of stars having moon hosting planets and to estimate the physical properties of the exomoons. The theoretical models need also to be unambiguous enough to be applicable for all possible realistic scenarios of the position of the exomoon with respect to the host exoplanet, and will thus help to strategize the observational parameters to such extremely time-critical observations. We therefore, present in this study a comprehensive and generic analytical formalism for the lightcurves of a transiting exoplanetary system with a exomoon in terms of the radius and orbital parameters of both the planet and the moon. An important aspect of such formalism is to formulate the motion of the three bodies in a common reference frame with respect to the observer. The existing formalism (D. M. Kipping, 2011; Teachey & Kipping, 2018) rely on the rotational transformation of the individual orbits for this purpose. On the other hand, we present a comparatively simple and straightforward analytical formalism

by taking into account only the physically significant orbital parameters of the exoplanet and a circularly orbiting exomoon, such that one can easily model the transit light curves for every possible orbital alignments of the system. To account for the independent spacial inclination of the orbits of the planet and the moon in a simpler way, we have used a two angular parameter approach. We have also provided direct and straightforward solutions to the conditions for various alignments of the star-planet-moon system, especially for the cases where all the three circular bodies intersect with each other. In section 4.2, we discuss the analytical formalism; in section 4.3, we present the results; and in section 4.4, we conclude our study.

4.2 Analytical formalism

Let's consider a natural satellite or moon with radius r_m , orbiting a planet with radius r_p , where r_m and r_p are expressed in term of the radius of the star. If the moon is sufficiently massive, the barycenter of the planet-moon system will be significantly away from the center of the planet even though it lies inside the planetary surface. However, the barycenter will follow the same orbit as the planet would in the absence of a moon. In order to achieve a simple analytical formalism, we have considered a circular orbit for the barycenter around the star. This provides us the advantage of the underlying symmetry. For most of the cases, the orbital eccentricity of an exoplanet can only be estimated by using the radial-velocity method, and a prior knowledge of it would be required to model the transit lightcurve correctly. However, in the absence of a prior information of the eccentricity, by modeling the transit signal for a circular orbit would result in a slightly different value for the orbital semi-major axis and the orbital inclination of the planet. However, it wouldn't affect the orbital properties of the moon.

In the formalism presented here, we have used subscripts s, p, m and b to denote the star, the planet, the moon and the planet-moon barycenter respectively. Now, the separation of the barycenter of the planet-moon system from the center of the star is given by,

$$z_{sb} = a_b \sqrt{\sin^2 \theta_b + \cos^2 \theta_b \cos^2 i_b} \quad (4.1)$$

$$\theta_b = \frac{2\pi}{P_b}(t - t_{0b}) \quad (4.2)$$

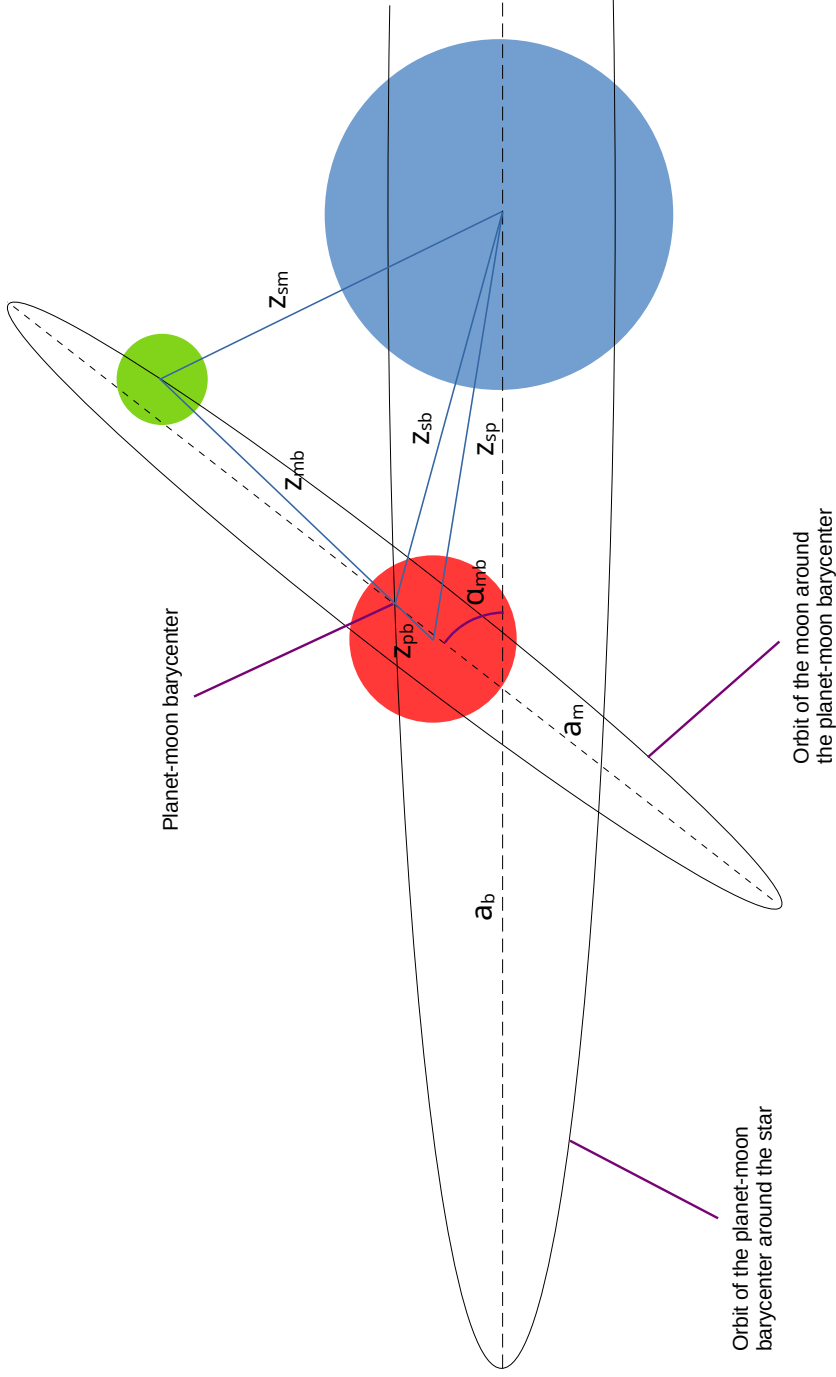


Figure 4.1: Orbital orientation of the star-planet-moon system from the observer's point of view, showing z_{sp} , z_{pm} and z_{sm} , the separations between the centers of the star and the planet, the planet and the moon, and the star and the moon respectively; z_{sb} , z_{pb} and z_{mb} , the separation of the planet-moon barycenter from the centers of the star, the planet and the moon respectively; α_{mb} , the angle between the major axes of the projected orbits of the planet-moon barycenter around the star and the moon around the planet-moon barycenter; a_b and a_m , the orbital semi-major axes of the planet-moon barycenter around the star and the moon around the planet-moon barycenter respectively.

where a_b is the semi-major axis; i_b is the inclination angle; θ_b is the orbital phase; P_b is the orbital period; and t_{0b} is the mid-transit time of the planet-moon barycenter around the star.

If we consider the distance between centers of the moon and the planet to be r_{pm} , the distance of the center of the moon from the planet-moon barycenter is $a_m = r_{pm}/(1 + M_m/M_p)$, where M_m is the mass of the moon and M_p is the mass of the planet; and the distance of the center of the planet from the planet-moon barycenter is $a_p = r_{pm} - a_m$. Now, the separation between the center of the moon and the barycenter of the planet-moon system is given by,

$$z_{mb} = a_m \sqrt{\sin^2 \theta_m + \cos^2 \theta_m \cos^2 i_m} \quad (4.3)$$

$$\theta_m = \frac{2\pi}{P_m}(t - t_{0m}) \quad (4.4)$$

and, the separation of the center of the planet from the barycenter of the planet-moon system can be written as

$$z_{pb} = a_p \sqrt{\sin^2 \theta_m + \cos^2 \theta_m \cos^2 i_m} \quad (4.5)$$

where a_m is the semi-major axes of the moon, a_p is the semi-major axes of the planet; i_m is the inclination angle; θ_m is the orbital phase; P_m is the orbital period; and t_{0m} is the mid-transit time of the moon around the planet-moon barycenter. Note that, the orbital inclination angle of the moon is also measured with respect to the point of view of the observer. The separation between the center of the planet and the center of the moon is,

$$z_{pm} = z_{mb} + z_{pb} \quad (4.6)$$

We denote the angle between the major axes of the projected orbits of the planet-moon barycenter around the star and the moon around the planet-moon barycenter as α_{mb} (see Figure 4.1). Now, the separation between the centers of the planet and the star can be written as,

$$z_{sp} = \sqrt{z_{sb}^2 + z_{pb}^2 - 2z_{sb}z_{pb} \cos \phi} \quad (4.7)$$

$$\phi = \alpha_{mb} + \eta - \eta_1 \quad (4.8)$$

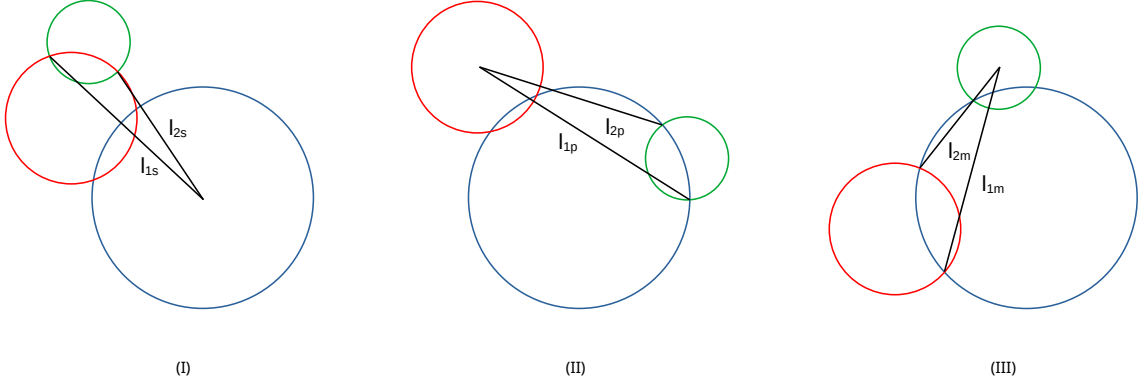


Figure 4.2: (I) Alignment with star-planet and planet-moon intersections showing l_{1s} and l_{2s} , the separation of the star from the points of intersection of the planet and the moon; (II) Alignment with star-planet and star-moon intersections showing l_{1p} and l_{2p} , the separation of the planet from the points of intersection of the star and the moon; (III) Alignment with star-planet and star-moon intersections showing l_{1m} and l_{2m} , the separation of the moon from the points of intersection of the star and the planet.

$$\eta = \begin{cases} \cos^{-1} \frac{\cos \theta_b \cos i_b}{\sqrt{\sin^2 \theta_b + \cos^2 \theta_b \cos^2 i_b}}, & 0 \leq \theta_b \leq \pi \\ -\cos^{-1} \frac{\cos \theta_b \cos i_b}{\sqrt{\sin^2 \theta_b + \cos^2 \theta_b \cos^2 i_b}}, & -\pi \leq \theta_b < 0 \end{cases} \quad (4.9)$$

$$\eta_1 = \begin{cases} \cos^{-1} \frac{\cos \theta_m \cos i_m}{\sqrt{\sin^2 \theta_m + \cos^2 \theta_m \cos^2 i_m}}, & 0 \leq \theta_m \leq \pi \\ -\cos^{-1} \frac{\cos \theta_m \cos i_m}{\sqrt{\sin^2 \theta_m + \cos^2 \theta_m \cos^2 i_m}}, & -\pi \leq \theta_m < 0 \end{cases} \quad (4.10)$$

where ϕ is the angle between z_{sb} and z_{pb} . Similarly, the separation between the centers of the moon and the star is written as,

$$z_{sm} = \sqrt{z_{sb}^2 + z_{mb}^2 - 2z_{sb}z_{mb} \cos \phi_1} \quad (4.11)$$

$$\phi_1 = \pi - \phi \quad (4.12)$$

If the ratio between the mass of the moon and the planet is assumed very small, the barycenter of the planet-moon system could be approximated at the center of the planet, i.e. $a_p = 0$, in which case the model simplifies to $z_{pb} = 0$, $z_{sp} = z_{sb}$ and $z_{pm} = z_{mb}$.

The separation of the star from the points of intersection of the moon and the planet (see Figure 4.2 and Appendix 4.4) are given by,

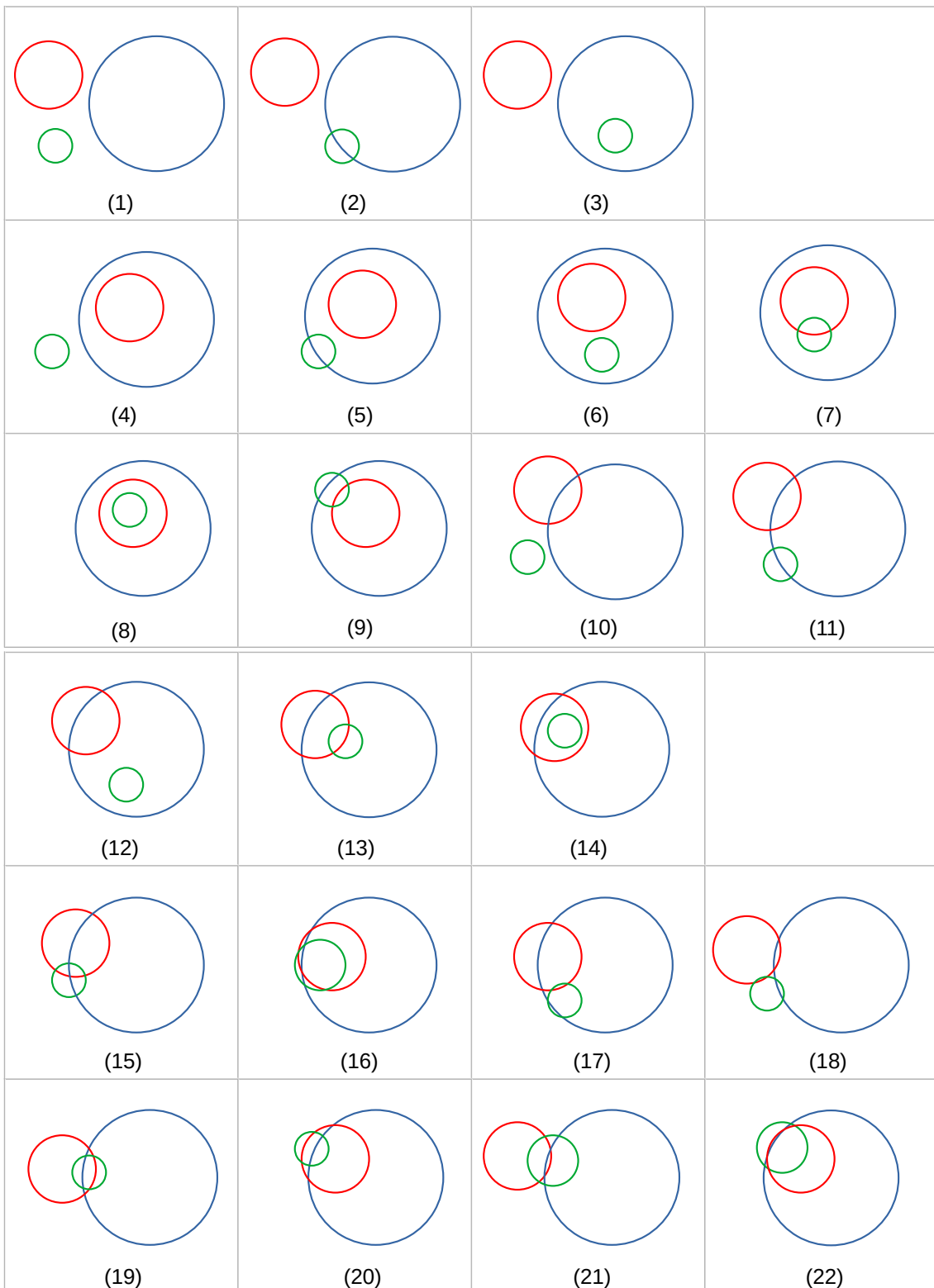


Figure 4.3: An instance of all possible cases of alignments for the star (blue), the planet (red) and the moon (green).

$$l_{1s} = \sqrt{r_p^2 + z_{sp}^2 - 2r_p z_{sp} \cos \left(\cos^{-1} \frac{z_{sp}^2 + z_{pm}^2 - z_{sm}^2}{2z_{sp}z_{pm}} + \cos^{-1} \frac{r_p^2 - r_m^2 + z_{pm}^2}{2z_{pm}r_p} \right)} \quad (4.13)$$

$$l_{2s} = \sqrt{r_p^2 + z_{sp}^2 - 2r_p z_{sp} \cos \left(\cos^{-1} \frac{z_{sp}^2 + z_{pm}^2 - z_{sm}^2}{2z_{sp}z_{pm}} - \cos^{-1} \frac{r_p^2 - r_m^2 + z_{pm}^2}{2z_{pm}r_p} \right)} \quad (4.14)$$

Similarly, the separation of the planet from the points of intersection of the moon and the star are given by,

$$l_{1p} = \sqrt{r_m^2 + z_{pm}^2 - 2r_m z_{pm} \cos \left(\cos^{-1} \frac{z_{pm}^2 + z_{sm}^2 - z_{sp}^2}{2z_{pm}z_{sm}} + \cos^{-1} \frac{r_m^2 - 1 + z_{sm}^2}{2z_{sm}r_m} \right)} \quad (4.15)$$

$$l_{2p} = \sqrt{r_m^2 + z_{pm}^2 - 2r_m z_{pm} \cos \left(\cos^{-1} \frac{z_{pm}^2 + z_{sm}^2 - z_{sp}^2}{2z_{pm}z_{sm}} - \cos^{-1} \frac{r_m^2 - 1 + z_{sm}^2}{2z_{sm}r_m} \right)} \quad (4.16)$$

Also, the separation of the moon from the points of intersection of the star and the planet are given by,

$$l_{1m} = \sqrt{r_p^2 + z_{pm}^2 - 2r_p z_{pm} \cos \left(\cos^{-1} \frac{z_{pm}^2 + z_{sp}^2 - z_{sm}^2}{2z_{pm}z_{sp}} + \cos^{-1} \frac{r_p^2 - 1 + z_{sp}^2}{2z_{sp}r_p} \right)} \quad (4.17)$$

$$l_{2m} = \sqrt{r_p^2 + z_{pm}^2 - 2r_p z_{pm} \cos \left(\cos^{-1} \frac{z_{pm}^2 + z_{sp}^2 - z_{sm}^2}{2z_{pm}z_{sp}} - \cos^{-1} \frac{r_p^2 - 1 + z_{sp}^2}{2z_{sp}r_p} \right)} \quad (4.18)$$

The normalized flux from the star is given by,

$$F = 1 - \frac{F'}{F_T} \quad (4.19)$$

where F_T is the un-obscured flux of the star, and F' is the occulted flux. If F'_p is the flux occulted by the planet and F'_m is that by the moon, then

$$F' = F'_p + F'_m \quad (4.20)$$

Under small-planet approximation, i.e., $r_p, r_m \lesssim 0.1$, we follow the prescription by Mandel and Agol (2002). Hence, we have,

$$F'_p = \frac{2A_{op}}{(\rho_{2p}^2 - \rho_{1p}^2)} \int_{\rho_{1p}}^{\rho_{2p}} I(\rho) \rho d\rho \quad (4.21)$$

$$F'_m = \frac{2A_{om}}{(\rho_{2m}^2 - \rho_{1m}^2)} \int_{\rho_{1m}}^{\rho_{2m}} I(\rho) \rho d\rho \quad (4.22)$$

$$(\rho_{1p}, \rho_{2p}) = \begin{cases} (0, z_{sp} + r_p), & z_{sp} \leq r_p, \\ (z_{sp} - r_p, z_{sp} + r_p), & r_p < z_{sp} < 1 - r_p, \\ (z_{sp} - r_p, 1), & 1 - r_p \leq z_{sp} < 1 + r_p \end{cases} \quad (4.23)$$

$$(\rho_{1m}, \rho_{2m}) = \begin{cases} (0, z_{sm} + r_m), & z_{sm} \leq r_m, \\ (z_{sm} - r_m, z_{sm} + r_m), & r_m < z_{sm} < 1 - r_m, \\ (z_{sm} - r_m, 1), & 1 - r_m \leq z_{sm} < 1 + r_m \end{cases} \quad (4.24)$$

where $I(\rho)$ is the specific intensity, ρ being the radial distance; A_{op} is the area of the stellar disk occulted by the planet; and A_{om} is that occulted by the moon.

Thus, the normalized flux from the star can be written as,

$$F = 1 - \frac{2}{F_T} \left[\frac{A_{op}}{(\rho_{2p}^2 - \rho_{1p}^2)} \int_{\rho_{1p}}^{\rho_{2p}} I(\rho) \rho d\rho + \frac{A_{om}}{(\rho_{2m}^2 - \rho_{1m}^2)} \int_{\rho_{1m}}^{\rho_{2m}} I(\rho) \rho d\rho \right] \quad (4.25)$$

Different alignments of the star, the planet and the moon result into different values of A_{op} and A_{om} . We have categorized all the possible alignments into 22 cases, as shown in Figure 4.3. Similar categorizations were previously provided by Fewell (2006) and D. M. Kipping, 2011. However, we have made a more concise categorization considering only the physically feasible alignments and a more straightforward criteria for where they hold. The conditions where these cases hold, along with the values of A_{op} and A_{om} are listed in Table 4.1. Various terms for the area used in Table 4.1 are as following.

$A_p = \pi r_p^2$ and $A_m = \pi r_m^2$ are the disc areas of the planet and the moon respectively. A_{sp} , A_{pm} and A_{sm} are the areas of intersections of star-planet, planet-moon and star-moon respectively (Mandel & Agol, 2002), given by,

$$A_{sp} = \cos^{-1} \frac{1 - r_p^2 + z_{sp}^2}{2z_{sp}} + r_p^2 \cos^{-1} \frac{r_p^2 - 1 + z_{sp}^2}{2z_{sp}r_p} - \sqrt{z_{sp}^2 - \frac{(1 - r_p^2 + z_{sp}^2)^2}{4}} \quad (4.26)$$

$$A_{pm} = r_p^2 \cos^{-1} \frac{r_p^2 - r_m^2 + z_{pm}^2}{2z_{pm}r_p} + r_m^2 \cos^{-1} \frac{r_m^2 - r_p^2 + z_{pm}^2}{2z_{pm}r_m} - \sqrt{z_{pm}^2 r_p^2 - \frac{(r_p^2 - r_m^2 + z_{pm}^2)^2}{4}} \quad (4.27)$$

$$A_{sm} = \cos^{-1} \frac{1 - r_m^2 + z_{sm}^2}{2z_{sm}} + r_m^2 \cos^{-1} \frac{r_m^2 - 1 + z_{sm}^2}{2z_{sm}r_m} - \sqrt{z_{sm}^2 - \frac{(1 - r_m^2 + z_{sm}^2)^2}{4}} \quad (4.28)$$

Following a similar formalism as given by Fewell (2006), the area of intersection of all the three bodies, i.e., the star, the planet and the moon, (see Figure 4.4) can be written as,

$$A_{spm1} = A_{\Delta} + A_{sa} + A_{pa} + A_{ma1} \quad (4.29)$$

when $D \geq 0$. Otherwise,

$$A_{spm2} = A_{\Delta} + A_{sa} + A_{pa} + A_{ma2} \quad (4.30)$$

where,

$$D = (c_{mx} - c_{pmx})(c_{smy} - c_{pmy}) - (c_{my} - c_{pmy})(c_{smx} - c_{pmx}). \quad (4.31)$$

which determines whether more than half of the moon is within the arc area (see Figure 4.4).

In the above expressions,

$$A_{\Delta} = \sqrt{s(s - s_{sp})(s - s_{pm})(s - s_{sm})}, \quad (4.32)$$

$$A_{sa} = \sin^{-1} \frac{s_{pm}}{2} - \frac{s_{pm}}{4} \sqrt{4 - s_{pm}^2}, \quad (4.33)$$

$$A_{pa} = r_p^2 \sin^{-1} \frac{s_{sm}}{2r_p} - \frac{s_{sm}}{4} \sqrt{4r_p^2 - s_{sm}^2}, \quad (4.34)$$

$$A_{ma1} = r_m^2 \sin^{-1} \frac{s_{sp}}{2r_m} - \frac{s_{sp}}{4} \sqrt{4r_m^2 - s_{sp}^2}, \quad (4.35)$$

$$A_{ma2} = r_m^2 \sin^{-1} \frac{s_{sp}}{2r_m} + \frac{s_{sp}}{4} \sqrt{4r_m^2 - s_{sp}^2}, \quad (4.36)$$

$$s_{sp} = \sqrt{(c_{smx} - c_{pmx})^2 + (c_{smy} - c_{pmy})^2}, \quad (4.37)$$

$$s_{pm} = \sqrt{(c_{spx} - c_{smx})^2 + (c_{spy} - c_{smy})^2}, \quad (4.38)$$

$$s_{sm} = \sqrt{(c_{spx} - c_{pmx})^2 + (c_{spy} - c_{pmy})^2}, \quad (4.39)$$

$$s = \frac{s_{sp} + s_{pm} + s_{sm}}{2}, \quad (4.40)$$

$$(c_{mx}, c_{my}) = (z_{sm} \cos \delta_{sm}, -z_{sm} \sin \delta_{sm}), \quad (4.41)$$

$$\cos \delta_{sm} = \frac{z_{sp}^2 + z_{sm}^2 - z_{pm}^2}{2z_{sp}z_{sm}}, \quad (4.42)$$

$$(c_{spx}, c_{spy}) = \left[\frac{1 - r_p^2 + z_{sp}^2}{2z_{sp}}, -\sqrt{1 - \left(\frac{1 - r_p^2 + z_{sp}^2}{2z_{sp}} \right)^2} \right], \quad (4.43)$$

$$(c_{smx}, c_{smy}) = (c'_{smx} \cos \delta_{sm} + c'_{smy} \sin \delta_{sm}, -c'_{smx} \sin \delta_{sm} + c'_{smy} \cos \delta_{sm}), \quad (4.44)$$

$$(c'_{smx}, c'_{smy}) = \left[\frac{1 - r_m^2 + z_{sm}^2}{2z_{sm}}, \sqrt{1 - \left(\frac{1 - r_m^2 + z_{sm}^2}{2z_{sm}} \right)^2} \right], \quad (4.45)$$

$$(c_{pmx}, c_{pmy}) = (-c''_{pmx} \cos \delta_{pm} + c''_{pmy} \sin \delta_{pm} - z_{sp}, -c''_{pmx} \sin \delta_{pm} + c''_{pmy} \cos \delta_{pm}), \quad (4.46)$$

$$(c''_{pmx}, c''_{pmy}) = \left[\frac{r_p - r_m^2 + z_{pm}^2}{2z_{pm}}, -\sqrt{r_p^2 - \left(\frac{r_p - r_m^2 + z_{pm}^2}{2z_{pm}} \right)^2} \right], \quad (4.47)$$

and

$$\cos \delta_{pm} = \frac{z_{sp}^2 + z_{pm}^2 - z_{sm}^2}{2z_{sp}z_{pm}}. \quad (4.48)$$

Here, A_{Δ} is the area of the triangle and A_{sa} , A_{pa} , A_{ma1} and A_{ma2} are the areas of the arcs within the area of intersection of the three bodies (i.e., the star, the planet and the moon); c_{sp} , c_{pm} and c_{sm} are the coordinates of intersection of the three bodies; and c_m is the coordinate of the center of the moon.

A_{op} and A_{om} , the areas of the stellar disk occulted by the planet and the moon respectively.

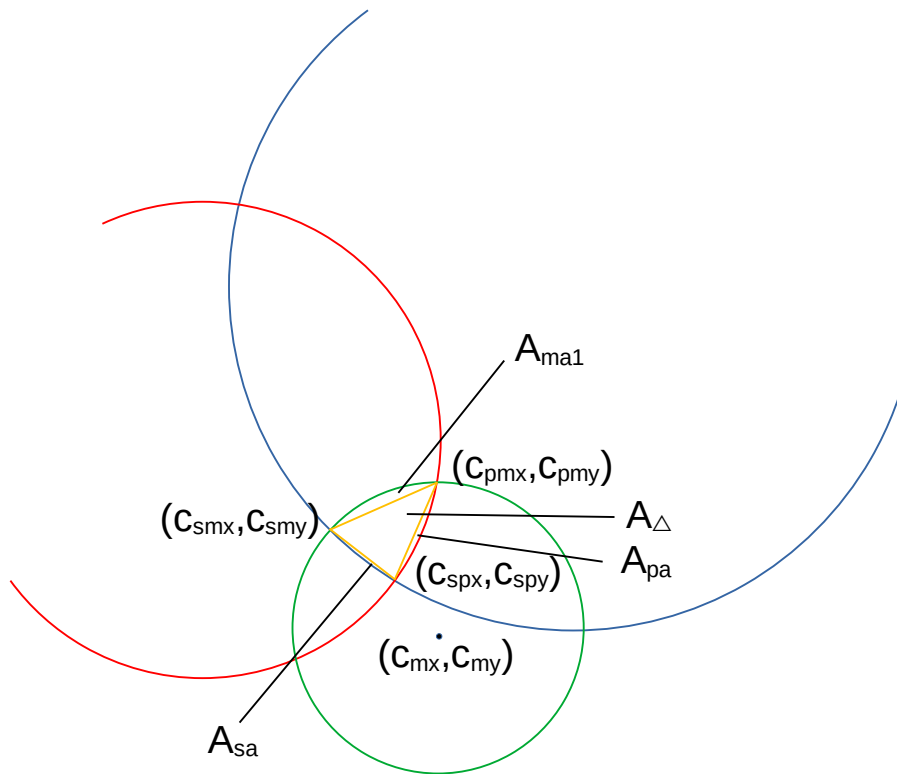


Figure 4.4: Alignment with intersection of all the three bodies (i.e., the star, the planet and the moon) showing A_{Δ} , the area of the triangle and A_{sa} , A_{pa} and A_{ma1} , the areas of the arcs within the common area of intersection of the three bodies.

Table 4.1: Different cases of star-planet-moon alignments

Case	Conditions	A_{op}	A_{om}
1	$z_{sp} \geq 1 + r_p$ $z_{sm} \geq 1 + r_m$	0	0
2	$z_{sp} \geq 1 + r_p$ $1 + r_m > z_{sm} > 1 - r_m$	0	A_{sm}
3	$z_{sp} \geq 1 + r_p$ $z_{sm} \leq 1 - r_m$	0	A_{pm}
4	$z_{sp} \leq 1 - r_p$ $z_{pm} \geq r_p + r_m$ $z_{sm} \geq 1 + r_m$	A_p	0
5	$z_{sp} \leq 1 - r_p$ $z_{pm} \geq r_p + r_m$ $1 + r_m > z_{sm} > 1 - r_m$	A_p	A_{sm}
6	$z_{sp} \leq 1 - r_p$ $z_{pm} \geq r_p + r_m$ $z_{sm} \leq 1 - r_m$	A_p	A_m
7	$z_{sp} \leq 1 - r_p$ $r_p + r_m > z_{pm} > r_p - r_m$ $z_{sm} \leq 1 - r_m$	A_p	$A_m - A_{pm}$
8	$z_{sp} \leq 1 - r_p$ $z_{pm} \leq r_p - r_m$ $z_{sm} \leq 1 - r_m$	A_p	0
9	$z_p \leq 1 - r_{sp}$ $r_p + r_m > z_{pm} > r_p - r_m$ $1 + r_m > z_{sm} > 1 - r_m$	A_p	$A_{sm} - A_{pm}$
10	$1 + r_p > z_{sp} > 1 - r_p$ $z_{sm} \geq 1 + r_m$	A_{sp}	0
11	$1 + r_p > z_{sp} > 1 - r_{sp}$ $z_m \geq r_p + r_m$ $1 + r_m > z_{sm} > 1 - r_m$	A_{sp}	A_{sm}

Table 4.1: Different cases of star-planet-moon alignments (*cont.*)

Case	Conditions	A_{op}	A_{om}
12	$1 + r_p > z_{sp} > 1 - r_p$ $z_{pm} \geq r_p + r_m$ $z_{sm} \leq 1 - r_m$	A_{sp}	A_m
13	$1 + r_p > z_{sp} > 1 - r_p$ $r_p + r_m > z_{pm} > r_p - r_m$ $z_{sm} \leq 1 - r_m$	A_{sp}	$A_m - A_{pm}$
14	$1 + r_p > z_{sp} > 1 - r_p$ $z_{pm} \leq r_p - r_m$	A_{sp}	0
15	$1 + r_p > z_{pm} > 1 - r_p$ $r_p + r_m > z_{pm} > r_p - r_m$ $1 + r_m > z_{sm} > 1 - r_m$ $l_{1m} > r_m > l_{2m}$ $D \geq 0$	A_{sp}	$A_{sm} - A_{spm1}$
16	$1 + r_p > z_{sp} > 1 - r_p$ $r_p + r_m > z_{pm} > r_p - r_m$ $1 + r_m > z_{sm} > 1 - r_m$ $l_{1m} > r_m > l_{2m}$ $D < 0$	A_{sp}	$A_{sm} - A_{spm2}$
17	$1 + r_p > z_{sp} > 1 - r_p$ $r_p + r_m > z_{pm} > r_p - r_m$ $1 + r_m > z_{sm} > 1 - r_m$ $1 \geq l_{1s} \geq l_{2s}$ $l_{1p} \geq l_{2p} \geq r_p$ $l_{1m} \geq l_{2m} \geq r_m$	A_{sp}	$A_{sm} - A_{pm}$
18	$1 + r_p > z_{pm} > 1 - r_p$ $r_p + r_m > z_{pm} > r_p - r_m$ $1 + r_m > z_{sm} > 1 - r_m$ $l_{1s} \geq l_{2s} \geq 1$ $l_{1p} \geq l_{2p} \geq r_p$ $l_{1m} \geq l_{2m} \geq r_m$	A_{sp}	A_{sm}

Table 4.1: Different cases of star-planet-moon alignments (*cont.*)

Case	Conditions	A_{op}	A_{om}
19	$1 + r_p > z_{sp} > 1 - r_p$ $r_p + r_m > z_{pm} > r_p - r_m$ $1 + r_m > z_{sm} > 1 - r_m$ $1 \geq l_{1s} \geq l_{2s}$ $r_p \geq l_{1p} \geq l_{2p}$ $l_{1m} \geq l_{2m} \geq r_m$	A_{sp}	$A_m - A_{pm}$
20	$1 + r_p > z_{sp} > 1 - r_p$ $r_p + r_m > z_{pm} > r_p - r_m$ $1 + r_m > z_{sm} > 1 - r_m$ $l_{1s} \geq l_{2s} \geq 1$ $r_p \geq l_{1p} \geq l_{2p}$ $l_{1m} \geq l_{2m} \geq r_m$	A_{sp}	0
21	$1 + r_p > z_{sp} > 1 - r_p$ $r_p + r_m > z_{pm} > r_p - r_m$ $1 + r_m > z_{sm} > 1 - r_m$ $l_{1s} \geq l_{2s} \geq 1$ $l_{1p} \geq l_{2p} \geq r_p$ $r_m \geq l_{1m} \geq l_{2m}$	A_{sp}	$A_{sm} - A_{sp}$
22	$1 + r_p > z_{sp} > 1 - r_p$ $r_p + r_m > z_{sp} > r_p - r_m$ $1 + r_m > z_{sm} > 1 - r_m$ $1 \geq l_{1s} \geq l_{2s}$ $l_{1p} \geq l_{2p} \geq r_p$ $r_m \geq l_{1m} \geq l_{2m}$	A_{sp}	$A_{sm} - A_{pm} + (A_p - A_{sp})$

Note: A_{op} and A_{om} are the areas of the stellar disk occulted by the planet and the moon respectively.

4.3 Results and discussion

The model parameters in the present formalism are r_p , r_m , t_{0b} , t_{0m} , P_b , P_m , r_{pm} , M_p/M_m , i_b , i_m , α_{mb} , and the limb-darkening coefficients of the host-star defining $I(\rho)$, where all the distances are in terms of stellar radius. Here we have used the quadratic limb-darkening formula (Claret, 2000; Claret & Gimenez, 1990), given by

$$I(\rho)/I(0) = 1 - u_1(1 - \mu) - u_2(1 - \mu)^2, \quad (4.49)$$

where $\mu = \sqrt{1 - \rho^2}$, and u_1 and u_2 are the quadratic limb-darkening coefficients.

While generating the model transit lightcurves, we have used the analytical quadratic limb-darkening formalism for transit flux given by Mandel and Agol (2002). In the absence of such an analytical quadratic limb-darkening formula, we have used the small-body approximation to estimate the transit flux for the cases where all the three circular bodies overlap (see Section 4.2).

Let us now consider a scenario with $r_p = 0.1$, $r_m = 0.01$, $t_{0b} = 5$ days, $t_{0m} = 10$ days, $P_b = 300$ days, $P_m = 20$ days, $r_{pm} = 200$, $M_p/M_m = 1411$, $i_b = 90^\circ$, $i_m = 90^\circ$, $\alpha_{mb} = 0^\circ$, $u_1 = 0.4$ and $u_2 = 0.25$. Clearly, $i_b = i_m = 90^\circ$ implies that both the planet and the moon are transiting through the center of the star, and that combined with $\alpha_{mb} = 0^\circ$ implies that the orbit of the moon is aligned with the orbit of the planet, i.e., both the planet and the moon are in the same orbital plane. The transit lightcurve for this scenario is shown in Figure 4.5(a). Usually, the transit of the moon can take place before, during or after the transit of the planet depending upon a combination of various parameters. For this scenario, we can see that the transit of the moon starts after the end of the planet's transit, as the moon is placed in a wide orbit around the planet and its position makes it highly trailing while transiting the star. If we change the position of the moon by replacing $t_{0m} = 8$ days, as shown in Figure 4.5(b), we can see that the transit of the moon starts before the end of the transit of the planet.

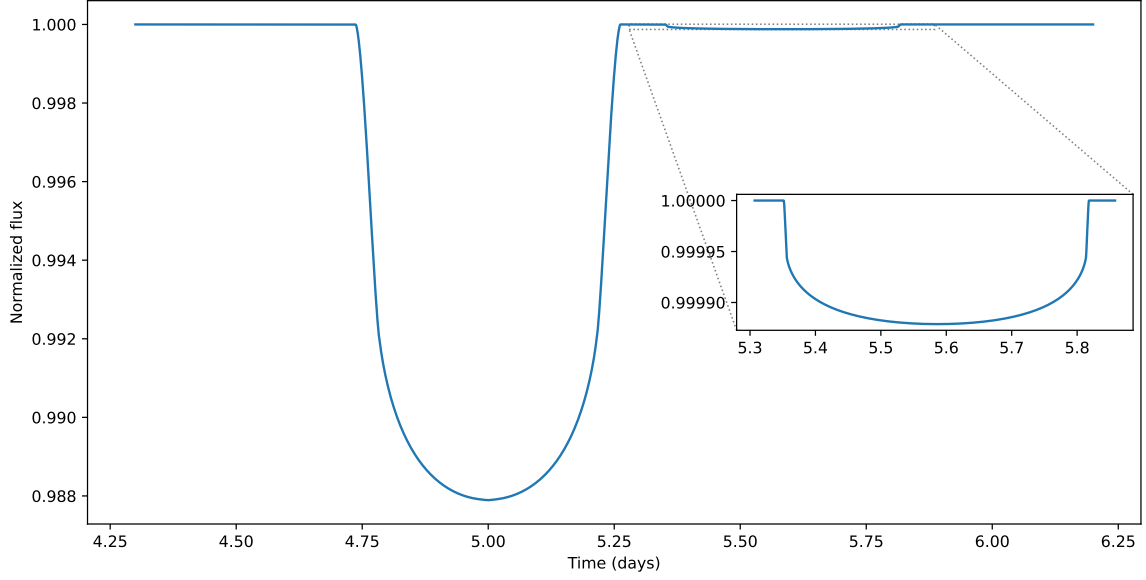
The alignment of the orbit of an exomoon depends upon the formation and evolution path it followed. If the moon is formed from the circumplanetary disc, there is a higher probability for its orbit to be equatorial and it might be co-aligned (co-planer) with the planetary orbit (Peale, 1999). On the other hand, if the moon is formed through planetary capture or collision, its orbit may not be co-aligned with the orbit of the planet. Both these situations can easily be modeled by using our formalism. When $i_b = i_m$ and $\alpha_{mb} = 0$, the orbits are co-aligned. On the contrary, when $i_b \neq i_m$ and/or $\alpha_{mb} \neq 0$, the orbits are no longer co-aligned with each other. To

demonstrate it, let's consider a scenario by replacing $\alpha_{mb} = 20^\circ$ in the first scenario. As shown in Figure 4.6(a), we can see that both the transit depth and duration of the moon has decreased. This is because, in this case the moon is transiting towards the edge of the star instead of through the center as was in the case of the first scenario.

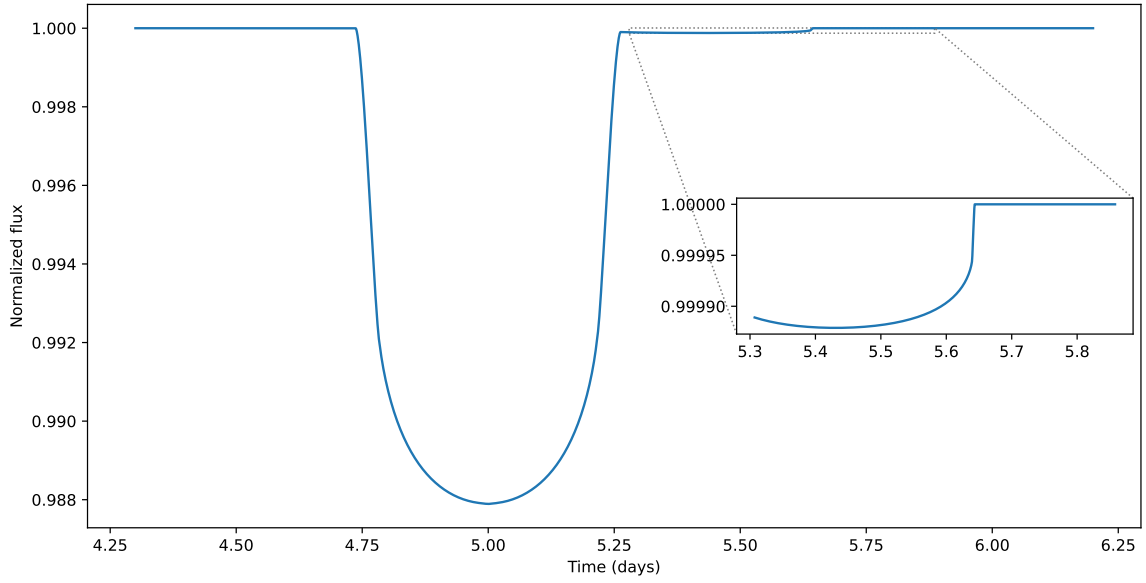
Obviously, if the moon is in a position such that it is fully transiting the planet or is fully eclipsed by it, while transiting the star, no transit signal due to the moon could be observed. Also, if the moon is in a wide and highly inclined orbit as compared to that of the planet, it may not transit the star every time the planet transits it (Martin et al., 2019). For example, if we replace $\alpha_{mb} = 30^\circ$ in the previous case, no transit is observed for the moon. However, if the position of the moon is changed by replacing $t_{0m} = 8$ days, the transit of the moon is observed as shown in Figure 4.6(b). Combining these factors along with the fact that exomoons are more likely to be found around planets in wider orbits around their host-stars, i.e. planets with much longer orbital period than a few days, it would require long period surveys continuously monitoring a particular portion of the sky to detect the exomoons. However, such surveys are also likely to increase the number of large period exoplanets, including the habitable-zone terrestrial exoplanets, thereby increasing their effectiveness by detecting many interesting planetary and sub-planetary mass bodies.

The photometric precision required to detect the exomoons is directly related to the transit depth, which is in turn dependent upon the ratio of disc area of the moon to that of the star. The required photometric precision is minimum for an exomoon in a system with a smaller M-dwarf type star. Let's consider such a system with a moon of the size of the Moon around a planet of the size of the Earth, i.e. $r_p = 0.075$, $r_m = 0.02$, $t_{0b} = 5$ days, $t_{0m} = 10$ days, $P_b = 60$ days, $P_m = 15$ days, $r_{pm} = 25$, $M_p/M_m = 81$, $i_b = 90^\circ$, $i_m = 90^\circ$, $\alpha_{mb} = 0^\circ$, $u_1 = 0.4$ and $u_2 = 0.25$, the light-curve for which is shown in Figure 4.7(a). If we change the position of the moon by replacing $t_{0m} = 5$ days, there would arise a scenario where the moon transits the planet while simultaneously transiting the star as well. Such a scenario is presented in Figure 4.7(b).

To demonstrate the affect of the moon on the transit timing of the planet, we have co-plotted the transit lightcurve of the planet in the absence of a moon in Figure 4.7(a). Comparing the two lightcurves, the transit-time-variation (TTV) can be observed. For a practical scenario, it could be difficult to detect the TTV in the observed transit data, as the barycentric offset from the center of the planet is quite small compared to the distance between the centers of the planet and the moon, even for a smaller mass ratio between the planet and the moon (e.g. the earth-moon

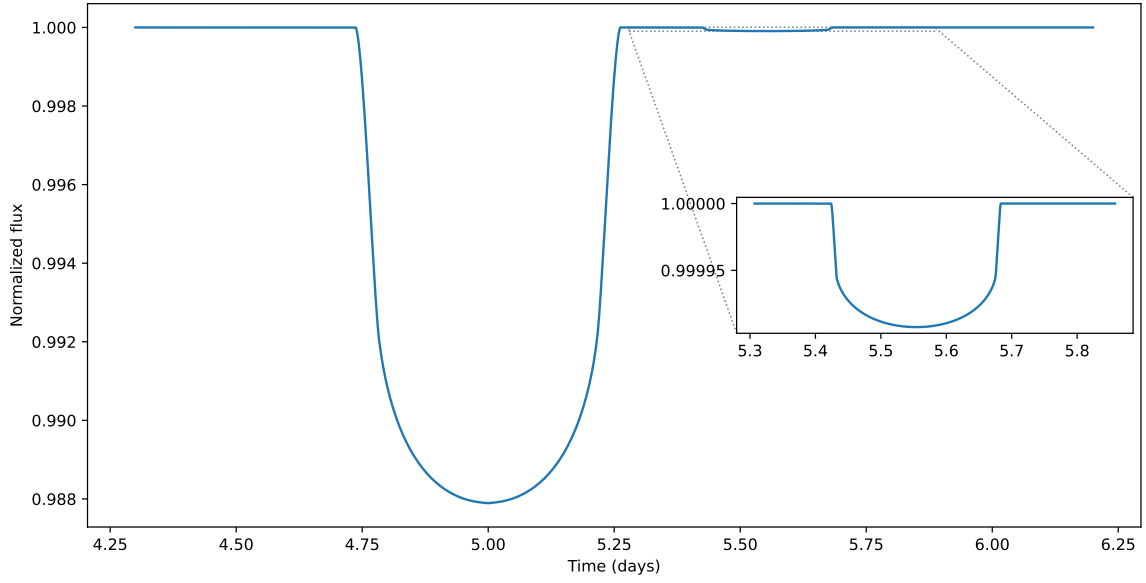


(a)

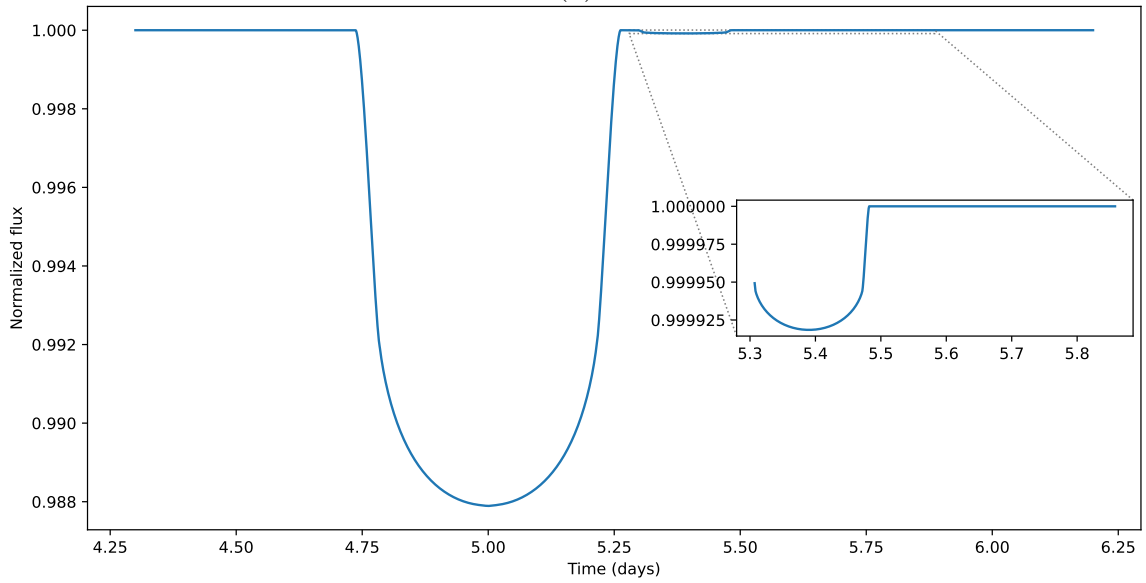


(b)

Figure 4.5: Transit light-curves of a moon hosting exoplanetary system: (a) with $r_p = 0.1$, $r_m = 0.01$, $t_{0b} = 5$ days, $t_{0m} = 10$ days, $P_b = 300$ days, $P_m = 20$ days, $r_{pm} = 200$, $M_p/M_m = 1411$, $i_b = 90^\circ$, $i_m = 90^\circ$, $\alpha_{mb} = 0^\circ$, $u_1 = 0.4$ and $u_2 = 0.25$; and (b) replacing $t_{0m} = 8$ days.



(a)



(b)

Figure 4.6: Transit light-curves of a moon hosting exoplanetary system: (a) with $r_p = 0.1$, $r_m = 0.01$, $t_{0b} = 5$ days, $t_{0m} = 10$ days, $P_b = 300$ days, $P_m = 20$ days, $r_{pm} = 200$, $M_p/M_m = 1411$, $i_b = 90^\circ$, $i_m = 90^\circ$, $\alpha_{mb} = 20^\circ$, $u_1 = 0.4$ and $u_2 = 0.25$; and (b) replacing $t_{0m} = 8$ days and $\alpha_{mb} = 30^\circ$.

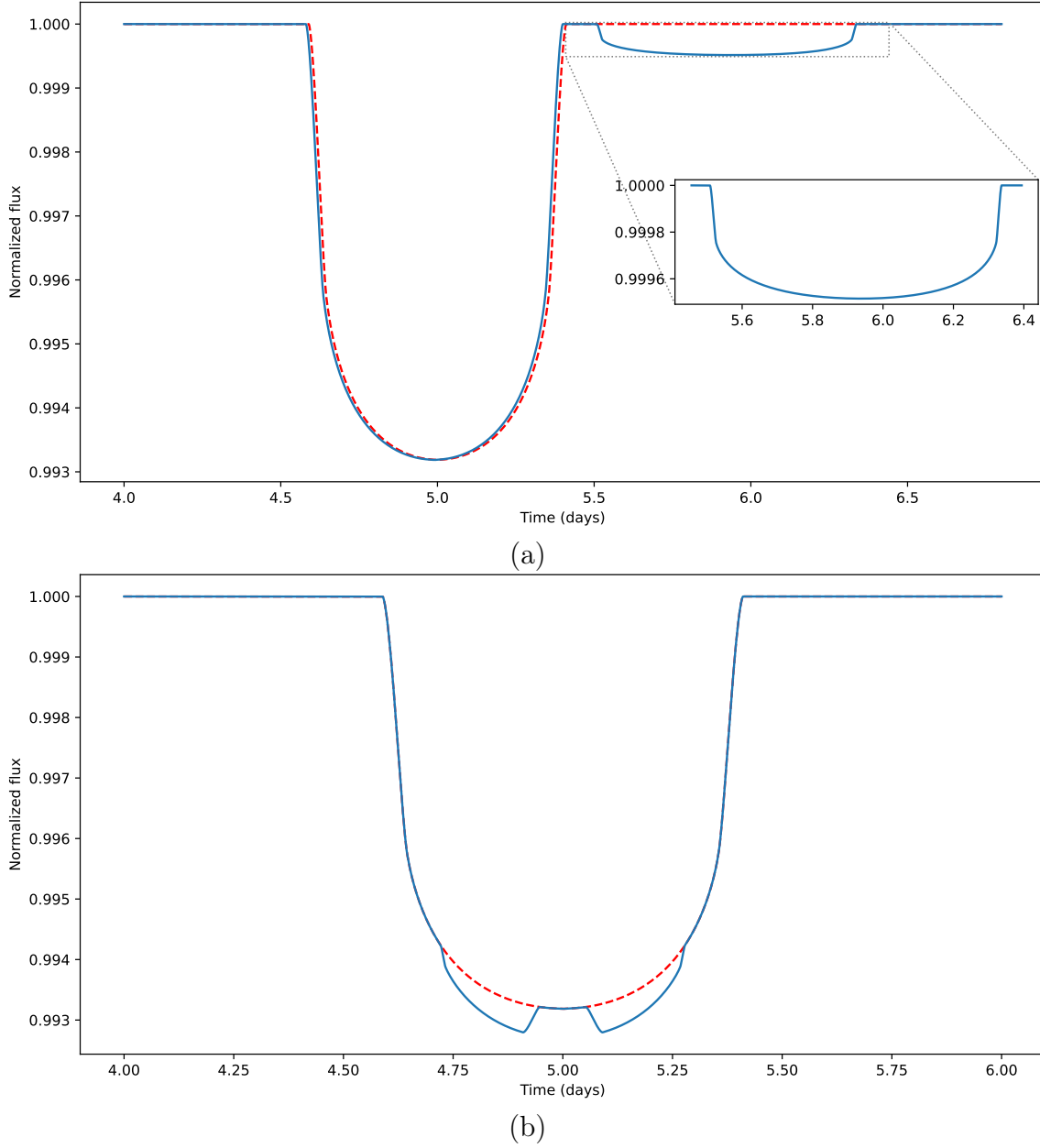


Figure 4.7: Transit light-curves of a moon hosting exoplanetary system: (a) with $r_p = 0.075$, $r_m = 0.02$, $t_{0b} = 5$ days, $t_{0m} = 10$ days, $P_b = 60$ days, $P_m = 15$ days, $r_{pm} = 25$, $M_p/M_m = 81$, $i_b = 90^\circ$, $i_m = 90^\circ$, $\alpha_{mb} = 0^\circ$, $u_1 = 0.4$ and $u_2 = 0.25$; and (b) same but with $t_{0m} = 5$ days. The dashed red lines show the transit lightcurves of the planet in the absence of a moon. The transit-time-variation (TTV) due to the presence of a moon can be observed in (a).

system, where $M_p/M_m \simeq 81$).

On the other hand, a higher precision would be required for systems with a larger host-star. The minimum photometric precision required to detect a terrestrial exoplanet of the size of the Earth around a star similar to the Sun is about 100 ppm (parts-per-million). Therefore, a precision much better than that would be required to detect the exomoons around such systems. Such extremely high precision is expected to be achievable using the next generation large telescopes, such as the James Webb Space Telescope (JWST), the European Extremely Large Telescope (E-ELT), the Thirty Meter Telescope (TMT), and the Giant Magellan Telescope (GMT) etc. Also, the instrumental and atmospheric noise effects has to be minimized for such observations. This can be achieved by using small-scale noise reduction techniques such as the wavelet denoising (Chakrabarty & Sengupta, 2019; Donoho & Johnstone, 1994; Saha, 2023; Saha & Sengupta, 2021; Saha et al., 2021). The stellar variability and pulsations can also cause a challenge in such observations, which need to be reduced using techniques like the Gaussian process regression (Chakrabarty & Sengupta, 2019; M. C. Johnson et al., 2015; Rasmussen & Williams, 2006; Saha, 2023; Saha & Sengupta, 2021; Saha et al., 2021).

4.4 Conclusion

In this study, we have presented an analytical formalism to model the transit lightcurves for a system with a transiting exoplanet hosting an exomoon. The formalism uses the radius and orbital properties of both the planet and the moon as model parameters. The orbital alignment of the moon is taken care by introducing two angular parameters and hence both co-aligned and non-coaligned orbit of a moon with respect to the planetary orbit can be modeled easily. This also enables to model every possible scenarios of alignments for the star-planet-moon system using this formalism.

The detection of exomoons requires extremely high precision observations which is expected to be achievable using the next generation very large telescopes along with the implementation of the existing critical noise reduction techniques. In such possibilities, our transit formalism could be useful to model the lightcurves in order to characterize the physical properties of the exomoons as well as to simulate every possible scenarios and make strategies for such extremely time-critical observations.

Appendix: Derivation of l_{1s} and l_{2s}

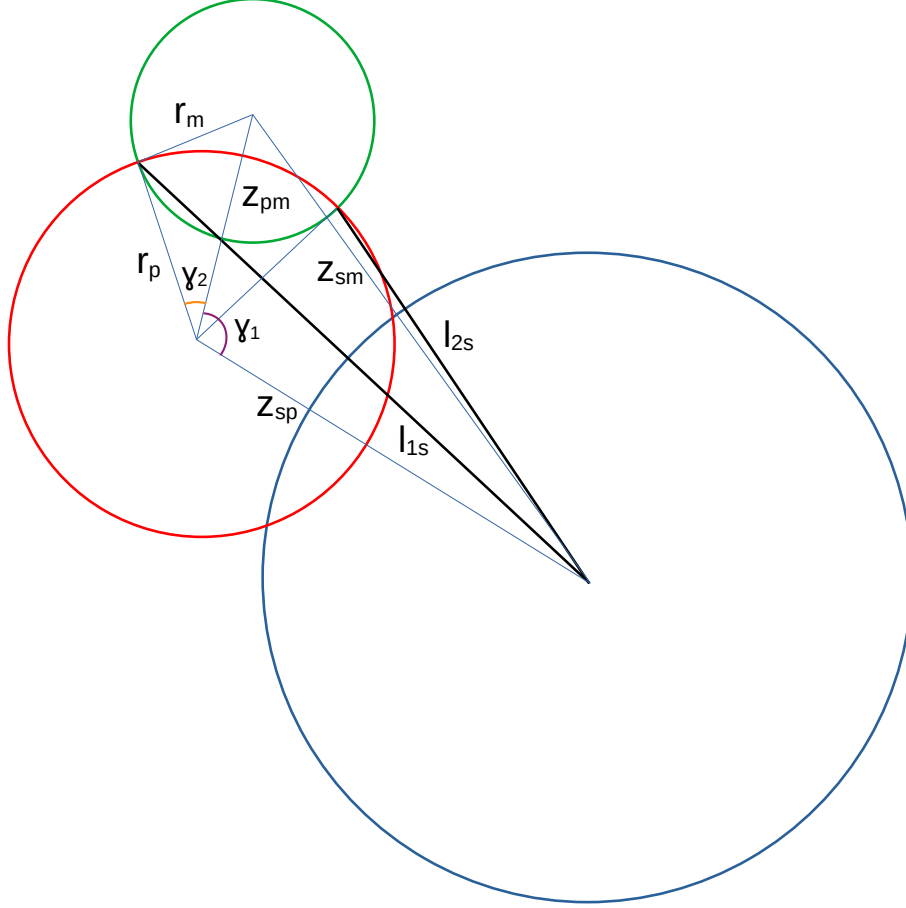


Figure 4.8: Alignment of the three bodies with star-planet and planet-moon intersections.

From Figure 4.8, the angles γ_1 and γ_2 can be written as,

$$\gamma_1 = \cos^{-1} \left(\frac{z_{sp}^2 + z_{pm}^2 - z_{sm}^2}{2z_{sp}z_{pm}} \right) \quad (4.50)$$

$$\gamma_2 = \cos^{-1} \left(\frac{r_p^2 - r_m^2 + z_{pm}^2}{2z_{pm}r_p} \right) \quad (4.51)$$

Now, l_{1s} and l_{2s} can be written as,

$$\begin{aligned}
l_{1s} &= \sqrt{r_p^2 + z_{sp}^2 - 2r_p z_{sp} \cos(\gamma_1 + \gamma_2)} \\
&= \sqrt{r_p^2 + z_{sp}^2 - 2r_p z_{sp} \cos \left(\cos^{-1} \frac{z_{sp}^2 + z_{pm}^2 - z_{sm}^2}{2z_{sp}z_{pm}} + \cos^{-1} \frac{r_p^2 - r_m^2 + z_{pm}^2}{2z_{pm}r_p} \right)}
\end{aligned} \tag{4.52}$$

$$\begin{aligned}
l_{2s} &= \sqrt{r_p^2 + z_{sp}^2 - 2r_p z_{sp} \cos(\gamma_1 - \gamma_2)} \\
&= \sqrt{r_p^2 + z_{sp}^2 - 2r_p z_{sp} \cos \left(\cos^{-1} \frac{z_{sp}^2 + z_{pm}^2 - z_{sm}^2}{2z_{sp}z_{pm}} - \cos^{-1} \frac{r_p^2 - r_m^2 + z_{pm}^2}{2z_{pm}r_p} \right)}
\end{aligned} \tag{4.53}$$

l_{1p} , l_{2p} , l_{1m} and l_{2m} can also be derived in a similar fashion.

Chapter 5

Detection of habitable exomoons in the JWST era

5.1 Introduction

Since the detection of the first exoplanet using transit method (Charbonneau et al., 2000), thousands of exoplanets have been discovered using this method through several ground as well as space based missions. However, the discovery of natural satellites in such exoplanetary systems (also known as exomoons) has still remained elusive. Considering the number of natural satellites discovered around the planets in our solar system, the existence of such exomoons is very plausible. However, their non-discovery till date could be attributed to the fact that the satellites tend to be much smaller in size than the planets they orbit around.

Although the transit method favors the discovery of close-in hot-Jupiters and other giant planets, several giant exoplanets have also been discovered in the habitable zone of their host-stars. While such giant planets in the habitable zones may not be of particular interest in terms of habitability, any rocky exomoon around such an exoplanets could sustain life.

The recently commissioned James Webb Space Telescope (JWST) is the largest space-based telescope developed till date, and hence provides unique opportunity to study the habitable exomoons. In this work, we have studied the detectability of such exomoons through JWST. We have also studied the capability of JWST for the study of atmospheric composition for such exomoons to determine their habitability.

In section 5.2, we have discussed about transiting exomoons and their lightcurves. In section 5.3, we have discussed about the detectability of rocky exomoons in the habitable zones of their host stars through JWST. And in section 5.4, we have summerized the conclusions of this work.

Table 5.1: Physical properties of stellar and planetary bodies

Object	Radius [km]	Mass[kg]	Temperature [K]
G2 star	7×10^5	2×10^{30}	5778
K2 star	5.11×10^5	1.64×10^{30}	5084
Jupiter	7×10^4	1.9×10^{27}	—
Mars	3.39×10^3	6.4×10^{23}	—
Titan	2.58×10^3	1.4×10^{23}	—
Luna	1.74×10^3	7.4×10^{22}	—

5.2 Transiting exomoons

Although most of the exoplanets discovered till date are in the closed-in orbits around their host stars, exomoons are expected to be present around planets in wider orbits. This is because the planets are likely to lose any natural satellite present during their migration to the inner orbits (Dobos et al., 2021; Namouni, 2010; Spalding et al., 2016). In the case of M-type and late K-type stars, the habitable zones fall at a distance very close to the host stars, which may result in an absence of habitable zone exomoons in such systems. On the other hand, early type stars have habitable zones placed significantly away from the host stars, which also reduces the detection probability of transiting exoplanets and hence transiting exomoons in the habitable zones of such systems. We have, therefore, considered two different cases for host-stars, i.e. G2 and K2 type, which are optimal for the study of habitable exomoons. We have considered an exoplanet similar to the size of the Jupiter and three different cases for the exomoons, with sizes similar to the Mars, the Titan and the Luna in the habitable zones of these host-stars. The physical properties of these bodies which are used in our study is listed in Table 5.1.

The distance of the habitable zone from the host-stars is considered to be equivalent to the Earth’s distance from the Sun, i.e.

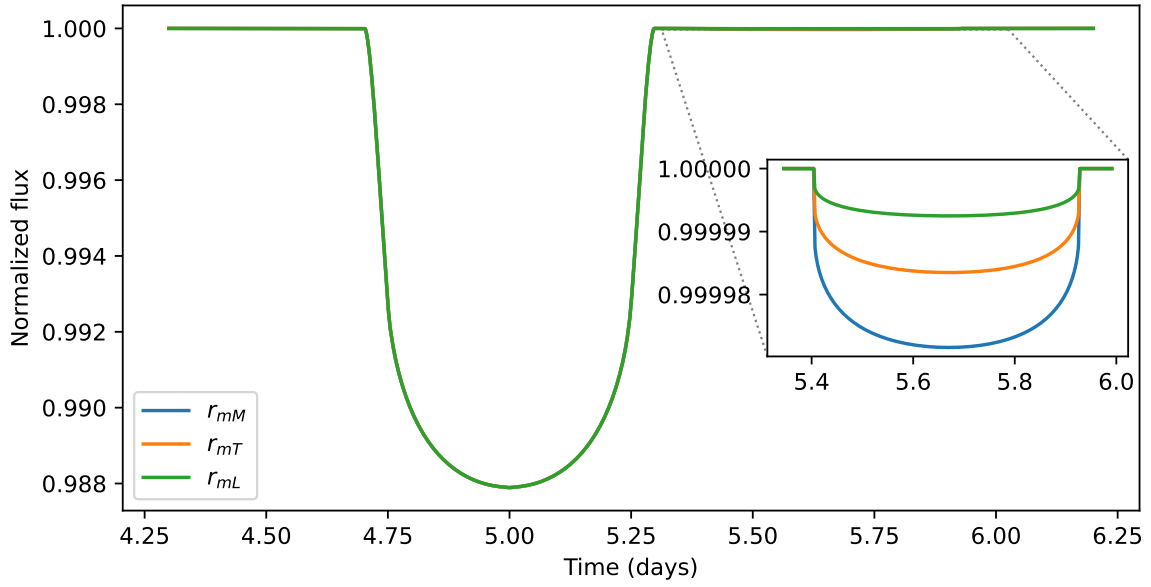
$$a_{HZ} = 1\text{AU} \times (L_{star}/L_{sun})^{0.5} \quad (5.1)$$

We have considered that the barycenter of the planet-moon system follows the same path around the host-star, as the planet would have followed in the absence of a moon. We have also considered that the moon follows a circular path around the planet-moon barycenter. These assumptions simplifies the three body problem

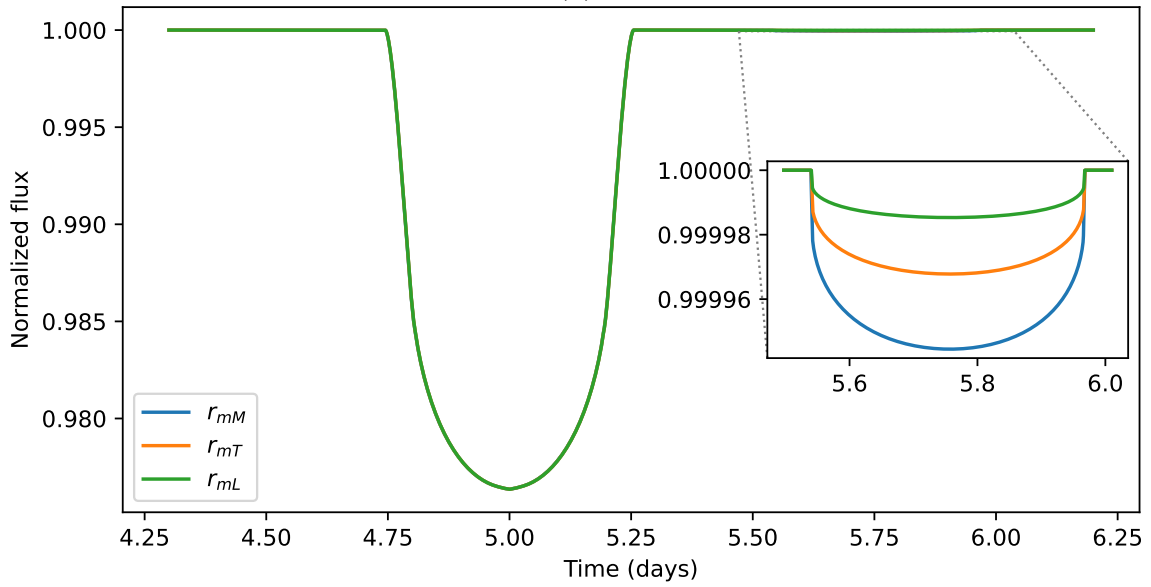
Table 5.2: Transit parameters for different scenarios

Parameter	G2 Star	K2 Star
r_p	0.1	0.137
r_{mM}	0.00484	0.00663
r_{mT}	0.00369	0.00505
r_{mL}	0.00249	0.00341
$t_{0b}[Days]$	5	5
$t_{0m}[Days]$	9	9
$P_b[Days]$	365	171.2
$P_m[Days]$	14.47	14.47
$a_b[AU]$	1	0.565
r_{pm}	2.5	3.42
M_J/M_M	2968.75	2968.75
M_J/M_T	13571.4	13571.4
M_J/M_L	25675.7	25675.7
i_b	90	90
i_m	90	90
α_{mb}	0	0
u_1	0.4	0.55
u_2	0.25	0.15

and enables to solve for the trajectories analytically. Saha and Sengupta, 2022 has given a detailed analytical formalism to model the transit lightcurves for a transiting exoplanet hosting an exomoon. The model parameters used in this formalism are, radius of the planet (r_p); radius of the moon (r_m); mid-transit time (t_{0b}), orbital period (P_b), semi-major axis (a_b), and the orbital inclination angle (i_b) of the barycenter of the planet-moon system around the host-star; mid-transit time (t_{0m}), orbital period (P_m), and the orbital inclination angle (i_m) of the moon around the planet-moon barycenter, mass ratio of the planet and the moon (M_p/M_m), distance between the planet and the moon (r_{pm}); the angular separation between the major axes of the two projected orbits, i.e. the orbit of the planet-moon barycenter around the star and the orbit of the moon around the planet-moon barycenter, (α_{mb}); and the (quadratic) limb-darkening coefficients (u_1, u_2).



(a)



(b)

Figure 5.1: Transit lightcurves corresponding to the parameter values given in Table 5.2 with the host-stars being (a) G2 and (b) K2 type.

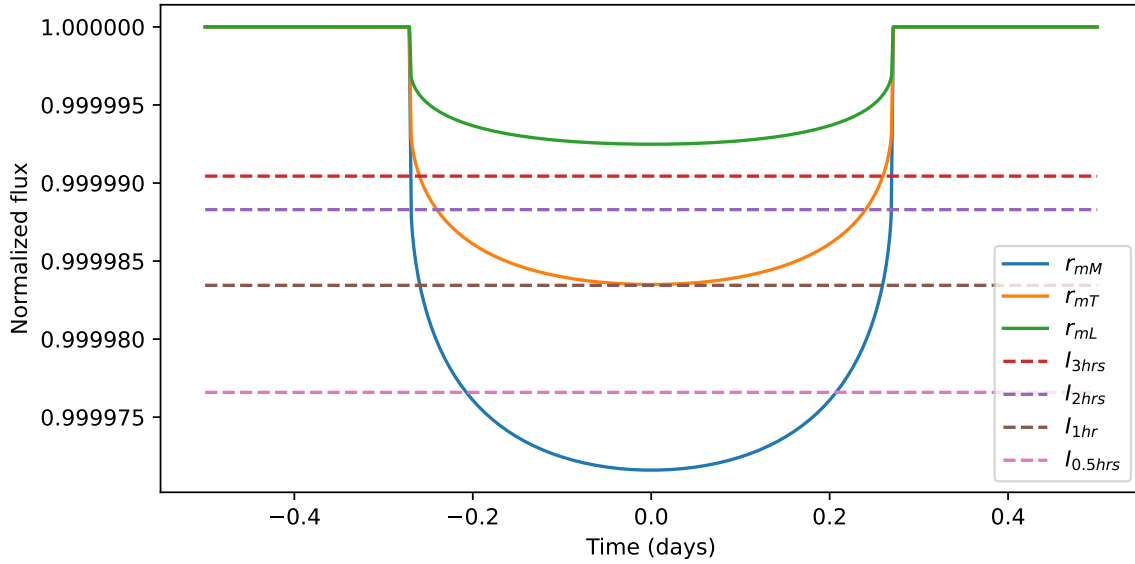
The parameter values corresponding to different scenarios are given in Table 5.2. The transit lightcurves corresponding to these scenarios are shown in Figure 5.1, where the portion of the lightcurve have been zoomed in to show the transit signature of the exomoons.

5.3 Detection of transiting exomoons through JWST

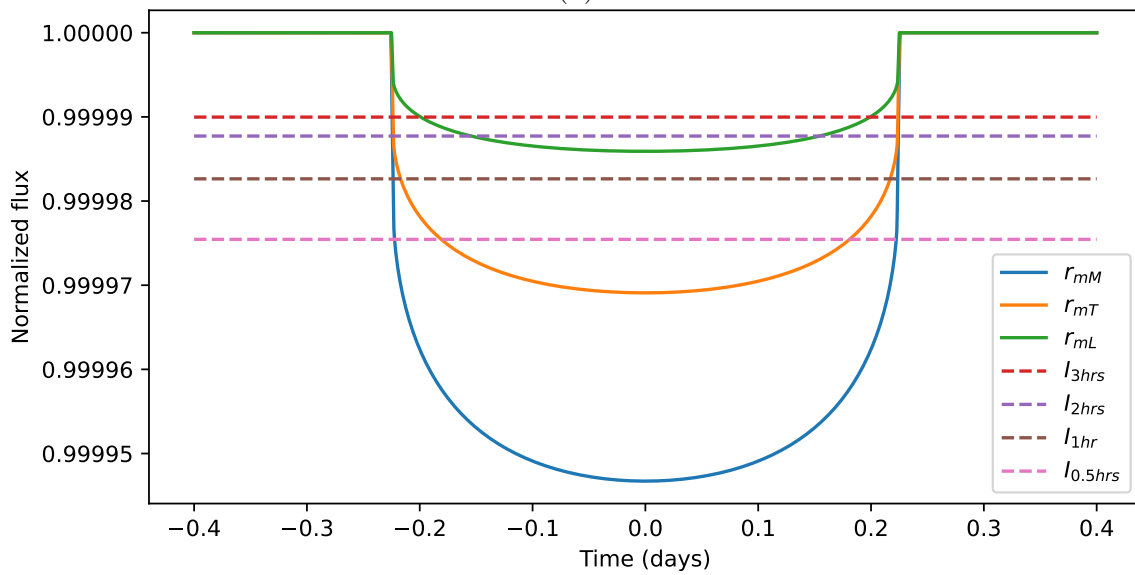
In order to estimate the SNR for the photometric observations using JWST, we have used the JWST Exposure time calculator ^{*}, which is based on Pandeia (Pontoppidan et al., 2016). The NIRCAM instrument of JWST is capable of photometric observations in a wide range of wide, mid and narrow band filters. For brighter host stars with V_{mag} 8 and 9 for G2 and K2 spectral types respectively, we have used the narrow band filter F187N while estimating the SNR. Similarly, for fainter host stars with V_{mag} 11.5 and 12.5 for G2 and K2 spectral types respectively, we have used the wide band filter F150W. These stellar magnitudes and corresponding photometric filters of JWST have been selected in order to obtain high SNR per exposure without saturation. Depending upon the value of several transit parameters, and especially the position of the moon with respect to the planet at the time of transit, we could either have part of the transit of the moon coincided with the transit of the planet, or the whole of the transit of the moon outside the transit of the planet (as the cases shown in Figure 5.1). We have estimated the SNR for a photometric integration time, I (henceforth “integration time”), of 0.5 hrs, 1 hr, 2 hrs and 3 hrs for both the G2 and K2 type host-stars. We have compared these expected photometric precision with the transit depths for different sizes of the exomoons for the scenarios given in Table 5.2, as plotted in Figure 5.2.

From Figure 5.2, it is clear that for both the cases of G2-type host stars, an exomoon with a size similar to Mars would be detectable for an integration time of 30 minutes. On the other hand, if the size of the moon is similar to Titan, it will be detectable for an integration time of 2 hours. It is also worth noticing that an exomoon with a size similar to Luna would be undetectable even with an integration time of 3 hours for these scenarios. On the other hand, for both the cases of K2-type host stars, an exomoon with size similar to Mars or Titan would be detectable for an integration time of 30 minutes. Also, unlike the scenarios of G2-type host stars, an exomoon with a size similar to Luna would be marginally detectable for an integration time of 2 hours and comfortably detectable for an integration time of 3

^{*}<https://jwst.etc.stsci.edu/>

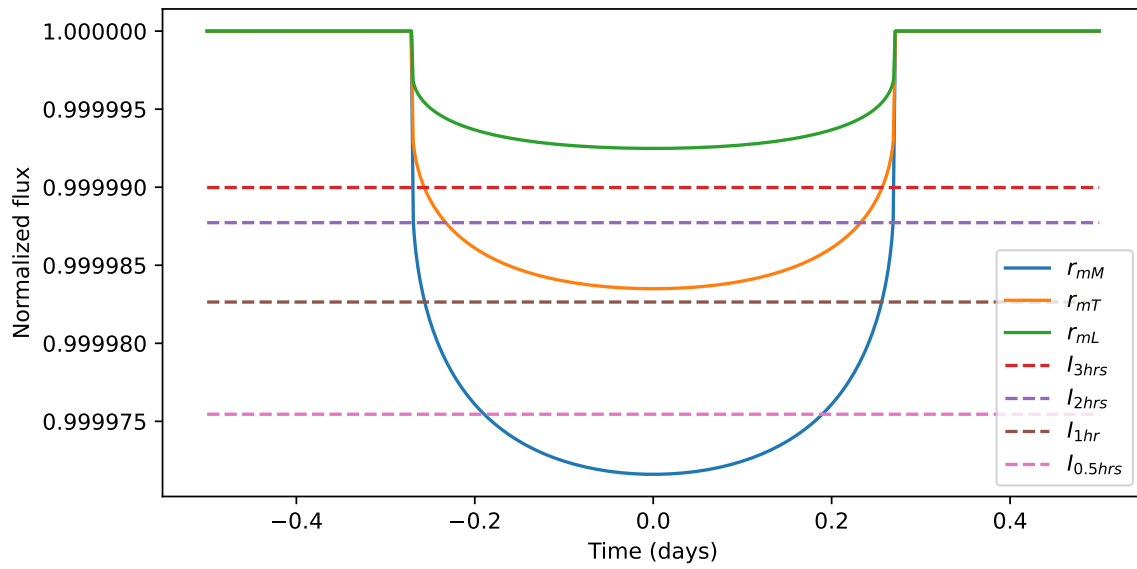


(a)

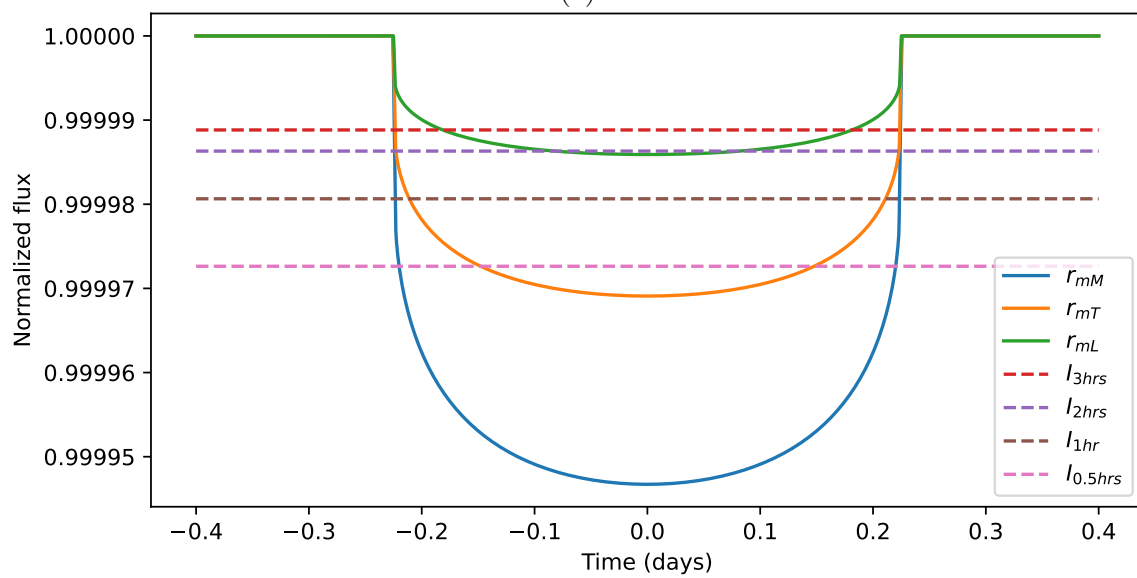


(b)

Figure 5.2: The expected photometric precision (dashed lines) for given integration times compared with the transit lightcurves for different sizes of the moons with the host-stars being (a) G2 type with $V_{mag} = 8.$, (b) K2 type with $V_{mag} = 9.$,... [cont.]

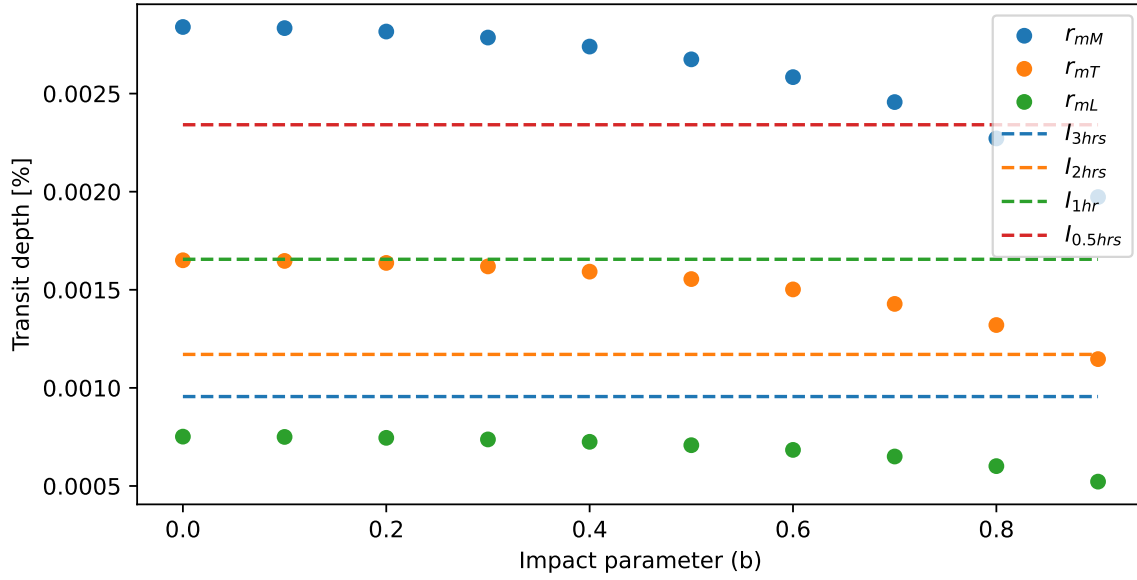


(c)

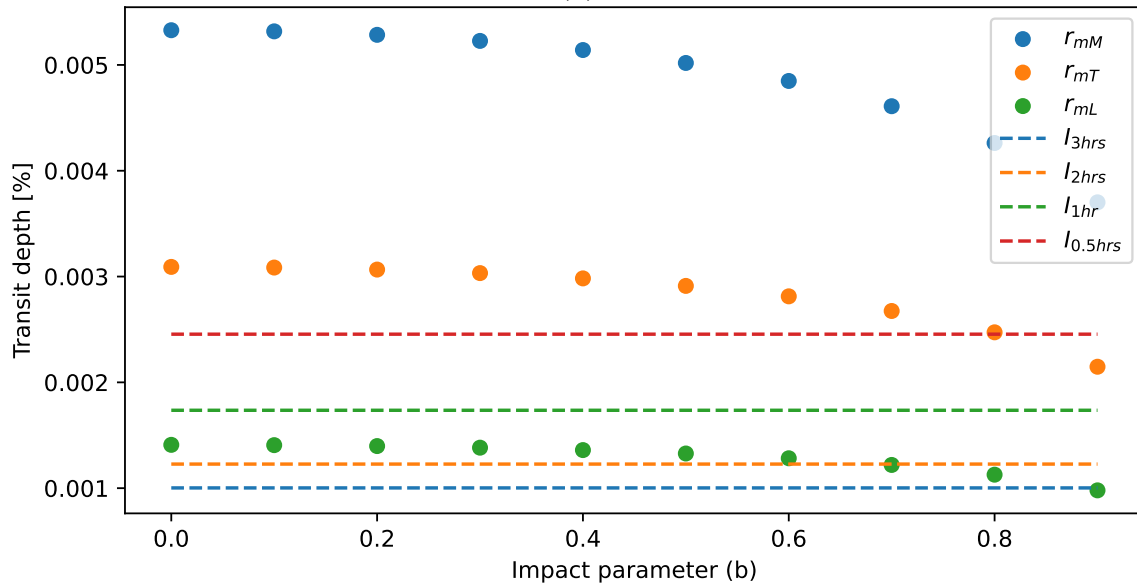


(d)

Figure 5.2: [cont.] ... (c) G2 type with $V_{mag} = 11.5$ and (d) K2 type with $V_{mag} = 12.5$.

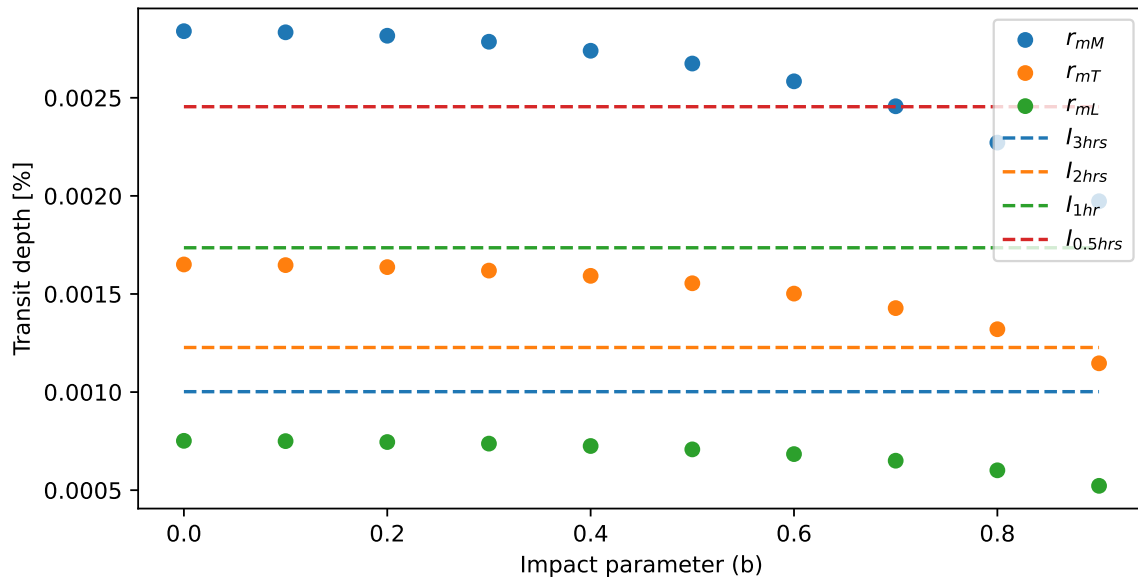


(a)

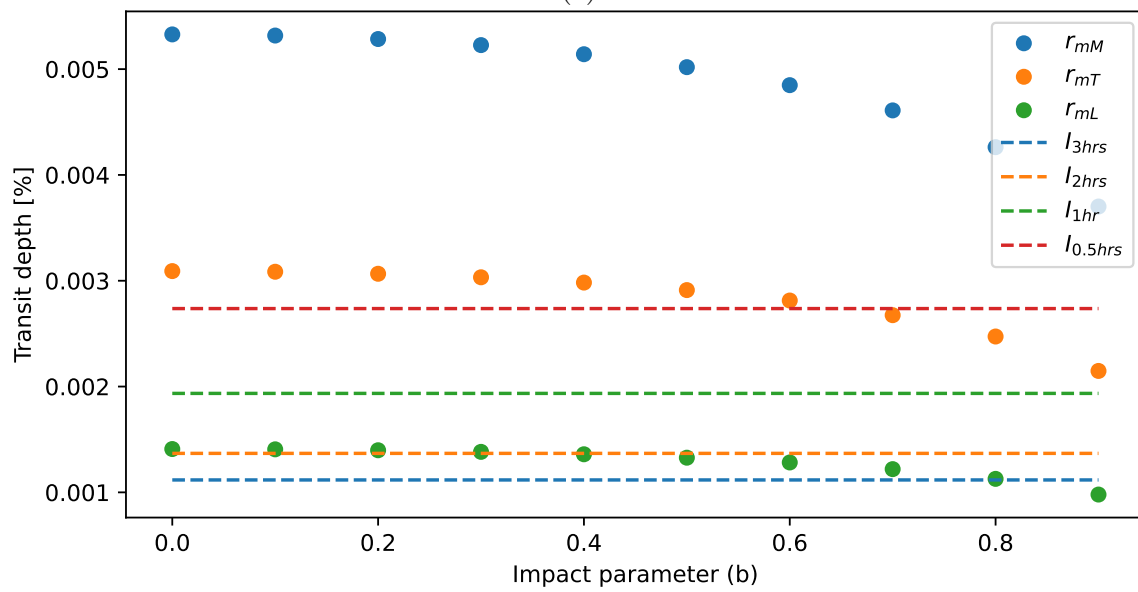


(b)

Figure 5.3: The expected photometric precision (dashed lines) for given integration times compared with the transit depths for different sizes of the moons and different values of the impact parameter with the host-stars being (a) G2 type with $V_{mag} = 8.$, (b) K2 type with $V_{mag} = 9.,...$ [cont.]



(c)



(d)

Figure 5.3: [cont.] ... (c) G2 type with $V_{mag} = 11.5$ and (d) K2 type with $V_{mag} = 12.5$.

Table 5.3: Photometric precision [in ppm] required for the detection of exomoons of different sizes around G2 and K2 type stars

Host-star type	Size of exomoon				
	Earth	Trappist-1d	Mars	Titan	Luna
<i>G2</i>	100.37	61.79	28.39	16.50	7.52
<i>K2</i>	188.48	115.7	53.28	30.91	14.09

hours.

As the transit depth is also a function of impact parameter, a change in its value will affect the detectability of an exomoon. We have compared the expected photometric precision from JWST with the expected transit depths for different values of the impact parameter, b , as plotted in Figure 5.3. It can be noticed that with an integration time of 3 hours, exomoons with the size similar to Mars and Titan can be detected for any impact parameter for both the cases of the G2-type host-stars. On the other hand, for the cases of the K2-type host-stars, with an integration time of 3 hours, it will be possible to detect exomoons with size similar to Mars and Titan for any impact parameter and an exomoon with the size similar to Luna for up to an impact parameter of 0.8.

The main advantage that JWST provides for the detection of exomoons (as well as smaller exoplanets) is the plethora of narrow, mid as well as wide band filters it provides in the near infrared region. These different filter options can be used strategically to obtain photometric signal of high SNR for potential host stars of different magnitudes while preventing saturation due to over exposure. In table 5.3, we have listed the photometric precision [in ppm] required to detect the exomoons of different sizes for both G2 and K2 type host stars for the impact parameter being 0, i.e. the exomoon transiting through the center of the host star. In tables 5.4 and 5.5, we have tabulated the estimated obtainable photometric precision [in ppm], using different shorter wavelength time-series filters of the NIRCAM instrument of JWST, for different magnitude of the G2 and K2 type host stars respectively for an integration time of 3hrs. It can be noticed from by comparing these photometric precision values that JWST has the capability for detecting exomoons smaller than the size of Titan around G2 type host stars and exomoons smaller than Luna around K2 type host stars.

Table 5.4: Photometric precision [in ppm] obtainable from different filters for G2 type host stars of different V_{mag} for an integration time of 3 hrs.

V_{mag}	Filters																					
	F187N	F212N	F140M	F182M	F210M	F070W	F090W	F115W	F150W	F200W	F187N	F212N	F140M	F182M	F210M	F070W	F090W	F115W	F150W	F200W		
8.0	9.56	10.20	-	-	-	-	-	-	-	-	-	-	-	-	-	-	-	-	-	-	-	-
8.5	12.19	13.03	-	-	-	-	-	-	-	-	-	-	-	-	-	-	-	-	-	-	-	-
9.0	15.68	16.8	-	-	-	-	-	-	-	-	-	-	-	-	-	-	-	-	-	-	-	-
9.5	20.36	21.88	-	-	-	-	-	-	-	-	-	-	-	-	-	-	-	-	-	-	-	-
10.0	26.82	28.93	-	-	-	-	-	-	-	-	-	-	-	-	-	-	-	-	-	-	-	-
10.5	35.95	38.96	-	8.93	11.6	9.59	-	-	-	-	-	-	-	-	-	-	-	-	-	-	-	-
11.0	49.34	53.78	11.71	11.37	14.86	12.22	-	-	-	-	-	-	-	-	-	-	-	-	-	-	-	8.84
11.5	69.7	76.42	15.05	14.6	19.27	15.72	11.86	10.97	10.02	11.27	-	-	-	-	-	-	-	-	-	-	-	-
12.0	100.91	111.29	19.51	18.89	25.29	20.41	15.22	14.05	12.8	14.45	-	-	-	-	-	-	-	-	-	-	-	-
12.5	149.48	165.66	25.63	24.77	33.77	26.86	19.71	18.14	16.48	18.69	-	-	-	-	-	-	-	-	-	-	-	-
13.0	225.52	250.76	34.24	33.02	46.05	35.97	25.85	23.69	21.43	24.45	-	-	-	-	-	-	-	-	-	-	-	-

5.4 Conclusion

In this work, we have studied the capability of the large next generation space based telescope, JWST, to detect rocky exomoons in the habitable zones of their host stars. We have used the analytical formalism given by Saha and Sengupta, 2022 to model the transit lightcurves for a moon hosting exoplanetary system around G2 and K2 type host stars. We have considered different sizes for the exomoon, i.e. similar to the size of the mars, the titan and the luna, around a jupiter sized planet orbiting at a distance from the host star equivalent to the earth's distance from the sun. In order to estimate the SNR of the photometric observations from JWST, we have used the JWST Exposure time calculator based on Pandeia. As the time of observable transit of the exomoon alone depends upon several factors associated with the properties of the star-planet-moon systems, we have considered an integration time of 0.5 hrs, 1 hr, 2 hrs, and 3 hrs while calculating the SNR of the photometric observations.

Studying the various scenarios, we have confirmed that exomoons as small as the titan can be detectable around a G2 type host star, and that as small as the luna can be detectable around a K2 type host star. We have also shown how a change in the impact parameter of the exomoon transit can affect its detectability. JWST has a major advantage as the presence of various narrow-band, mid-band and wide-band filters for photometric observations, which can be used strategically to study the potential host stars of different magnitudes keeping the SNR high. We have estimated the expected photometric precision from using these different filters for the host stars of different magnitudes for an integration time of 3 hrs, and compared them with the required precision to detect exomoons of different sizes.

This study evaluates the capability of JWST in detecting smaller potentially habitable exomoons through the transit photometry method. These results can be used to strategize the observations for such detection, which can result in the discovery of the first ever exomoon. The results from this work can also be extended to be applicable to other existing and upcoming space bound instruments, and for designing the next generation detectors for transit photometric studies.

Chapter 6

Summary

The works presented in this thesis consists of both observational and theoretical aspects of the transit photometric studies of exoplanets and exomoons. In this chapter, we have summarized the key results and conclusions of our studies.

In our first project, we have conducted multiband follow-up observations of a few known transiting exoplanets using two of our own ground based facilities, i.e. the 2m Himalayan Chandra Telescope (HCT) at the Indian Astronomical Observatory, Hanle and the 1.3m J. C. Bhattacharya Telescope (JCBT) at the Vainu Bappu Observatory, Kavalur. The large comparative apertures of these telescopes have resulted in photometric observations with high signal-to-noise (SNR) ratio. Also, the multiband observations have enabled us to study the wavelength dependent physical properties of our target exoplanets with a better accuracy. In order to reduce the effect of various noise components in the transit lightcurves, we have developed a state-of-the-art critical noise reduction and treatment algorithm. This algorithm uses sophisticated techniques, such as wavelet denoising to reduce the noise components that are uncorrelated in time and Gaussian process (GP) regression to reduce the noise components that are correlated in time from the lightcurves. In addition to this, our well optimized data reduction and modeling algorithm has resulted in a much better accuracy and precision in the estimation of the physical properties for our target exoplanets compared to the previous studies.

In our second project, we have extended the critical noise treatment that we have developed in our first project to the photometric transit observations from the space based telescopes. Since the space based facilities provide many advantages over their ground based counter-parts, and some of the most sophisticated existing and upcoming instruments for the study of transiting exoplanets are space based, critical analysis of the data obtained from these telescopes using more sophisticated techniques is a need of the era. In particular, the noise due to various instrumental effects and the variability and pulsations of the exoplanet hosting stars need to be reduced from the photometric signals to make them more effective in characterize the exoplanet properties. We have reiterated our critical noise treatment algorithm,

which uses both wavelet denoising and GP regression techniques, to make them applicable to the space based observations. We have demonstrated the effectiveness of our algorithm by applying it to the transit photometric observations for a few exoplanets from the Transiting Exoplanet Survey Satellite (TESS). The high SNR photometric observations from TESS combined with our critical noise treatment algorithm have resulted in significant improvement in the accuracy and precision of the estimated physical properties of the target exoplanets compared to the previously known values. The algorithm developed in this work can also be applicable to the high precision transmission spectroscopic studies using the next generation telescopes.

In our third project, we have formulated a comprehensive analytical formalism to model the lightcurves of a transiting exoplanetary system hosting exomoons. The advent of the new next generation large telescopes can provide an unique opportunity for the detection of first confirmed exomoon using the transit method of exoplanet detection. In such case, it is utmost necessary to have a comprehensive analytical formulation for the analysis of the observed lightcurves both to confirm the presence of an exomoon and to characterize their physical properties. The analytical formalism that we have presented in this work takes into account the relative size of both the planet and moon compared to their host star, their orbital properties and limb-darkening effect of the host star. As the orbit of the moon around the planet may not be co-aligned with the orbit of the planet around the star, we have used three angular parameters to independently define their alignments. We have also considered a circular orbit for the moon, which is indeed the case with the tidally locked natural satellites, and made our formalism much simpler in application by taking the advantage of the underlying symmetry. We have also demonstrated the capabilities of our formalism by modeling the lightcurves for various scenarios of a star-planet-moon system.

In our fourth project, we have studied the capability of the next generation large spec based telescope, JWST, to detect small sub-Earth sized potentially habitable exomoon around G- and K-type stars. We have considered exomoons of different sizes, i.e. similar to the size of the mars, the titan and the luna, around a jupiter sized planet orbiting at a distance from the host star equivalent to the earth's distance from the sun. We have modeled the transit lightcurves for these systems using the analytical formulation derived in our previous project, and estimated the SNR of the photometric observations from JWST using the JWST Exposure time calculator based on Pandeia. By comparing the minimum photometric precision required to detect the exomoons of different sizes to the expected obtainable photometric

precision using the NIRCAM instrument of JWST and using different near-infrared filters, we have concluded that exomoons as small as the titan would be detectable around a G2 type star and that as small as the luna would be detectable around a K2 type star.

Bibliography

- Agol, E., & Fabrycky, D. C. (2018). Transit-Timing and Duration Variations for the Discovery and Characterization of Exoplanets. In H. J. Deeg & J. A. Belmonte (Eds.), *Handbook of exoplanets* (p. 7). https://doi.org/10.1007/978-3-319-55333-7_7
- Agol, E., Jansen, T., Lacy, B., Robinson, T. D., & Meadows, V. (2015). The Center of Light: Spectroastrometric Detection of Exomoons. *ApJ*, *812*(1), Article 5, 5. <https://doi.org/10.1088/0004-637X/812/1/5>
- Bakos, G. Á., Hartman, J. D., Bhatti, W., Bieryla, A., de Val-Borro, M., Latham, D. W., Buchhave, L. A., Csubry, Z., Penev, K., Kovács, G., Béky, B., Falco, E., Kovács, T., Howard, A. W., Johnson, J. A., Isaacson, H., Marcy, G. W., Torres, G., Noyes, R. W., ... Sári, P. (2015). HAT-P-54b: A Hot Jupiter Transiting a 0.6 M_{\odot} Star in Field 0 of the K2 Mission. *AJ*, *149*(4), Article 149, 149. <https://doi.org/10.1088/0004-6256/149/4/149>
- Barros, S. C. C., Demangeon, O., Diaz, R. F., Cabrera, J., Santos, N. C., Faria, J. P., & Pereira, F. (2020). Improving transit characterisation with Gaussian process modelling of stellar variability. *A&A*, *634*, Article A75, A75. <https://doi.org/10.1051/0004-6361/201936086>
- Benedict, G. F., McArthur, B. E., Forveille, T., Delfosse, X., Nelan, E., Butler, R. P., Spiesman, W., Marcy, G., Goldman, B., Perrier, C., Jefferys, W. H., & Mayor, M. (2002). A Mass for the Extrasolar Planet Gliese 876b Determined from Hubble Space Telescope Fine Guidance Sensor 3 Astrometry and High-Precision Radial Velocities. *ApJ*, *581*(2), L115–L118. <https://doi.org/10.1086/346073>
- Bennett, D. P. (2008). Detection of Extrasolar Planets by Gravitational Microlensing. In J. W. Mason (Ed.), *Exoplanets* (p. 47). https://doi.org/10.1007/978-3-540-74008-7_3
- Bieryla, A., Collins, K., Beatty, T. G., Eastman, J., Siverd, R. J., Pepper, J., Gaudi, B. S., Stassun, K. G., Cañas, C., Latham, D. W., Buchhave, L. A., Sanchis-Ojeda, R., Winn, J. N., Jensen, E. L. N., Kielkopf, J. F., McLeod, K. K., Gregorio, J., Colón, K. D., Street, R., ... Trueblood, P. (2015). KELT-7b:

- A Hot Jupiter Transiting a Bright $V = 8.54$ Rapidly Rotating F-star. *AJ*, 150(1), Article 12, 12. <https://doi.org/10.1088/0004-6256/150/1/12>
- Bryson, S. T., Tenenbaum, P., Jenkins, J. M., Chandrasekaran, H., Klaus, T., Caldwell, D. A., Gilliland, R. L., Haas, M. R., Dotson, J. L., Koch, D. G., & Borucki, W. J. (2010). The Kepler Pixel Response Function. *ApJ*, 713(2), L97–L102. <https://doi.org/10.1088/2041-8205/713/2/L97>
- Cabrera, J., & Schneider, J. (2007). Detecting companions to extrasolar planets using mutual events. *A&A*, 464(3), 1133–1138. <https://doi.org/10.1051/0004-6361:20066111>
- Chakrabarty, A., & Sengupta, S. (2019). Precise Photometric Transit Follow-up Observations of Five Close-in Exoplanets: Update on Their Physical Properties. *AJ*, 158(1), Article 39, 39. <https://doi.org/10.3847/1538-3881/ab24dd>
- Chakrabarty, A., & Sengupta, S. (2020). Effects of Thermal Emission on the Transmission Spectra of Hot Jupiters. *ApJ*, 898(1), Article 89, 89. <https://doi.org/10.3847/1538-4357/ab9a33>
- Charbonneau, D., Brown, T. M., Latham, D. W., & Mayor, M. (2000). Detection of Planetary Transits Across a Sun-like Star. *ApJ*, 529(1), L45–L48. <https://doi.org/10.1086/312457>
- Christiansen, J. L., Ballard, S., Charbonneau, D., Deming, D., Holman, M. J., Madhusudhan, N., Seager, S., Wellnitz, D. D., Barry, R. K., Livengood, T. A., Hewagama, T., Hampton, D. L., Lisse, C. M., & A’Hearn, M. F. (2011). System Parameters, Transit Times, and Secondary Eclipse Constraints of the Exoplanet Systems HAT-P-4, TrES-2, TrES-3, and WASP-3 from the NASA EPOXI Mission of Opportunity. *ApJ*, 726(2), Article 94, 94. <https://doi.org/10.1088/0004-637X/726/2/94>
- Claret, A. (2000). A new non-linear limb-darkening law for lte stellar atmosphere models. calculations for $-5.0 \leq \log [m/h] \leq +1$, $2000 \text{ k} \leq \text{teff} \leq 50000 \text{ k}$ at several surface gravities. *A&A*, 363, 1081–1190.
- Claret, A., & Gimenez, A. (1990). Limb-darkening coefficients of late-type stars. *A&A*, 230, 412–418.
- Cubillos, P., Harrington, J., Loredó, T. J., Lust, N. B., Blečić, J., & Stemm, M. (2017). On Correlated-noise Analyses Applied to Exoplanet Light Curves. *AJ*, 153, Article 3, 3. <https://doi.org/10.3847/1538-3881/153/1/3>
- Cumming, A. (2004). Detectability of extrasolar planets in radial velocity surveys. *MNRAS*, 354(4), 1165–1176. <https://doi.org/10.1111/j.1365-2966.2004.08275>

- Damasso, M., Biazzo, K., Bonomo, A. S., Desidera, S., Lanza, A. F., Nascimbeni, V., Esposito, M., Scandariato, G., Sozzetti, A., Cosentino, R., Gratton, R., Malavolta, L., Rainer, M., Gandolfi, D., Poretti, E., Zanmar Sanchez, R., Ribas, I., Santos, N., Affer, L., . . . Southworth, J. (2015). The GAPS programme with HARPS-N at TNG. V. A comprehensive analysis of the XO-2 stellar and planetary systems. *A&A*, *575*, Article A111, A111. <https://doi.org/10.1051/0004-6361/201425332>
- Deeg, H. J., & Alonso, R. (2018). Transit Photometry as an Exoplanet Discovery Method. In H. J. Deeg & J. A. Belmonte (Eds.), *Handbook of exoplanets* (p. 117). https://doi.org/10.1007/978-3-319-55333-7_117
- del Ser, D., Fors, O., & Núñez, J. (2018). TFAW: Wavelet-based signal reconstruction to reduce photometric noise in time-domain surveys. *A&A*, *619*, Article A86, A86. <https://doi.org/10.1051/0004-6361/201730671>
- Demangeon, O. D. S., Faedi, F., Hébrard, G., Brown, D. J. A., Barros, S. C. C., Doyle, A. P., Maxted, P. F. L., Collier Cameron, A., Hay, K. L., Alikakos, J., Anderson, D. R., Armstrong, D. J., Boumis, P., Bonomo, A. S., Bouchy, F., Delrez, L., Gillon, M., Haswell, C. A., Hellier, C., . . . Wheatley, P. J. (2018). The discovery of WASP-151b, WASP-153b, WASP-156b: Insights on giant planet migration and the upper boundary of the Neptunian desert. *A&A*, *610*, Article A63, A63. <https://doi.org/10.1051/0004-6361/201731735>
- Dobos, V., Charnoz, S., Pál, A., Roque-Bernard, A., & Szabó, G. M. (2021). Survival of Exomoons Around Exoplanets. *PASP*, *133*(1027), Article 094401, 094401. <https://doi.org/10.1088/1538-3873/abfe04>
- Donoho, D., & Johnstone, I. (1994). *Ideal denoising in an orthonormal basis chosen from a library of bases*.
- Eastman, J., Siverd, R., & Gaudi, B. S. (2010). Achieving Better Than 1 Minute Accuracy in the Heliocentric and Barycentric Julian Dates. *PASP*, *122*(894), 935. <https://doi.org/10.1086/655938>
- Esposito, M., Covino, E., Desidera, S., Mancini, L., Nascimbeni, V., Zanmar Sanchez, R., Biazzo, K., Lanza, A. F., Leto, G., Southworth, J., Bonomo, A. S., Suárez Mascareño, A., Boccato, C., Cosentino, R., Claudi, R. U., Gratton, R., Maggio, A., Micela, G., Molinari, E., . . . Turner, O. D. (2017). The GAPS Programme with HARPS-N at TNG. XIII. The orbital obliquity of three close-in massive planets hosted by dwarf K-type stars: WASP-43, HAT-P-20 and Qatar-2. *A&A*, *601*, Article A53, A53. <https://doi.org/10.1051/0004-6361/201629720>

- Fewell, M. P. (2006). *Area of common overlap of three circles* (tech. rep.). DEFENCE SCIENCE and TECHNOLOGY ORGANISATION EDINBURGH (AUSTRALIA) MARITIME ...
- Föhning, D., Wilson, R. W., Osborn, J., & Dhillon, V. S. (2019). Atmospheric scintillation noise in ground-based exoplanet photometry. *MNRAS*, *489*(4), 5098–5108. <https://doi.org/10.1093/mnras/stz2444>
- Fox, C., & Wiegert, P. (2021). Exomoon candidates from transit timing variations: Eight kepler systems with ttvs explainable by photometrically unseen exomoons. *MNRAS*, *501*(2), 2378–2393.
- Gaudi, B. S. (2010). Microlensing by Exoplanets. In S. Seager (Ed.), *Exoplanets* (pp. 79–110).
- Gilliland, R. L., Chaplin, W. J., Dunham, E. W., Argabright, V. S., Borucki, W. J., Basri, G., Bryson, S. T., Buzasi, D. L., Caldwell, D. A., Elsworth, Y. P., Jenkins, J. M., Koch, D. G., Kolodziejczak, J., Miglio, A., van Cleve, J., Walkowicz, L. M., & Welsh, W. F. (2011). Kepler Mission Stellar and Instrument Noise Properties. *ApJS*, *197*(1), Article 6, 6. <https://doi.org/10.1088/0067-0049/197/1/6>
- Gillon, M., Triaud, A. H. M. J., Demory, B.-O., Jehin, E., Agol, E., Deck, K. M., Lederer, S. M., de Wit, J., Burdanov, A., Ingalls, J. G., Bolmont, E., Lecante, J., Raymond, S. N., Selsis, F., Turbet, M., Barkaoui, K., Burgasser, A., Burleigh, M. R., Carey, S. J., ... Queloz, D. (2017). Seven temperate terrestrial planets around the nearby ultracool dwarf star TRAPPIST-1. *Nature*, *542*(7642), 456–460. <https://doi.org/10.1038/nature21360>
- Han, C., & Han, W. (2002). On the Feasibility of Detecting Satellites of Extrasolar Planets via Microlensing. *ApJ*, *580*(1), 490–493. <https://doi.org/10.1086/343082>
- Hastings, W. (1970). Monte Carlo Sampling Methods using Markov Chains and their Applications. *Biometrika*, *57*(1), 97–109. <https://doi.org/10.1093/biomet/57.1.97>
- Haswell, C. A. (2010). *Transiting Exoplanets*.
- Hatzes, A. P. (2016). The Radial Velocity Method for the Detection of Exoplanets. In V. Bozza, L. Mancini, & A. Sozzetti (Eds.), *Methods of detecting exoplanets: 1st advanced school on exoplanetary science* (p. 3, Vol. 428). https://doi.org/10.1007/978-3-319-27458-4_1

- Heller, R. (2014). Detecting Extrasolar Moons Akin to Solar System Satellites with an Orbital Sampling Effect. *ApJ*, 787(1), Article 14, 14. <https://doi.org/10.1088/0004-637X/787/1/14>
- Hellier, C., Anderson, D. R., Collier Cameron, A., Gillon, M., Jehin, E., Lendl, M., Maxted, P. F. L., Pepe, F., Pollacco, D., Queloz, D., Ségransan, D., Smalley, B., Smith, A. M. S., Southworth, J., Triaud, A. H. M. J., Udry, S., & West, R. G. (2011). WASP-43b: the closest-orbiting hot Jupiter. *A&A*, 535, Article L7, L7. <https://doi.org/10.1051/0004-6361/201117081>
- Hellier, C., Anderson, D. R., Collier Cameron, A., Delrez, L., Gillon, M., Jehin, E., Lendl, M., Maxted, P. F. L., Pepe, F., Pollacco, D., Queloz, D., Ségransan, D., Smalley, B., Smith, A. M. S., Southworth, J., Triaud, A. H. M. J., Udry, S., & West, R. G. (2014). Transiting hot Jupiters from WASP-South, Euler and TRAPPIST: WASP-95b to WASP-101b. *MNRAS*, 440(3), 1982–1992. <https://doi.org/10.1093/mnras/stu410>
- Hellier, C., Anderson, D. R., Collier Cameron, A., Gillon, M., Lendl, M., Maxted, P. F. L., Queloz, D., Smalley, B., Triaud, A. H. M. J., West, R. G., Brown, D. J. A., Enoch, B., Lister, T. A., Pepe, F., Pollacco, D., Ségransan, D., & Udry, S. (2010). WASP-29b: A Saturn-sized Transiting Exoplanet. *ApJ*, 723(1), L60–L63. <https://doi.org/10.1088/2041-8205/723/1/L60>
- Henry, G. W., Marcy, G. W., Butler, R. P., & Vogt, S. S. (2000). A Transiting “51 Peg-like” Planet. *ApJ*, 529(1), L41–L44. <https://doi.org/10.1086/312458>
- Hinkley, S., Vigan, A., Kasper, M., Quanz, S. P., & Lacour, S. (2021). Direct Imaging and Spectroscopy. In N. Madhusudhan (Ed.), *Exofrontiers; big questions in exoplanetary science* (pp. 5–1). <https://doi.org/10.1088/2514-3433/abfa8fch5>
- Jenkins, J. M. (2017). Kepler Data Processing Handbook: Overview of the Science Operations Center.
- Johnson, J. A., Winn, J. N., Bakos, G. Á., Hartman, J. D., Morton, T. D., Torres, G., Kovács, G., Latham, D. W., Noyes, R. W., Sato, B., Esquerdo, G. A., Fischer, D. A., Marcy, G. W., Howard, A. W., Buchhave, L. A., Fűrész, G., Quinn, S. N., Béky, B., Sasselov, D. D., . . . Sári, P. (2011). HAT-P-30b: A Transiting Hot Jupiter on a Highly Oblique Orbit. *ApJ*, 735(1), Article 24, 24. <https://doi.org/10.1088/0004-637X/735/1/24>
- Johnson, M. C., Cochran, W. D., Collier Cameron, A., & Bayliss, D. (2015). Measurement of the Nodal Precession of WASP-33 b via Doppler Tomography. *ApJ*, 810(2), Article L23, L23. <https://doi.org/10.1088/2041-8205/810/2/L23>

- Johnson, R. E., & Huggins, P. J. (2006). Toroidal Atmospheres around Extrasolar Planets. *PASP*, *118*(846), 1136–1143. <https://doi.org/10.1086/506183>
- Kipping, D. (2020). An Independent Analysis of the Six Recently Claimed Exomoon Candidates. *ApJ*, *900*(2), Article L44, L44. <https://doi.org/10.3847/2041-8213/abafa9>
- Kipping, D. (2021). The exomoon corridor: Half of all exomoons exhibit TTV frequencies within a narrow window due to aliasing. *MNRAS*, *500*(2), 1851–1857. <https://doi.org/10.1093/mnras/staa3398>
- Kipping, D. M. (2009). Transit timing effects due to an exomoon. *MNRAS*, *392*(1), 181–189. <https://doi.org/10.1111/j.1365-2966.2008.13999.x>
- Kipping, D. M. (2011). LUNA: an algorithm for generating dynamic planet-moon transits. *MNRAS*, *416*(1), 689–709. <https://doi.org/10.1111/j.1365-2966.2011.19086.x>
- Lee, G. R., Gommers, R., Waselewski, F., Wohlfahrt, K., & O’Leary, A. (2019). Pywavelets: A python package for wavelet analysis. *Journal of Open Source Software*, *4*(36), 1237. <https://doi.org/10.21105/joss.01237>
- Lewis, K. M., Sackett, P. D., & Mardling, R. A. (2008). Possibility of Detecting Moons of Pulsar Planets through Time-of-Arrival Analysis. *ApJ*, *685*(2), L153. <https://doi.org/10.1086/592743>
- Lightkurve Collaboration, Cardoso, J. V. d. M., Hedges, C., Gully-Santiago, M., Saunders, N., Cody, A. M., Barclay, T., Hall, O., Sagar, S., Turtelboom, E., Zhang, J., Tzanidakis, A., Mighell, K., Coughlin, J., Bell, K., Berta-Thompson, Z., Williams, P., Dotson, J., & Barentsen, G. (2018). Lightkurve: Kepler and TESS time series analysis in Python.
- Livingston, J. H., Crossfield, I. J. M., Werner, M. W., Gorjian, V., Petigura, E. A., Ciardi, D. R., Dressing, C. D., Fulton, B. J., Hirano, T., Schlieder, J. E., Sinukoff, E., Kosiarek, M., Akeson, R., Beichman, C. A., Benneke, B., Christiansen, J. L., Hansen, B. M. S., Howard, A. W., Isaacson, H., . . . Tamura, M. (2019). Spitzer Transit Follow-up of Planet Candidates from the K2 Mission. *AJ*, *157*(3), Article 102, 102. <https://doi.org/10.3847/1538-3881/aaff69>
- Lovis, C., & Fischer, D. (2010). Radial Velocity Techniques for Exoplanets. In S. Seager (Ed.), *Exoplanets* (pp. 27–53).
- Luo, G., & Zhang, D. (2012). *Wavelet denoising, advances in wavelet theory and their applications in engineering, physics and technology, dr. dimitru baleanu (ed.)* InTech.

- Maciejewski, G., Fernández, M., Aceituno, F., Martín-Ruiz, S., Ohlert, J., Dimitrov, D., Szyszka, K., von Essen, C., Mugrauer, M., Bischoff, R., Michel, K. .-. , Mallonn, M., Stangret, M., & Moździerski, D. (2018). Planet-Star Interactions with Precise Transit Timing. I. The Refined Orbital Decay Rate for WASP-12 b and Initial Constraints for HAT-P-23 b, KELT-1 b, KELT-16 b, WASP-33 b and WASP-103 b. *Acta Astron.*, *68*(4), 371–401. <https://doi.org/10.32023/0001-5237/68.4.4>
- Malbet, F., & Sozzetti, A. (2018). Astrometry as an Exoplanet Discovery Method. In H. J. Deeg & J. A. Belmonte (Eds.), *Handbook of exoplanets* (p. 196). https://doi.org/10.1007/978-3-319-55333-7_196
- Mandel, K., & Agol, E. (2002). Analytic Light Curves for Planetary Transit Searches. *ApJ*, *580*(2), L171–L175. <https://doi.org/10.1086/345520>
- Martin, D. V., Fabrycky, D. C., & Montet, B. T. (2019). Transits of Inclined Exomoons—Hide and Seek and an Application to Kepler-1625. *ApJ*, *875*(2), Article L25, L25. <https://doi.org/10.3847/2041-8213/ab0aea>
- Mayor, M., & Queloz, D. (1995). A Jupiter-mass companion to a solar-type star. *Nature*, *378*(6555), 355–359. <https://doi.org/10.1038/378355a0>
- Namouni, F. (2010). The Fate of Moons of Close-in Giant Exoplanets. *ApJ*, *719*(2), L145–L147. <https://doi.org/10.1088/2041-8205/719/2/L145>
- Nesvorný, D., Kipping, D. M., Buchhave, L. A., Bakos, G. Á., Hartman, J., & Schmitt, A. R. (2012). The detection and characterization of a nontransiting planet by transit timing variations. *Science*, *336*(6085), 1133–1136.
- Noyola, J. P., Satyal, S., & Musielak, Z. E. (2014). Detection of Exomoons through Observation of Radio Emissions. *ApJ*, *791*(1), Article 25, 25. <https://doi.org/10.1088/0004-637X/791/1/25>
- Noyola, J. P., Satyal, S., & Musielak, Z. E. (2016). On the Radio Detection of Multiple-exomoon Systems due to Plasma Torus Sharing. *ApJ*, *821*(2), Article 97, 97. <https://doi.org/10.3847/0004-637X/821/2/97>
- Osborn, J., Föhning, D., Dhillon, V. S., & Wilson, R. W. (2015). Atmospheric scintillation in astronomical photometry. *MNRAS*, *452*(2), 1707–1716. <https://doi.org/10.1093/mnras/stv1400>
- Oza, A. V., Johnson, R. E., Lellouch, E., Schmidt, C., Schneider, N., Huang, C., Gamborino, D., Gebek, A., Wyttenbach, A., Demory, B.-O., Mordasini, C., Saxena, P., Dubois, D., Moullet, A., & Thomas, N. (2019). Sodium and Potassium Signatures of Volcanic Satellites Orbiting Close-in Gas Giant

- Exoplanets. *ApJ*, 885(2), Article 168, 168. <https://doi.org/10.3847/1538-4357/ab40cc>
- Patra, K. C., Winn, J. N., Holman, M. J., Yu, L., Deming, D., & Dai, F. (2017). The Apparently Decaying Orbit of WASP-12b. *AJ*, 154(1), Article 4, 4. <https://doi.org/10.3847/1538-3881/aa6d75>
- Peale, S. J. (1999). Origin and Evolution of the Natural Satellites. *ARA&A*, 37, 533–602. <https://doi.org/10.1146/annurev.astro.37.1.533>
- Pereira, F., Campante, T. L., Cunha, M. S., Faria, J. P., Santos, N. C., Barros, S. C. C., Demangeon, O., Kuszlewicz, J. S., & Corsaro, E. (2019). Gaussian process modelling of granulation and oscillations in red giant stars. *MNRAS*, 489(4), 5764–5774. <https://doi.org/10.1093/mnras/stz2405>
- Perryman, M. A. C. (2000). Extra-solar planets. *Reports on Progress in Physics*, 63(8), 1209–1272. <https://doi.org/10.1088/0034-4885/63/8/202>
- Pontoppidan, K. M., Pickering, T. E., Laidler, V. G., Gilbert, K., Sontag, C. D., Slocum, C., Sienkiewicz, M. J., Hanley, C., Earl, N. M., Pueyo, L., Ravindranath, S., Karakla, D. M., Robberto, M., Noriega-Crespo, A., & Barker, E. A. (2016). Pandeia: a multi-mission exposure time calculator for JWST and WFIRST. In A. B. Peck, R. L. Seaman, & C. R. Benn (Eds.), *Observatory operations: Strategies, processes, and systems vi* (p. 991016, Vol. 9910). <https://doi.org/10.1117/12.2231768>
- Pueyo, L. (2018). Direct Imaging as a Detection Technique for Exoplanets. In H. J. Deeg & J. A. Belmonte (Eds.), *Handbook of exoplanets* (p. 10). https://doi.org/10.1007/978-3-319-55333-7_10
- Quan Pan, Lei Zhang, Guanzhong Dai, & Hongai Zhang. (1999). Two denoising methods by wavelet transform. *IEEE Transactions on Signal Processing*, 47(12), 3401–3406. <https://doi.org/10.1109/78.806084>
- Quirrenbach, A. (2010). Astrometric Detection and Characterization of Exoplanets. In S. Seager (Ed.), *Exoplanets* (pp. 157–174).
- Rasmussen, C. E., & Williams, C. K. I. (2006). *Gaussian Processes for Machine Learning*. The MIT Press.
- Ricker, G. R., Winn, J. N., Vanderspek, R., Latham, D. W., Bakos, G. Á., Bean, J. L., Berta-Thompson, Z. K., Brown, T. M., Buchhave, L., Butler, N. R., Butler, R. P., Chaplin, W. J., Charbonneau, D., Christensen-Dalsgaard, J., Clampin, M., Deming, D., Doty, J., De Lee, N., Dressing, C., . . . Villaseñor, J. (2015). Transiting Exoplanet Survey Satellite (TESS). *Journal of Astronomical*

- Telescopes, Instruments, and Systems*, 1, Article 014003, 014003. <https://doi.org/10.1117/1.JATIS.1.1.014003>
- Saha, S. (2023). Precise Transit Photometry Using TESS: Updated Physical Properties for 28 Exoplanets Around Bright Stars. *arXiv e-prints*, Article arXiv:2306.02951, arXiv:2306.02951. <https://doi.org/10.48550/arXiv.2306.02951>
- Saha, S., Chakrabarty, A., & Sengupta, S. (2021). Multiband Transit Follow-up Observations of Five Hot Jupiters with Critical Noise Treatments: Improved Physical Properties. *AJ*, 162(1), Article 18, 18. <https://doi.org/10.3847/1538-3881/ac01dd>
- Saha, S., & Sengupta, S. (2021). Critical Analysis of Tess Transit Photometric Data: Improved Physical Properties for Five Exoplanets. *AJ*, 162(5), Article 221, 221. <https://doi.org/10.3847/1538-3881/ac294d>
- Saha, S., & Sengupta, S. (2022). Transit Light Curves for Exomoons: Analytical Formalism. *ApJ*, 936(1), Article 2, 2. <https://doi.org/10.3847/1538-4357/ac85a9>
- Sartoretti, P., & Schneider, J. (1999). On the detection of satellites of extrasolar planets with the method of transits. *A&AS*, 134, 553–560. <https://doi.org/10.1051/aas:1999148>
- Schwarz, G. (1978). Estimating the Dimension of a Model. *Annals of Statistics*, 6(2), 461–464.
- Sengupta, S., Chakrabarty, A., & Tinetti, G. (2020). Optical Transmission Spectra of Hot Jupiters: Effects of Scattering. *ApJ*, 889(2), Article 181, 181. <https://doi.org/10.3847/1538-4357/ab6592>
- Sengupta, S., & Marley, M. S. (2016). Detecting Exomoons around Self-luminous Giant Exoplanets through Polarization. *ApJ*, 824(2), Article 76, 76. <https://doi.org/10.3847/0004-637X/824/2/76>
- Sing, D. K. (2010). Stellar limb-darkening coefficients for CoRoT and Kepler. *A&A*, 510, Article A21, A21. <https://doi.org/10.1051/0004-6361/200913675>
- Smith, J. C., Stumpe, M. C., Cleve, J. E. V., Jenkins, J. M., Barclay, T. S., Fanelli, M. N., Girouard, F. R., Kolodziejczak, J. J., McCauliff, S. D., Morris, R. L., & Twicken, J. D. (2012). Kepler presearch data conditioning ii - a bayesian approach to systematic error correction. *PASP*, 124(919), 1000–1014. <http://www.jstor.org/stable/10.1086/667697>
- Southworth, J., Wheatley, P. J., & Sams, G. (2007). A method for the direct determination of the surface gravities of transiting extrasolar planets. *MNRAS*, 379, L11–L15. <https://doi.org/10.1111/j.1745-3933.2007.00324.x>

- Sozzetti, A., Torres, G., Charbonneau, D., Winn, J. N., Korzennik, S. G., Holman, M. J., Latham, D. W., Laird, J. B., Fernandez, J., O'Donovan, F. T., Mandushev, G., Dunham, E., Everett, M. E., Esquerdo, G. A., Rabus, M., Belmonte, J. A., Deeg, H. J., Brown, T. N., Hidas, M. G., & Baliber, N. (2009). A New Spectroscopic and Photometric Analysis of the Transiting Planet Systems TrES-3 and TrES-4. *ApJ*, *691*(2), 1145–1158. <https://doi.org/10.1088/0004-637X/691/2/1145>
- Spalding, C., Batygin, K., & Adams, F. C. (2016). Resonant Removal of Exomoons during Planetary Migration. *ApJ*, *817*(1), Article 18, 18. <https://doi.org/10.3847/0004-637X/817/1/18>
- Stumpe, M. C., Smith, J. C., Catanzarite, J. H., Van Cleve, J. E., Jenkins, J. M., Twicken, J. D., & Girouard, F. R. (2014). Multiscale Systematic Error Correction via Wavelet-Based Bandsplitting in Kepler Data. *PASP*, *126*(935), 100. <https://doi.org/10.1086/674989>
- Stumpe, M. C., Smith, J. C., Van Cleve, J. E., Twicken, J. D., Barclay, T. S., Fanelli, M. N., Girouard, F. R., Jenkins, J. M., Kolodziejczak, J. J., McCauliff, S. D., & Morris, R. L. (2012). Kepler Presearch Data Conditioning I—Architecture and Algorithms for Error Correction in Kepler Light Curves. *PASP*, *124*(919), 985. <https://doi.org/10.1086/667698>
- Szabó, G. M., Szatmáry, K., Divéki, Z., & Simon, A. (2006). Possibility of a photometric detection of “exomoons”. *A&A*, *450*(1), 395–398. <https://doi.org/10.1051/0004-6361:20054555>
- Teachey, A., Kipping, D. M., & Schmitt, A. R. (2018). HEK. VI. On the Dearth of Galilean Analogs in Kepler, and the Exomoon Candidate Kepler-1625b I. *AJ*, *155*(1), Article 36, 36. <https://doi.org/10.3847/1538-3881/aa93f2>
- Teachey, A., & Kipping, D. M. (2018). Evidence for a large exomoon orbiting Kepler-1625b. *Science Advances*, *4*(10), Article eaav1784, eaav1784. <https://doi.org/10.1126/sciadv.aav1784>
- Torres, G., Bakos, G. Á., Hartman, J., Kovács, G., Noyes, R. W., Latham, D. W., Fischer, D. A., Johnson, J. A., Marcy, G. W., Howard, A. W., Sasselov, D. D., Kipping, D., Sipőcz, B., Stefanik, R. P., Esquerdo, G. A., Everett, M. E., Lázár, J., Papp, I., & Sári, P. (2010). HAT-P-14b: A 2.2 M_J Exoplanet Transiting a Bright F Star. *ApJ*, *715*(1), 458–467. <https://doi.org/10.1088/0004-637X/715/1/458>
- Traub, W. A., & Oppenheimer, B. R. (2010). Direct Imaging of Exoplanets. In S. Seager (Ed.), *Exoplanets* (pp. 111–156).

- Van Cleve, J. E., Howell, S. B., Smith, J. C., Clarke, B. D., Thompson, S. E., Bryson, S. T., Lund, M. N., Handberg, R., & Chaplin, W. J. (2016). That's How We Roll: The NASA K2 Mission Science Products and Their Performance Metrics. *PASP*, *128*(965), 075002. <https://doi.org/10.1088/1538-3873/128/965/075002>
- Waldmann, I. P. (2014). On Signals Faint and Sparse: The ACICA Algorithm for Blind De-trending of Exoplanetary Transits with Low Signal-to-noise. *ApJ*, *780*, Article 23, 23. <https://doi.org/10.1088/0004-637X/780/1/23>
- Williams, D. M., & Knacke, R. F. (2004). Looking for Planetary Moons in the Spectra of Distant Jupiters. *Astrobiology*, *4*(3), 400–403. <https://doi.org/10.1089/ast.2004.4.400>
- Winn, J. N. (2010). Exoplanet Transits and Occultations. In S. Seager (Ed.), *Exoplanets* (pp. 55–77).
- Wright, J. T. (2018). Radial Velocities as an Exoplanet Discovery Method. In H. J. Deeg & J. A. Belmonte (Eds.), *Handbook of exoplanets* (p. 4). https://doi.org/10.1007/978-3-319-55333-7_4
- Wright, J. T., & Gaudi, B. S. (2013). Exoplanet Detection Methods. In T. D. Oswalt, L. M. French, & P. Kalas (Eds.), *Planets, stars and stellar systems. volume 3: Solar and stellar planetary systems* (p. 489). https://doi.org/10.1007/978-94-007-5606-9_10